INTERACTION OF A STRONGLY FOCUSED LIGHT BEAM WITH SINGLE ATOMS

SYED ABDULLAH BIN SYED ABDUL RAHMAN ALJUNID

A THESIS SUBMITTED FOR THE DEGREE OF
DOCTOR OF PHILOSOPHY

Centre for Quantum Technologies
National University of Singapore
2012

Declaration

I hereby declare that this thesis is my original work and it has been written by me in its entirety. I have duly acknowledged all the sources of information which have been used in the thesis.

This thesis has also not been submitted for any degree in any university previously.

Syed Abdullah Bin Syed
Abdul Rahman Aljunid
25th May 2012

ACKNOWLEDGMENTS

Special thanks goes to Dr. Gleb Maslennikov for being there, working on the project for as long as I have, teaching me things about mechanics, electronics and stuff in general and also for guiding me back to the big picture whenever I get too distracted trying to make everything work perfectly. You help remind me how fun and interesting real physics can be, especially when everything makes sense.

Thanks definitely goes to my PhD supervisor Prof Christian Kurtsiefer who taught me everything about atomic physics, quantum optics, hardware programming and everything you should not do if you do not want your lab to burn down. Thank you for your guidance and support throughout my candidature and for encouraging me to go for conferences near and far.

Thanks to Brenda Chng for keeping track of details of the experiment in your lab book, for encouraging us to be safe in the lab all this while and for proof-reading this thesis. I'm not sure if I still have a deposit in the Bank of Brenda, but feel free to use it.

I would also like to extend special thanks to Lee Jianwei for helping me move and rebuild the experiment from building S13 to S15 and also build up the entire experiment on Raman cooling. Thanks to everyone that I had the pleasure to work with in all stages of the experiment especially, Meng Khoon, Florian, Zilong, Martin, Kadir, DHL, Victor, Andreas and anyone else that I may have left out.

Special thanks also goes out to Wang Yimin and Colin Teo from the Theory group for their enormous help in predicting and simulating the conditions for our experiments. Without Yimin's help, the nice theoretical curves for the pulsed experiment won't be there and I'd still be confused about some theory about atom excitation.

Thanks also goes out to those working on other experiments in the Quantum Optics lab for entertaining my distractions as I get bored looking at single atoms. Thanks to Hou Shun, Tien Tjuen, Siddarth, Bharat, Gurpreet, Peng Kian, Chen Ming, Wilson and too many others to include.

Heartfelt thanks also to all the technical support team, especially Eng Swee, Imran and Uncle Bob who always manage to assist me like trying to solder a 48-pin chip the size of an ant and teaching me the best way to machine a part of an assembly and all the interesting discussion about everyday stuff that I had in the workshops. Thanks to Pei Pei, Evon, Lay Hua, Mashitah and Jessie for making the admin matters incredibly easy for us. Also thanks to all whom I meet along the

way from home to the lab that never failed to exchange greetings and made entering the dark lab a bit less gloomy.

Finally thanks to my family members and friends for the company and keeping me sane whenever I require respite from the many things that can drive anyone to tears in the lab.

CONTENTS

SUMMARY

The work in experimentally measuring the interaction of a strongly focused Gaussian light beam with a quantum system is presented here. The quantum system that is probed is a single ^{87}Rb atom trapped in the focus of a far off resonant 980 nm optical dipole trap. The atom is optically pumped into a two-level cycling transition such that it has a simple theoretical description in its interaction with the 780 nm probe light. Two classes of experiment were performed, one with a weak coherent continuous wave light and another with a strong coherent pulsed light source. In the weak cw experiments, an extinction of 8.2 ± 0.2 % with a corresponding reflection of 0.161 ± 0.007 % [1], and a maximal phase shift of 0.93° [2] by a single atom were measured. For these cw experiments, a single quantity, the scattering ratio R_{sc}, is sufficient to quantify the interaction strength of a Gaussian beam focused on a single atom, stationary at the focus. This ratio is dependent only on the focusing strength u, conveniently defined in terms of the Gaussian beam waist. The scattering ratio cannot be measured directly. Instead, experimentally measurable quantities such as extinction, reflection and induced phase shift, which are shown to be directly related to the scattering ratio, are measured and its value extracted.

In the experiments with strong coherent pulses, we investigate the effect of the shape of the pulses on its interaction with the single atom. Ideally the pulses should be from a single photon in the Fock number state. However, since we do not have a single photon source at the correct frequency and bandwidth yet, and also because the interaction strength is still low, a coherent probe light that is quite intense is sent to the atom instead. It is also much simpler to temporally shape coherent pulses by an EOM. The length of the pulses were on the order of the lifetime of the atomic transition. Two different pulse shapes are chosen as discussed by Wang et al. [3], rectangular and a rising exponential. The excitation probability of the atom per pulse sent is measured for different pulse shapes, bandwidths and average photon number. It is shown that before saturation, and for a similar pulse bandwidth, the rising exponential pulse will attain a higher excitation probability compared to a rectangular pulse with the same average photon number in the pulse.

LIST OF SYMBOLS

$\hbar$	Reduced Plank constant
ε_0	Permittivity of free space
c	Speed of light in vacuum
e	Electron charge
k_B	Boltzmann constant

1

INTRODUCTION

The rise of *Quantum Information Science* in the past two and a half decades has been driven by many discoveries and advancements. This blend of *quantum mechanics*, *information theory* and *computer science* occurred when pioneers in the field began to ask fundamental questions about the physical limits of computation, such as, what is the minimal free energy dissipation that must accompany a computation step [4, 5], is there a protocol to distribute secret keys with unconditional security [6, 7], are there algorithms that optimise factoring and sorting [8, 9] and other such problems. An interesting possibility of QIS is quantum computation [10], where the quantum property of *entanglement*, not present in classical physics, is utilised. If the elementary information of a normal computer is encoded in bits of 0 or 1, then information in a quantum computer is encoded in quantum bits or *qubits*, where the qubit is in an arbitrary coherent superposition of 0 and/or 1. Quantum computers then use these qubits, entangled or otherwise, to perform quantum computation algorithms that far outperform classical computation algorithms in certain classes of problem and simulations.

There are many different systems under study for the actual implementation of quantum computers such as trapped ions [11], neutral atoms [12], spins in NMR [13], cavity QED [14], superconducting circuits [15], quantum dots [16] and several others [17, 18]. In any physical realisation however, there will always be some factors that limit their usability as a true quantum device. DiVincenzo [19] lists the "Five (plus two) requirements for the implementation of quantum computation" as

1. Scalable physical system with well characterised qubits
2. Initialisation of the state of the qubits is possible
3. Decoherence time of the qubit needs to be much longer than the gate operation time
4. A Universal set of quantum gates can be applied
5. Qubit-selective measurement capability
6. Ability to interconnect stationary and flying qubits
7. Proper transmission of flying qubits between locations,

where the last two are not actual requirements for a quantum computer but requirements for quantum communication between two quantum computers. Photons are an inherently suitable choice for flying qubits since they can propagate freely through air or fibre for a large distance before being absorbed or scattered. This is the envisioned quantum network of photons as the flying qubit of information carrier and atom-like systems at the nodes of the network as stationary qubits of information storage and/or processor [20, 21, 22, 23]. To achieve this vision and requirement number 6, it is necessary to have a high fidelity of information transfer between the flying and stationary qubits. Because of the no cloning theorem, qubits cannot be read and copied in an arbitrary basis without affecting the qubit itself. As such, we require an interaction which not only preserves but faithfully transfers all the quantum information between the stationary and flying qubits. A common method of achieving this interaction with high fidelity is to place an atom (stationary qubit) in a high-finesse optical cavity which enhances the electric field strength of the photons (flying qubits) and thus its interaction with the atom [24, 25]. An alternative method of achieving this enhanced interaction is to use an ensemble of atoms where a collective enhancement effect is observed [21].

Here we explore the interaction of light, focused by a lens, with a *single* trapped atom. This study will determine how feasible it is to have a quantum interface by simply focusing the light. This has practical relevance/interest because it has been shown that an optical lattice can be used to trap many single atoms [26] and hence offer simple upward scalability compared to high-finesse cavity systems which are technologically demanding to scale up. A whole range of different atom-like systems have and are still being investigated as the ideal element to be used as an interface [27, 28, 18]. Although not all systems are equally suitable as an interface for qubits, these studies do allow seemingly related questions such as, whether they can be used as a conditional phase gate [29, 2] or a triggered single photon source [30, 31].

The system used here is a single Rubidium87 atom trapped in a far off resonant optical dipole trap [32]. The atom is probed using on resonant light focused tightly and then recollected using an aspheric lens pair in a confocal arrangement. Two regimes of interactions are explored, one using a weak coherent laser beam and the other using strong coherent pulses. The outline of this thesis is as follows. Chapter 2 presents the theory of light-atom interaction. The simple case of a plane wave is briefly summarised in section 2.1 and its extension to a strongly focused Gaussian beam, following the work of Tey et al. [33] is presented in section 2.2. In section 2.5, the work of Wang

et al. [3] on the theory of shaped excitation pulses interacting with a single atom is presented.

In chapter 3 the experiments performed to measure the interaction of light with a single Rubidium atom as a two-level system is presented. The basic setup that is similar for all experiments performed is detailed in sections 3.1 and 3.2. Finally the conclusion and future outlook of possible experiments are discussed in chapter 4. The results of the phase shift and reflection measurements are published in [2, 1], while a manuscript is being prepared for the pulsed experiments.

2

INTERACTION OF LIGHT WITH A TWO-LEVEL ATOM

In this chapter, we will review the theoretical aspects of the interaction of light with a two-level atom. The atom will be approximated by an atomic dipole while the probe light beam will be treated initially as a classical electric field. For a strongly focused continuous wave Gaussian beam, a useful quantity to quantify the interaction strength, is the scattering ratio, R_{sc}, will be described [33]. It will be shown that experimentally observable quantities such as transmission, reflection and phase shifts, can all be determined from R_{sc}.

The next section discusses some of the effects of temperature on the observed interaction [34]. In subsection 2.5, the case of pulsed excitation will be described where the probe is no longer a continuous wave. Thus, a new Hamiltonian which captures the relevant dynamics is introduced [3]. In this pulsed regime, the interaction strength is quantified through the excitation probability, P_e which is a measure of the atomic population in the excited state.

2.1 INTERACTION IN THE WEAK COHERENT CASE

The interaction of light with a two-level system has been discussed in great detail in many textbooks [35, 36, 37]. There are many regions of interest ranging from a purely classical atom and electromagnetic field, to that of a semi-classical model, where the atom is quantised and the field remains classical, and finally a fully quantum one, where both the atom and the field are quantised. In this section, a semi-classical model of atom light interaction with spontaneous decay is used. From this model, the expression for power scattered by a two level atom will be obtained.

2.1.1 *Semi-classical model*

A semi-classical model of atom light interaction is one where quantum mechanics is used to treat the atom while the light is treated as a classical electric field. In such a treatment, the Hamiltonian of the system can be written as,

$$H = H_0 + H_I(t), \tag{1}$$

where H_0 is the Hamiltonian of the unperturbed two-level atom with energy eigenstates $\left|\phi_i\right\rangle$ and eigenvalues E_i and $H_I(t)$ is the perturbation by the oscillating electric field of the light, which has the form

$$H_I(t) = -\hat{\mathbf{d}} \cdot \mathbf{E}(t), \tag{2}$$

where $\hat{\mathbf{d}}$ is the atomic dipole operator under the dipole approximation that is purely non-diagonal in the basis $\left\{\left|\phi_1\right\rangle, \left|\phi_2\right\rangle\right\}$. For a circularly polarised electric field[1] with amplitude E_0 and frequency ω and of the form $\mathbf{E}(t) = E_0 \left[\cos(\omega t)\,\hat{\mathbf{x}} + \sin(\omega t)\,\hat{\mathbf{y}}\right]/\sqrt{2}$ and the dipole operator written as $\hat{\mathbf{d}} = -e\hat{\mathbf{r}}$, the interaction Hamiltonian can be simplified to,

$$\begin{aligned} H_I(t) &= \frac{eE_0}{\sqrt{2}}\hat{\mathbf{r}} \cdot \left(\frac{\mathrm{e}^{\mathrm{i}\omega t} + \mathrm{e}^{-\mathrm{i}\omega t}}{2}\hat{\mathbf{x}} - \mathrm{i}\frac{\mathrm{e}^{\mathrm{i}\omega t} - \mathrm{e}^{-\mathrm{i}\omega t}}{2}\hat{\mathbf{y}} \right) \\ &= \frac{eE_0}{2}\left(r_- \mathrm{e}^{\mathrm{i}\omega t} + r_+ \mathrm{e}^{-\mathrm{i}\omega t} \right), \end{aligned}$$

where $r_\pm = (x \pm \mathrm{i}y)/\sqrt{2}$. The wavefunction of the unperturbed Hamiltonian can be expressed as

$$\begin{aligned} \Psi(\mathbf{r}, t) &= c_1(t)\left|\phi_1\right\rangle \mathrm{e}^{-\mathrm{i}E_1 t/\hbar} + c_2(t)\left|\phi_2\right\rangle \mathrm{e}^{-\mathrm{i}E_2 t/\hbar} \\ \Psi_1(\mathbf{r}, t) &= c_1\left|\phi_1\right\rangle + c_2\left|\phi_2\right\rangle \mathrm{e}^{-\mathrm{i}\omega_0 t}, \end{aligned} \tag{3}$$

where c_1 and c_2 are time-dependent coefficients of the atomic population and are normalised such that $|c_1|^2 + |c_2|^2 = 1$ and $\hbar\omega_0 = E_2 - E_1$, with a change in its global phase. The wavefunction satisfies the Schrödinger equation,

$$\mathrm{i}\hbar\frac{\partial \Psi}{\partial t} = H\Psi, \tag{4}$$

which gives differential equations for the coefficients,

$$\begin{aligned} \mathrm{i}\dot{c}_1 &= \frac{c_2}{2}\left\{ \frac{\left\langle\phi_1\right| er_- E_0 \left|\phi_2\right\rangle}{\hbar} \mathrm{e}^{\mathrm{i}(\omega-\omega_0)t} + \frac{\left\langle\phi_1\right| er_+ E_0 \left|\phi_2\right\rangle}{\hbar} \mathrm{e}^{-\mathrm{i}(\omega+\omega_0)t} \right\} \\ \mathrm{i}\dot{c}_2 &= \frac{c_1}{2}\left\{ \frac{\left\langle\phi_2\right| er_- E_0 \left|\phi_1\right\rangle}{\hbar} \mathrm{e}^{\mathrm{i}(\omega+\omega_0)t} + \frac{\left\langle\phi_2\right| er_+ E_0 \left|\phi_1\right\rangle}{\hbar} \mathrm{e}^{-\mathrm{i}(\omega-\omega_0)t} \right\}. \end{aligned}$$

For the case where the radiation frequency is close to the atomic resonance, the magnitude of the detuning, $|\omega - \omega_0| \ll \omega_0$. The fast oscillat-

1 A circularly polarised electric field is chosen as it is a simultaneous eigenstate of the atom in the trap that will be used in the experiment. The eigenstates are good eigenstates even under the Zeeman and AC Stark shifts and thus will be a good two-level system.

ing term of $\omega + \omega_0$ averages out and can be neglected in the rotating-wave approximation giving,

$$\mathrm{i}\dot{c}_1 = \frac{c_2}{2}\Omega \mathrm{e}^{\mathrm{i}(\omega-\omega_0)t} \tag{5a}$$

$$\mathrm{i}\dot{c}_2 = \frac{c_1}{2}\Omega^* \mathrm{e}^{-\mathrm{i}(\omega-\omega_0)t}, \tag{5b}$$

with Rabi frequency

$$\Omega = \frac{\langle\phi_1 | er_- E_0 | \phi_2\rangle}{\hbar} = \frac{\left(\langle\phi_2 | er_+ E_0 | \phi_1\rangle\right)^*}{\hbar}. \tag{6}$$

The solution of equations 5 gives an oscillation of the expectation value of the population in the $|\phi_1\rangle$ and $|\phi_2\rangle$ or ground and excited states with effective Rabi frequency $\Omega' = \sqrt{\Omega^2 + \delta^2}$, (where δ is the detuning $\delta = \omega - \omega_0$), which continues on indefinitely. This is obviously not accurate as spontaneous emission will naturally reduce the population of the excited state and thus reducing the coherence between the ground and excited state, such that the oscillations damps out.

2.1.2 *Optical Bloch Equations*

To consider the actual steady-state population of the excited state, spontaneous emission needs to be included in the model. One simple way to do it, without going to a quantised description of the light field is to write down the optical Bloch equations and include decay terms to account for the decay due to spontaneous emission. The optical Bloch equations under the long-wavelength, electric dipole and rotating-wave approximation are[35]

$$\frac{\mathrm{d}}{\mathrm{d}t}\hat{\rho}_{22} = \mathrm{i}\frac{\Omega}{2}(\hat{\rho}_{21} - \hat{\rho}_{12}) - \Gamma\hat{\rho}_{22} \tag{7a}$$

$$\frac{\mathrm{d}}{\mathrm{d}t}\hat{\rho}_{11} = -\mathrm{i}\frac{\Omega}{2}(\hat{\rho}_{21} - \hat{\rho}_{12}) + \Gamma\hat{\rho}_{22} \tag{7b}$$

$$\frac{\mathrm{d}}{\mathrm{d}t}\hat{\rho}_{12} = -\mathrm{i}\delta\hat{\rho}_{12} - \mathrm{i}\frac{\Omega}{2}(\hat{\rho}_{22} - \hat{\rho}_{11}) - \frac{\Gamma}{2}\hat{\rho}_{12} \tag{7c}$$

$$\frac{\mathrm{d}}{\mathrm{d}t}\hat{\rho}_{21} = \mathrm{i}\delta\hat{\rho}_{12} + \mathrm{i}\frac{\Omega}{2}(\hat{\rho}_{22} - \hat{\rho}_{11}) - \frac{\Gamma}{2}\hat{\rho}_{21}, \tag{7d}$$

where Γ is the spontaneous decay rate, and $\hat{\rho}_{ij}$ are the elements of the density matrix operator and Ω is now assumed real. The steady-state solution ($t \to \infty$) for the excited state population is given by,

$$\rho_{22} = \frac{|\Omega|^2}{4\delta^2 + 2|\Omega|^2 + \Gamma^2}, \tag{8}$$

where it can be seen for a strong on-resonant continuous wave beam ($\Omega \gg \Gamma, \delta = 0$), the maximum excited state population achievable in the steady state is $\rho_{22}(t \to \infty) = 1/2$. The spontaneous decay rate in free space can be derived from Fermi's golden rule which gives

$$\Gamma = \frac{\omega_0^3 \left|\langle \phi_1 \left| er_- \right| \phi_2 \rangle\right|^2}{3\pi\varepsilon_0 \hbar c^3}. \tag{9}$$

$$= \frac{\hbar\omega_0^3}{3\pi\varepsilon_0 c^3}\left(\frac{\Omega}{E_0}\right)^2, \tag{10}$$

where the term in the bracket is actually a constant proportional to the dipole matrix element between states ϕ_1 and ϕ_2 or ground and excited state. The optical power scattered by the atom is given simply by the excited state population, decay rate and energy per photon [38]:

$$P_{\text{sc}} = \rho_{22}\Gamma\hbar\omega_0. \tag{11}$$

Combining equations 8 and 11 for an on-resonant beam ($\delta = 0$),

$$P_{\text{sc}} = \frac{\Omega^2}{2\Omega^2 + \Gamma^2}\Gamma\hbar\omega_0$$

$$= \frac{\frac{\Omega}{\Gamma}^2}{2\left(\frac{\Omega}{\Gamma}\right)^2 + 1}\hbar\omega_0, \tag{12}$$

and for a weak beam such that $\Omega \ll \Gamma$, and using equation 10, we see that the scattered power,

$$P_{\text{sc}} \approx \frac{\Omega^2}{\Gamma}\hbar\omega_0$$

$$= \frac{3\pi\varepsilon_0 c^3 E_0^2}{\omega_0^2}$$

$$= \frac{3\varepsilon_0 c\lambda^2 E_0^2}{4\pi}, \tag{13}$$

is quadratic with respect to the amplitude square of the electric field or linear in intensity. Thus, the power scattered of a weak beam by the atom is only a function of its wavelength and the electric field at the position of the atom.

A simple measure of interaction is the scattering cross section, σ, which for a two-level atom exposed to an on-resonant monochromatic plane wave is defined as [38]

$$\sigma = \frac{P_{\text{sc}}}{I}, \tag{14}$$

where I is the intensity of the incoming plane wave given by

$$I = \frac{1}{2}\varepsilon_0 c |E_0|^2 . \tag{15}$$

Combining equations 13, 14 and 15, the scattering cross section can be written as

$$\sigma_{\max} = \frac{3\lambda^2}{2\pi}. \tag{16}$$

The cross section has units of area and thus depends on the proportion of the electric field that is concentrated in that 'area'. A possible definition of scattering ratio is given by Zumofen et al. [39] as,

$$\mathcal{K}_0 = \frac{P_{\text{sc}}}{P_{\text{in}}} = \frac{\sigma_{\max}}{\mathcal{A}}, \tag{17}$$

where $\mathcal{A}$ represents the effective focal area and is calculated for various incoming geometries such as linearly polarised homogeneous plane waves and directional dipolar input waves as a function of the entrance half angle, as in the supplementary material of [39]. However, for a Gaussian beam, the entrance half angle is not a convenient quantity to measure. As such we introduce a similar but more convenient measure of scattering ratio which is a function of the waist of the incoming beam, defined as where the intensity drops to $1/e^2$ of the axial value.

2.1.3 *Gaussian beam*

Since a collimated circularly polarised probe from a single mode fibre with a TEM_{00} mode Gaussian profile is used in the experiment, choosing z as the propagation direction, the electric field has the form

$$\mathbf{E}_{\text{in}}(\rho, t) = \frac{E_L}{\sqrt{2}} [\cos(\omega t)\,\hat{\mathbf{x}} + \sin(\omega t)\,\hat{\mathbf{y}}] \exp\left(-\rho^2 / w_L^2\right), \tag{18}$$

where E_L is the electric field amplitude on the beam axis, ω is the oscillation frequency, ρ is the radial distance from the z-axis, w_L is the waist of the Gaussian beam. An ideal Gaussian beam has a transverse profile that extends to infinity, but a real one is limited by the finite aperture of the optics used. However the power at the wings of a beam that is clipped from an aperture of $\rho = 2w_0$ is less than 0.04 % and thus can safely be ignored. The time-averaged power of the beam is given by

$$P_{\text{in}} = \frac{1}{4}\pi\varepsilon_0 c E_L^2 w_L^2. \tag{19}$$

Using the definition of scattering ratio in equation 17, and substituting a Gaussian input (equation 19) and scattered power (equation 13) we obtain,

$$R_{\mathrm{sc}} = \frac{P_{\mathrm{sc}}}{P_{\mathrm{in}}} \tag{20}$$

$$= \frac{3\lambda^2}{\pi^2 w_L^2}\left(\frac{E_0}{E_L}\right)^2. \tag{21}$$

For a collimated beam focused by an ideal lens of focal length, f, the waist at the focus, within the paraxial approximation, is related to the waist at the input lens by,

$$w_0 = \frac{w_L}{\sqrt{1+\left(\frac{z_{\mathrm{R}}}{f}\right)^2}} \approx \frac{f\lambda}{\pi w_L}, \tag{22}$$

where $z_{\mathrm{R}} = \pi w_L^2/\lambda$ is the Rayleigh range of the beam before the lens and the approximation is valid for a focal length shorter than the Rayleigh range, $f \ll z_{\mathrm{R}}$. If all of the input beam power flows through the atom at the focus, the ratio of their powers is then

$$1 = \frac{P_0}{P_{\mathrm{in}}} = \left(\frac{E_0 w_0}{E_L w_L}\right)^2, \tag{23}$$

and thus equation 21 becomes

$$\begin{aligned} R_{\mathrm{sc}} &= \frac{3\lambda^2}{\pi^2 w_L^2}\left(\frac{w_L}{w_0}\right)^2 \\ &= \frac{3\lambda^2}{\pi^2 w_0^2} \\ &\approx 3\left(\frac{w_L}{f}\right)^2 \\ &= 3u^2, \end{aligned} \tag{24}$$

where the approximation in equation 22 was used and in the final line, a new parameter, the focusing strength was introduced, defined as

$$u \equiv \frac{w_L}{f}, \tag{25}$$

which is a measure of how strongly the beam is focused. For stronger focusing however, the electric field is not entirely concentrated at the focus and thus equation 23 is no longer applicable. This is because a single Gaussian mode is no longer sufficient to describe the beam.

The input beam polarisation is also converted to other polarisations that do not couple to the atom in the strong focusing limit since the polarised atom only couples to a particular electric field polarisation [33].

2.2 STRONG FOCUSING CASE

In the strong focusing case, the paraxial approximation breaks down and a new expression for the electric field at the focus is needed. Following the work of Tey et al. [33], the electric field after an ideal lens is written down such that it still satisfies Maxwell's equation. Once the field behind the ideal lens is known, it can be propagated to the focus either by decomposing the field into cylindrical modes and numerically propagating them or by using the Green's theorem.

To simplify the expressions in this section, the electric field is expressed in dimensionless units such that electric field strength of the collimated Gaussian beam entering the focusing lens is given by

$$\mathbf{F}_{\text{in}}(\rho, z) = \hat{\epsilon}_{+} \mathrm{e}^{-\rho^2/w_L^2} \mathrm{e}^{-\mathrm{i}kz}, \tag{26}$$

where $\hat{\epsilon}_{+}$ is one of the circular polarisation vectors $\hat{\epsilon}_{\pm} = (\hat{\mathbf{x}} \pm \mathrm{i}\hat{\mathbf{y}})/\sqrt{2}$, or in the cylindrical polarisation basis,

$$\mathbf{F}_{\text{in}}(\rho, \phi, z) = \frac{1}{\sqrt{2}} \left(\mathrm{e}^{\mathrm{i}\phi} \hat{\rho} + i \mathrm{e}^{\mathrm{i}\phi} \hat{\phi} \right) \mathrm{e}^{-\rho^2/w_L^2} \mathrm{e}^{-\mathrm{i}kz}, \tag{27}$$

where $\hat{\rho} = \cos\phi\hat{\mathbf{x}} + \sin\phi\hat{\mathbf{y}}$ and $\hat{\phi} = -\sin\phi\,\hat{\mathbf{x}} + \cos\phi\,\hat{\mathbf{y}}$ are the orthogonal polarisation vectors in the radial and azimuthal direction respectively and $k = 2\pi/\lambda$ is the wavevector amplitude along the propagation direction.

2.2.1 *Ideal lens transformation*

An ideal lens with focal length, f, will focus a collimated beam to the focus of the lens. In terms of wavefront, it converts a beam with a plane wavefront $\left(\mathrm{e}^{-\mathrm{i}kz}\right)$ into one with a spherical wavefront $\left(\mathrm{e}^{-\mathrm{i}k\sqrt{\rho^2+f^2}}\right)$ that converges towards the focal point F. This on its own however does not take into account the vector nature of the electric field. To set up a transformation that ideally converges the beam to the focal point and also satisfies Maxwell's equations, not only the wavefront, but the local polarisation of the electric field needs to be changed with three requirements in mind [40],

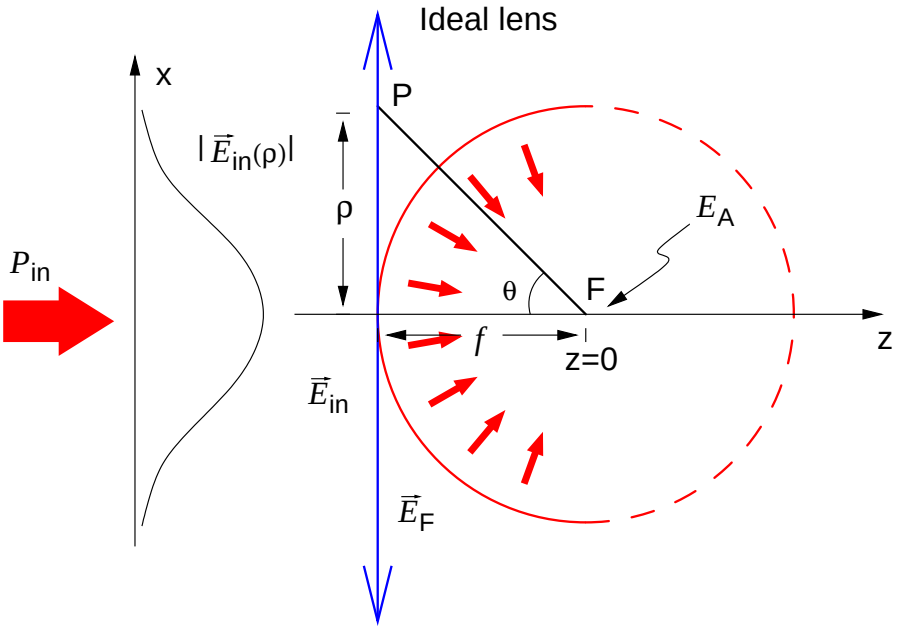

Figure 1: The electric field $\mathbf{E}_{in}$ of a collimated beam (planar wavefront) with a Gaussian profile is transformed into a focusing field $\mathbf{E}_F$ with a spherical wavefront by a thin ideal lens with a focal length f resulting in a field amplitude E_A at the focus of the lens.

1. A rotationally symmetric lens does not alter the local azimuthal field component, but only tilts the local radial polarisation component of the incoming field towards the axis
2. The electromagnetic field after the lens is still transverse and hence its polarisation orthogonal to the propagation direction, given by the normal of the wavefront
3. The power flowing into and out of an arbitrarily small area on the thin ideal lens is the same.

From condition 1, the radial polarisation vector after the lens is transformed by $\hat{\rho} \to \cos\theta\,\hat{\rho} + \sin\theta\,\hat{\mathbf{z}}$, where

$$\theta = \arctan(\rho/f) \tag{28}$$

as in figure 1. Condition 2 is automatically satisfied by the transformation and can be checked by writing the electric field in the spherical basis with centre at the focus and ensuring that the radial unit vector

$\hat{\mathbf{r}}$ is always zero[2]. The final condition is satisfied by multiplying the electric field by $1/\sqrt{\cos\theta}$.

Hence for an input field given by equation 26, the polarisation after the lens can be written as,

$$\mathbf{F}_{\mathrm{al}}(\rho,\phi,z=-f) = \frac{1}{\sqrt{\cos\theta}}\left(\frac{1+\cos\theta}{2}\hat{\epsilon}_{+} + \frac{\sin\theta}{\sqrt{2}}\mathrm{e}^{\mathrm{i}\phi}\,\hat{\mathbf{z}} + \frac{\cos\theta-1}{2}\mathrm{e}^{2\mathrm{i}\phi}\,\hat{\epsilon}_{-}\right)\times \mathrm{e}^{-\rho^2/w_L^2}\mathrm{e}^{-\mathrm{i}k\sqrt{\rho^2+f^2}}, \tag{29}$$

where $\hat{\epsilon}_{\pm}$ and $\hat{\mathbf{z}}$ are the three orthogonal polarisation vectors and θ as previously defined. As can be seen, for a real vector field, as the beam is more tightly focused (larger θ), other polarisation vector components start to appear. Once the electric field behind the lens is known, it can be propagated to the focus. One technique uses a decomposition of the electric field into complete orthogonal cylindrical modes to reconstruct the field at any point after the lens [41] while another is to use the Green's theorem which gives an analytical expression for the field at the focus.

2.2.2 *Field at the focus compatible with Maxwell equations*

From Green's theorem, it can be shown that for a given electric and magnetic fields $\mathbf{E}(\mathbf{r}')$ and $\mathbf{B}(\mathbf{r}')$ on an arbitrary closed surface S' that encloses a point $\mathbf{r}$, the electric field at the point is determined by [42]

$$\begin{aligned}\mathbf{E}(\mathbf{r}) &= \oint_{S'} \mathrm{d}A'\{ikc\,[\hat{\mathbf{n}}'\times\mathbf{B}(\mathbf{r}')]\,G(\mathbf{r},\mathbf{r}') + [\hat{\mathbf{n}}'\cdot\mathbf{E}(\mathbf{r}')]\,\nabla' G(\mathbf{r},\mathbf{r}') \\ &\quad + [\hat{\mathbf{n}}'\times\mathbf{E}(\mathbf{r}')]\times\nabla' G(\mathbf{r},\mathbf{r}')\}\end{aligned} \tag{30}$$

where $\hat{\mathbf{n}}'$ is the unit vector normal to the differential surface element $\mathrm{d}A'$ and points into the volume enclosed by S', and $G(\mathbf{r},\mathbf{r}')$ is the Green's function representing an outgoing spherical wave given by,

$$G(\mathbf{r},\mathbf{r}') = \frac{\mathrm{e}^{\mathrm{i}k|\mathbf{r}-\mathbf{r}'|}}{4\pi|\mathbf{r}-\mathbf{r}'|}. \tag{31}$$

If the point $\mathbf{r}$ is the focus of an aplanatic focusing field, then in the far field limit, i.e. when $|\mathbf{r}-\mathbf{r}'| \gg \lambda$, the incoming field propagation wave vector $\mathbf{k}'$ at any point $\mathbf{r}'$ always points towards the focus, $\mathbf{r}$. In

2 The angle θ in this formulation doesn't correspond to the inclination angle used in the standard spherical coordinates convention since it extends from the negative z direction. In order to convert to spherical coordinates and retain the same convention, either the transformation $\theta \to \pi - \theta$ or $\hat{\mathbf{z}} \to -\hat{\mathbf{z}}$ must be made.

this limit, the expressions for the magnetic field and the gradient of Green's function simplifies to,

$$\mathbf{B}(\mathbf{r}') \to \frac{\hat{\mathbf{k}}'}{c} \times \mathbf{E}(\mathbf{r}'), \tag{32a}$$

$$\nabla' G(\mathbf{r},\mathbf{r}') \to \mathrm{sgn}(z')\mathrm{i}\mathbf{k}' G(\mathbf{r},\mathbf{r}'), G \tag{32b}$$

where the $\mathrm{sgn}(z')$ is the sign function and is -1 for an $\mathbf{r}'$ before the focus and $+1$ for a position after. In this limit, and at the focus, equation 30 reduces to

$$\begin{aligned}
\mathbf{E}(\mathbf{r}_{\mathrm{focus}}) &= \oint_{S'} \mathrm{d}A' \Big\{ ik \left[\hat{\mathbf{n}}' \times \left(\hat{\mathbf{k}}' \times \mathbf{E}(\mathbf{r}')\right)\right] G(\mathbf{r},\mathbf{r}') + \mathrm{i}\,\mathrm{sgn}(z') G(\mathbf{r},\mathbf{r}') \left[\hat{\mathbf{n}}' \cdot \mathbf{E}(\mathbf{r}')\right] \mathbf{k}' \\
&\quad + \mathrm{i}\,\mathrm{sgn}(z') G(\mathbf{r},\mathbf{r}') \left[\hat{\mathbf{n}}' \times \mathbf{E}(\mathbf{r}')\right] \times \mathbf{k}' \Big\} \\
&= \oint_{S'} \mathrm{d}A' \mathrm{i} G(\mathbf{r},\mathbf{r}') \Big\{ \left[\left(\hat{\mathbf{n}}' \cdot \mathbf{E}(\mathbf{r}')\right) \mathbf{k}' - \left(\hat{\mathbf{n}}' \cdot \mathbf{k}'\right) \mathbf{E}(\mathbf{r}')\right] + \mathrm{sgn}(z') \left[\hat{\mathbf{n}}' \cdot \mathbf{E}(\mathbf{r}')\right] \mathbf{k}' \\
&\quad - \mathrm{sgn}(z') \left[\left(\mathbf{k}' \cdot \mathbf{E}(\mathbf{r}')\right) \hat{\mathbf{n}}' - \left(\mathbf{k}' \cdot \hat{\mathbf{n}}'\right) \mathbf{E}(\mathbf{r}')\right] \Big\} \\
&= \oint_{S'} \mathrm{d}A' \mathrm{i} G(\mathbf{r},\mathbf{r}') \Big[\left(\hat{\mathbf{n}}' \cdot \mathbf{E}(\mathbf{r}')\right) \left(1 + \mathrm{sgn}(z')\right) \mathbf{k}' \\
&\quad - \left(\hat{\mathbf{n}}' \cdot \mathbf{k}'\right) \left(1 - \mathrm{sgn}(z')\right) \mathbf{E}(\mathbf{r}') - \mathrm{sgn}(z') \left(\mathbf{k}' \cdot \mathbf{E}(\mathbf{r}')\right) \hat{\mathbf{n}}' \Big].
\end{aligned} \tag{33}$$

The last term in the equation is zero because the electric field is transverse. The closed surface S' can be divided into two parts, after and before the focus such that $\mathrm{sgn}(z')$ is either plus or minus one, giving,

$$\mathbf{E}(\mathbf{r}_{\mathrm{focus}}) = 2\mathrm{i} \int_{S_{\mathrm{af}}} \mathrm{d}A' G(\mathbf{r},\mathbf{r}') \left(\hat{\mathbf{n}}' \cdot \mathbf{E}(\mathbf{r}')\right) \mathbf{k}' - 2\mathrm{i} \int_{S_{\mathrm{bf}}} \mathrm{d}A' G(\mathbf{r},\mathbf{r}') \left(\hat{\mathbf{n}}' \cdot \mathbf{k}'\right) \mathbf{E}(\mathbf{r}'). \tag{34}$$

A large hemisphere is chosen as the surface after the focus such that the normal is orthogonal to the outgoing electric field (or parallel to $\mathbf{k}'$), i.e. $\hat{\mathbf{n}}' \cdot \mathbf{E}(\mathbf{r}') = 0$, and the first term vanishes. The other surface is chosen to be an infinitely large plane just after the ideal lens where the

dimensionless electric field is known as in equation 27. Performing the integral in the cylindrical basis and dropping the primes, we have,

$$\begin{aligned}
\mathbf{F}(\mathbf{r}_{\text{focus}}) &= \mathbf{F}(0,0,z=0) \\
&= -2\mathrm{i}\int_0^{\infty}\int_0^{2\pi} \rho \mathrm{d}\phi \mathrm{d}\rho \left(\frac{\mathrm{e}^{\mathrm{i}k\sqrt{f^2+\rho^2}}}{4\pi\sqrt{f^2+\rho^2}}\right)\left(|\hat{\mathbf{n}}|\left|\hat{\mathbf{k}}\right|k\cos\theta\right)\times \\
&\quad \frac{1}{\sqrt{\cos\theta}}\left(\frac{1+\cos\theta}{2}\hat{\epsilon}_+ + \frac{\sin\theta \mathrm{e}^{\mathrm{i}\phi}}{\sqrt{2}}\hat{\mathbf{z}} + \frac{\cos\theta-1}{2}\mathrm{e}^{2\mathrm{i}\phi}\hat{\epsilon}_-\right)\times \\
&\quad \mathrm{e}^{-\rho^2/w_L^2}\mathrm{e}^{-\mathrm{i}k\sqrt{\rho^2+f^2}} \\
&= \frac{-\mathrm{i}k\sqrt{f}}{2}\int_0^{\infty}\mathrm{d}\rho \frac{\rho\left(f+\sqrt{f^2+\rho^2}\right)}{\left(f^2+\rho^2\right)^{5/4}}\mathrm{e}^{-\rho^2/w_L^2}\hat{\epsilon}_+, \qquad (35)
\end{aligned}$$

where in the second step, the ϕ integral leaves only the right-hand circular polarisation term and θ is as defined in equation 28. The integral has an analytical solution and equation 35 becomes,

$$\mathbf{F}(\mathbf{r}_{\text{focus}}) = -\frac{1}{4}\frac{\mathrm{i}kw_L}{u}\mathrm{e}^{1/u^2}\left[\frac{1}{\sqrt{u}}\Gamma\left(-\frac{1}{4},\frac{1}{u^2}\right)+\sqrt{u}\Gamma\left(\frac{1}{4},\frac{1}{u^2}\right)\right]\hat{\epsilon}_+, \qquad (36)$$

with the upper incomplete gamma function,

$$\Gamma(a,x) \equiv \int_x^{\infty} t^{a-1}\mathrm{e}^{-t}\mathrm{d}t, \qquad (37)$$

and the focusing strength is as defined in equation 25. The –i term reflects Gouy phase of $-\pi/2$ that the field picks up when it reaches the focus [40]. The electric field dimensions can now be restored by multiplying by the amplitude at the centre of the collimated Gaussian beam E_L, which can be expressed in terms of the optical power as

$$E_L = \frac{1}{w_L}\sqrt{\frac{4P_{\text{in}}}{\varepsilon_0\pi c}}, \qquad (38)$$

resulting in an electric field at the focus of the form

$$\mathbf{E}(\mathbf{r}_{\text{focus}}) = -\frac{\mathrm{i}}{u}\mathrm{e}^{1/u^2}\sqrt{\frac{\pi P_{\text{in}}}{\varepsilon_0 c\lambda^2}}\left[\frac{1}{\sqrt{u}}\Gamma\left(-\frac{1}{4},\frac{1}{u^2}\right)+\sqrt{u}\Gamma\left(\frac{1}{4},\frac{1}{u^2}\right)\right]\hat{\epsilon}_+. \qquad (39)$$

As can be seen, the electric field depends only on the input power P_{in}, wavelength λ, and the focusing strength u.

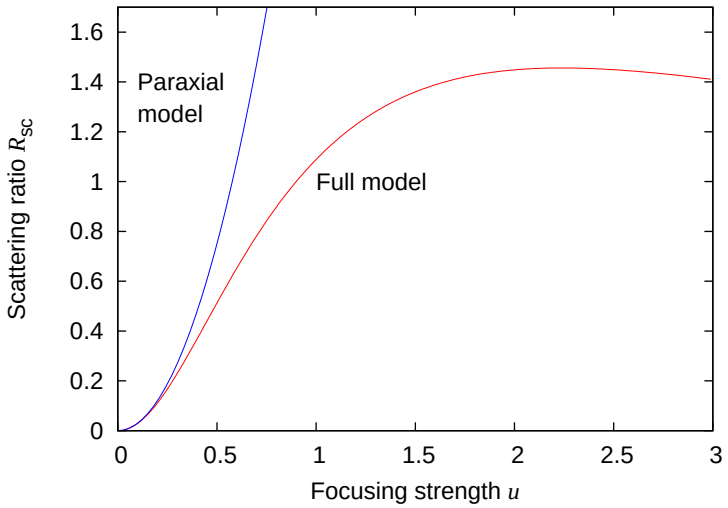

Figure 2: Scattering ratio, R_{sc}, as a function of the focusing parameter, u, using the paraxial approximation and the full model, for an atom stationary at the focus of an ideal lens.

2.2.3 *Scattering ratio*

The scattering ratio in equation 21 can now be re-evaluated in terms of the field amplitude at the focus from equations 39 and 38 to obtain,

$$\begin{aligned} R_{sc} &= \frac{3\lambda^2}{\pi^2 w_L^2}\left(\frac{1}{4}\frac{2\pi w_L}{u\lambda}e^{1/u^2}\left[\frac{1}{\sqrt{u}}\Gamma\left(-\frac{1}{4},\frac{1}{u^2}\right)+\sqrt{u}\Gamma\left(\frac{1}{4},\frac{1}{u^2}\right)\right]\right)^2 \\ &= \frac{3}{4u^3}e^{2/u^2}\left[\Gamma\left(-\frac{1}{4},\frac{1}{u^2}\right)+u\Gamma\left(\frac{1}{4},\frac{1}{u^2}\right)\right]^2, \end{aligned} \tag{40}$$

where it is now just a function of a single focusing parameter. The scattering ratio is thus just a measure of how efficiently one can convert a beam with a Gaussian profile into a directional dipole wave profile. As seen in figure 2, the value of the scattering ratio exceeds one, which from the definition of equation 20 might initially suggest that there's more light being scattered away from the atom than going in. However this is clearly unphysical and it should be noted that the field that is scattered by the atom is still coherent with the field of the input beam and will interfere destructively. Thus energy conversation is still maintained as will be shown in section 2.3.2 as was shown in several literature [43, 44]. The physical bound for light coming in from one direction is, $R_{sc} \leq 2$, given by the Bassett limit [45]. For this focusing model of the Gaussian beam using an ideal lens, a maximal value of $R_{sc} = 1.456$ for a focusing strength $u = 2.239$ is obtained. For an even larger focusing strength, the value of the scattering ratio starts to

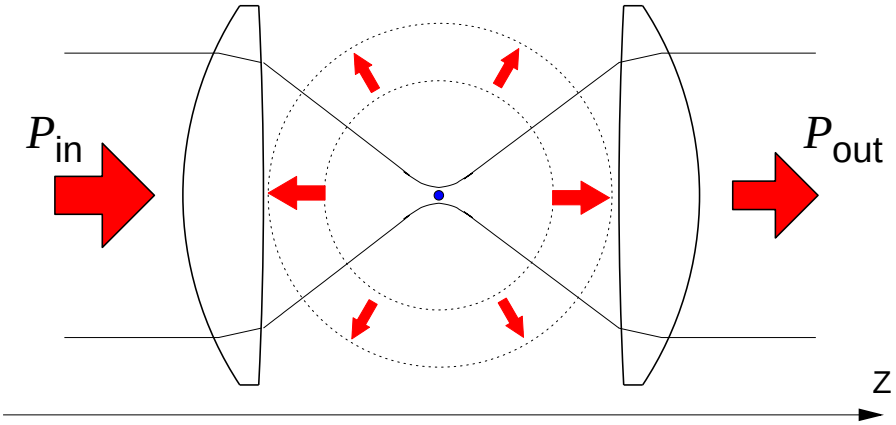

Figure 3: A transmission measurement setup with an atom at the focus of two confocal lenses. The transmitted power, P_{out}, is the result of interference between the scattered light and the input probe light in the case of coherent scattering.

decrease slowly as the electric field amplitude in the $\hat{\epsilon}_+$ polarisation at the point of the atom reduces due to over focusing.

To obtain a larger value of the scattering ratio from a Gaussian beam, a different transformation needs to be done, one where not only an ideal lens is used, but also transformations that change the amplitude profile of the beam to better match the directional dipole wave [39].

2.3 MEASURE OF SCATTERING RATIO

The scattering ratio can be used as a figure of merit for scattering experiments. It is however not a quantity that can be measured directly, unless there is a detector that can cover the whole 4π solid angle. In this section, the form of the scattered field of the atom and the experimentally accessible quantities of transmission, reflection and induced phase shift will be discussed. It will be shown that all these quantities can be expressed using the scattering ratio and detuning as parameters. The idea of the experiments that will be conducted is illustrated in figure 3. A weak coherent probe is focused to the atom and recollected again by the second lens. Also collected by the second lens is the field scattered by the atom which interferes with the probe for coherent scattering.

2.3.1 *Scattered field*

The field scattered by the atom is that of the rotating electric dipole [42], with an amplitude that is proportional to the excitation probe

field amplitude, E_0, and the total power contained in the dipole radiation is equal to the power scattered by the atom as in equation 13. In the far field ($r \gg \lambda$), the field scattered by the atom is

$$\mathbf{E}_{\mathrm{sc}}(\mathbf{r}) = \frac{3E_0 \mathrm{e}^{\mathrm{i}(kr+\pi/2)}}{2kr}\left[\hat{\epsilon}_+ - (\hat{\epsilon}_+ \cdot \hat{\mathbf{r}})\,\hat{\mathbf{r}}\right], \tag{41}$$

where $\hat{\mathbf{r}}$ is the radial unit vector pointing away from the atom [35] or in the cylindrical convention used in this chapter,

$$\mathbf{E}_{sc}(\rho,\phi,z) = \frac{3E_0 \mathrm{e}^{\mathrm{i}\left(k\sqrt{\rho^2+z^2}+\pi/2\right)}}{8k\sqrt{\rho^2+z^2}}\Big[(3+\cos 2\theta)\,\hat{\epsilon}_+ + \sqrt{2}\sin 2\theta\,\mathrm{e}^{\mathrm{i}\phi}\hat{\mathbf{z}} + (\cos 2\theta - 1)\,\mathrm{e}^{2\mathrm{i}\phi}\hat{\epsilon}_-\Big], \tag{42}$$

where θ is as defined in equation 28 . The phase term of $\pi/2$ reflects the fact that the field scattered by the atom lags the probe field by $\pi/2$ on resonance. From equation 29, the probe field at the lenses at $z = \mp f$ are,

$$\mathbf{E}_{\mathrm{ls}}(\rho,\phi,z=\mp f) = \frac{E_L}{\sqrt{\cos\theta}}\left(\frac{1+\cos\theta}{2}\hat{\epsilon}_+ + \frac{\sin\theta}{\sqrt{2}}\mathrm{e}^{\mathrm{i}\phi}\hat{\mathbf{z}} + \frac{\cos\theta-1}{2}\mathrm{e}^{2\mathrm{i}\phi}\hat{\epsilon}_-\right)\times \mathrm{e}^{\mp\mathrm{i}\left(k\sqrt{\rho^2+f^2}-\pi/2\right)}\mathrm{e}^{-\rho^2/w_L^2}, \tag{43}$$

where the incoming phase (at $z = -f$) is adjusted with the additional $\pi/2$ term such that the electric field at the location of the atom is real and positive[3] and at the second lens after the focus the field picks up an overall Gouy phase of $-\pi$. It can be seen from the above equations that on the z-axis ($\rho, \phi = 0$), the probe field and the forward scattered field are out of phase and interfere destructively. This was shown by Zumofen et al. [39] for any arbitrary incident fields.

2.3.2 *Energy flux*

Since the scattered field is still coherent with the incident probe field, the measure of the energy flux going in and out of the system needs to be evaluated from the final superposition of both fields. The intensity of the field can be determined from the time-averaged Poynting vector,

$$\langle \mathbf{S} \rangle = \frac{1}{T}\varepsilon_0 c^2 \int_0^T \mathrm{d}t\, \Re\mathfrak{e}\left(\mathbf{E}(\mathbf{r},t) \times \mathbf{B}^*(\mathbf{r},t)\right), \tag{44}$$

3 The scattered electric field was derived for an incoming electric field that is real at the location of the atom. Thus equation 39 is made real by adding an additional phase.

where far away from the focus, the wavefront can be locally approximated by a plane wave such that $\mathbf{B} = \hat{\mathbf{k}} \times \mathbf{E}/c$, and equation 44 becomes,

$$\langle \mathbf{S} \rangle = \frac{\varepsilon_0 c}{2} \Re\mathfrak{e} \left| \mathbf{E}(\mathbf{r}) \right|^2 \hat{\mathbf{k}}, \tag{45}$$

where $\mathbf{E}(\mathbf{r}) = \mathbf{E}_{\text{ls}} + \mathbf{E}_{\text{sc}}$ is the electric field due to the superposition of the two fields. The power that flows through the system can ideally be evaluated at any surface that bounds it. Although both the probe and the scattered field have a spherical wavefront, the power that flows through the system is evaluated at the infinite planes at $z = \mp f$, because the probe field is completely defined at those positions. The propagation directions are opposite before the focus, $\hat{\mathbf{k}}_{\text{ls}} = -\hat{\mathbf{k}}_{\text{sc}}$ and the same after the focus, $\hat{\mathbf{k}}_{\text{ls}} = \hat{\mathbf{k}}_{\text{sc}}$, thus giving,

$$\begin{aligned} P(z = \mp f) &= \int_S \langle \mathbf{S} \rangle \cdot \mathrm{d}\mathbf{A} \\ &= \frac{\varepsilon_0 c}{2} \int_S \Re\mathfrak{e} \left| \mathbf{E}(\mathbf{r}) \right|^2 \hat{\mathbf{k}}_{\text{ls}} \cdot \hat{\mathbf{z}} \, \mathrm{d}A \\ &= \frac{\varepsilon_0 c}{2} \int_0^{\infty} \int_0^{2\pi} \rho \mathrm{d}\phi \mathrm{d}\rho \, \Re\mathfrak{e} \left(|\mathbf{E}_{\text{ls}}|^2 \mp |\mathbf{E}_{\text{sc}}|^2 + \mathbf{E}_{\text{ls}} \mathbf{E}_{\text{sc}}^* \mp \mathbf{E}_{\text{sc}} \mathbf{E}_{\text{ls}}^* \right) \cos\theta, \end{aligned} \tag{46}$$

where $\hat{\mathbf{k}}_{\text{ls}} \cdot \hat{\mathbf{z}} = \cos\theta$ is the projection of the spherical wavefront on the plane at $z = \mp f$. The first two terms of the integral can be easily shown to be equal to

$$|\mathbf{E}_{\text{ls}}|^2 = E_L^2 \frac{\mathrm{e}^{-2\rho^2/w_L^2}}{\cos\theta}, \qquad |\mathbf{E}_{\text{sc}}|^2 = \frac{9E_0^2}{8k^2} \frac{1}{\rho^2 + f^2} \left(1 + \frac{f^2}{\rho^2 + f^2} \right), \tag{47}$$

while the last two terms can be expanded to get

$$\mathbf{E}_{\text{ls}} \mathbf{E}_{\text{sc}}^* \mp \mathbf{E}_{\text{sc}} \mathbf{E}_{\text{ls}}^* = \frac{3E_0 E_L \mathrm{e}^{-\rho^2/w_L^2}}{2k\sqrt{\rho^2 + f^2}\sqrt{\cos\theta}} (1 + \cos\theta) \begin{cases} (-2\mathrm{i}\sin\alpha) & \text{for } -f \\ (2\cos\alpha) & \text{for } +f \end{cases}, \tag{48}$$

where

$$\alpha = \begin{cases} 2k\sqrt{\rho^2 + f^2} & \text{for } -f \\ \pi & \text{for } +f \end{cases}. \tag{49}$$

The terms in equation 46 are the power of the input probe, scattered power and the power due to the interference terms respectively. Evaluating the integral before the lens we have,

$$\begin{aligned} P(z=-f) &= \frac{1}{4}\varepsilon_0 c\pi E_L^2 w_L^2 - \frac{3}{8\pi}\varepsilon_0 c E_0^2 \lambda^2 \\ &= P_{\text{in}} - \frac{1}{2}P_{\text{sc}}, \end{aligned} \tag{50}$$

where the interference term is zero because it is completely imaginary, and the relations from equations 19 and 13 are used. And after the lens, the integral gives

$$\begin{aligned} P(z=+f) &= P_{\text{in}} + \frac{1}{2}P_{\text{sc}} - \frac{\varepsilon_0 c}{2}\frac{3E_0 E_L}{2k}\frac{2\pi f}{2}\mathrm{e}^{1/u^2}\left[\frac{1}{\sqrt{u}}\Gamma\left(-\frac{1}{4},\frac{1}{u^2}\right) + \sqrt{u}\Gamma\left(\frac{1}{4},\frac{1}{u^2}\right)\right] \\ &= P_{\text{in}} + \frac{1}{2}P_{\text{sc}} - \frac{3}{4\pi}\varepsilon_0 c E_0^2 \lambda^2 = P_{\text{in}} - \frac{1}{2}P_{\text{sc}}, \end{aligned} \tag{51}$$

where the integral of equation 48 is done in the same way as that of equation 35 and the field at the lens, E_L is related to the field at the focus by equations 38 and 39. The power that flows through both planes at $z = \mp f$ are the same. Thus the total energy is conserved and there is no apparent violation as discussed in section 2.2.3.

2.3.3 *Transmission/Extinction*

A simple transmission measurement is given by the ratio of the power transmitted through the lenses when the atom is in to when it is not, $P_{\text{out}}/P_{\text{in}}$, where P_{out} is the total power measured by a detector placed after the setup. For a symmetrical setup as in figure 3, the detector typically covers the same mode as the probe beam[4]. This mode, $\mathbf{g}$, then can be used to carry out projections of an electric field $\mathbf{E}$ to get the following scalar product,

$$\langle \mathbf{g}, \mathbf{E} \rangle \equiv \frac{\varepsilon_0 c}{2}\int_{\mathbf{r}\in S} \{\mathbf{g}^*(\mathbf{r}) \cdot \mathbf{E}(\mathbf{r})\}\left(\hat{\mathbf{k}}_{\mathbf{g}} \cdot \hat{\mathbf{n}}\right) \mathrm{d}A, \tag{52}$$

where S is the integration plane, $\hat{\mathbf{k}}_{\mathbf{g}}$ is the local propagation direction of the mode function $\mathbf{g}$, and $\hat{\mathbf{n}}$ is the normal vector on the plane S. The integration can be carried out at any convenient plane such that it covers the mode function, such as the plane $z = +f$, immediately before the second lens, thus having a similar form as the earlier integral in equation 46. The target mode function $\mathbf{g}_T$ is defined to be the

4 The probe beam with a Gaussian profile is usually derived from a single-mode optical fibre. If the whole setup is symmetric, the beam can then be ideally coupled back into a similar single-mode optical with a very high efficiency.

same as that of the incoming probe mode of $\mathbf{E}_{\text{ls}}$ in equation 43. With a normalisation condition of $\langle \mathbf{g}_T, \mathbf{g}_T \rangle = 1$, the mode function can be set as

$$\mathbf{g}_T = \frac{\mathbf{E}_{\text{ls}}}{\sqrt{P_{\text{in}}}}. \tag{53}$$

With this normalisation, the square of the projection in equation 52 has the dimension of power and thus the optical power of the probe that is scattered by the atom and coupled into a single mode fibre is

$$\begin{aligned} P_{\text{out}} &= |\langle \mathbf{g}_T, \mathbf{E} \rangle|^2 \\ &= |\langle \mathbf{g}_T, \mathbf{E}_{\text{ls}} + \mathbf{E}_{\text{sc}} \rangle|^2 \\ &= \left| \sqrt{P_{\text{in}}} - \frac{P_{\text{sc}}/2}{\sqrt{P_{\text{in}}}} \right|^2. \end{aligned} \tag{54}$$

The transmission is then given by,

$$\begin{aligned} T &= \frac{P_{\text{out}}}{P_{\text{in}}} \\ &= \left| 1 - \frac{P_{\text{sc}}}{2P_{\text{in}}} \right|^2 \\ &= \left| 1 - \frac{R_{\text{sc}}}{2} \right|^2. \end{aligned} \tag{55}$$

For a maximal $R_{\text{sc}} = 1.456$ corresponding to a $u = 2.239$, a minimum transmission of $T_{\text{min}} = 0.074$. Experimentally, the transmission is measured not just at the peak but by scanning the probe beam detuning, Δ, across the resonance frequency of the transition, resulting a Lorentzian profile[5]. The transmission, as a function of detuning, is now,

$$T(\Delta) = 1 - \frac{\Gamma^2 R_{\text{sc}} \left(1 - \frac{R_{\text{sc}}}{4}\right)}{4(\Delta - \Delta_0)^2 + \Gamma^2}, \tag{56}$$

where Δ_0 is the perturbed detuning of the transition away from zero and Γ is the spontaneous decay rate of the transition which determines the natural line width of the transition without any power or Doppler broadening. By fitting a transmission spectrum of a two-level atom, the quantity R_{sc} can thus be extracted.

5 The Lorentzian term of $\frac{i\Gamma}{2(\Delta-\Delta_0)+i\Gamma}$ is multiplied to the scattered field only since that is the term dependent on detuning.

2.3.4 *Reflection*

The light that is missing from the transmission goes into spatial modes not covered by the forward detector. A convenient mode to detect part of this missing light would be that of the incoming probe, but in the opposite direction, i.e. the part of the light that is reflected backwards. This is because it has the same spatial mode profile as the probe. The integration plane of equation 52 is now chosen to be at $z = -f$ and with a mode function $\mathbf{g}_R$ that has the same form as $\mathbf{g}_T$ in equation 53 but with $k \to -k$. The reflected power is then

$$\begin{aligned} P_{\text{rft}} &= |\langle \mathbf{g}_R, \mathbf{E} \rangle|^2 \\ &= |\langle \mathbf{g}_R, \mathbf{E}_{\text{ls}} + \mathbf{E}_{\text{sc}} \rangle|^2 \\ &= \frac{P_{\text{sc}}^2}{4P_{\text{in}}}, \end{aligned} \tag{57}$$

where the projection of $\langle \mathbf{g}_R, \mathbf{E}_{\text{ls}} \rangle$ is zero because they have opposite k vectors. Reflection can thus be defined as

$$R = \frac{P_{\text{rft}}}{P_{\text{in}}} = \frac{R_{\text{sc}}^2}{4}. \tag{58}$$

And similarly as a function of detuning,

$$R(\Delta) = \frac{\Gamma^2 \left(\frac{R_{\text{sc}}^2}{4} \right)}{4 \left(\Delta - \Delta_0 \right)^2 + \Gamma^2}. \tag{59}$$

For a maximal $R_{\text{sc}} = 1.456$, a maximum reflection of $R_{\text{max}} = 53\%$ can be expected. A perfect reflection can be expected for an incoming directional dipole wave [39] which requires an $R_{\text{sc}} = 2$ but that cannot be achieved by coming with a probe with a Gaussian profile and a simple lens transformation.

2.3.5 *Phase shift*

The third independent measure of the scattering ratio is the phase shift that is induced on the probe by the atom. This phase shift is due to the interference of the scattered field and the incoming probe. The phase shift is a function of detuning as is given by the argument of the complex ratio of the projected fields in the forward direction which has the form,

$$\delta\phi(\Delta) = \arg\left(\frac{\langle \mathbf{g}_T, \mathbf{E}_{\mathrm{ls}} + \mathbf{E}_{\mathrm{sc}} \rangle}{\langle \mathbf{g}_T, \mathbf{E}_{\mathrm{ls}} \rangle}\right)$$
$$= \arg\left(1 - \frac{R_{\mathrm{sc}}}{2} \frac{i\Gamma}{2(\Delta - \Delta_0) + i\Gamma}\right). \tag{60}$$

It should be noted that on resonance, the scattered field is completely out of phase with the probe (at and after the second lens $z \geq +f$) and thus interferes destructively. This will just result in a decrease of the power of the probe (extinction) but no apparent phase shift of the probe. The maximal phase shift occurs at a detuning that is half the linewidth of the transition, $|\Delta - \Delta_0| = \Gamma/2$. And for an $R_{\mathrm{sc}} = 1.456$, the maximum achievable phase shift is $\delta\phi(\frac{\Gamma}{2}) = 30°$. Although this measurement is ideally independent of the other two techniques, in practice, it is not possible to measure the phase of the probe beam directly since the oscillation frequency is too fast. Thus the phase is measured in an interferometric setup with a local oscillator as a phase reference. Extracting the phase shift of the beam from the interferrogram then requires knowledge of the transmission/extinction of the probe since it is derived from the output of the interferometer. This will be discussed further in section 3.3.2.

2.4 FINITE TEMPERATURE

The theory presented so far works nicely for an atom that is stationary at the focus of the ideal lens. However, for a real atom with a finite temperature in a harmonic trap, the atom position fluctuates and its velocity is non-zero. Since there is only a single atom, the temperature here does not refer to the average kinetic energy of an ensemble, but rather the average kinetic energy averaged over many different loadings of the atom into the dipole trap. This will contribute to three effects namely, the atom not sitting at the maximum electric field at the focus, Doppler shift of the incoming probe beam and finally position dependent energy level shifts due to the harmonic potential of the trap. The first two effects were considered by Teo and Scarani [34] to come up with a final temperature of the atom in the trap. This will be discussed briefly in the following sections.

2.4.1 *Electric field around the focus*

Since the atom is no longer stationary at the focus, the electric field of the probe now needs to be evaluated at all positions where the atom

can be. This was done in [34] by solving for the Dyadic Green's function defined as,

$$\nabla \times (\nabla \times \mathbf{G}) - k^2 \mathbf{G} = \mathbf{1}\delta(\mathbf{r} - \mathbf{r}'), \tag{61}$$

where $\mathbf{G}$ is the given by,

$$\mathbf{G} = \left(\mathbf{1} + \frac{\nabla\nabla}{k^2}\right) G(\mathbf{r}, \mathbf{r}'), \tag{62}$$

where $G(\mathbf{r}, \mathbf{r}')$ is defined as equation 31. The electric field is then

$$\mathbf{E}(\mathbf{r}) = \int_S \mathrm{d}S'(\mathrm{i}k) \frac{\mathrm{e}^{\mathrm{i}kR}}{2\pi R} \begin{pmatrix} -\frac{z}{R} & 0 & 0 \\ 0 & -\frac{z}{R} & 0 \\ \frac{x'-x}{R} & \frac{y'-y}{R} & 0 \end{pmatrix} \mathbf{E}(\mathbf{r}'), \tag{63}$$

where S is the plane where the electric field is known completely, the displacement $R = |\mathbf{r} - \mathbf{r}'|$, and the focus is once again assumed to be in the far field limit as was done in equation 32.

2.4.2 *Non-stationary atom in a trap*

In the experiment, the atom is trapped in an far off-resonant optical dipole trap. The potential induced by the dipole trap is approximately harmonic close to the minima and can be approximated by equation 85. In this conservative harmonic potential, the kinetic and potential energy sum to a constant value, which is the total energy of the atom, $E_K + E_P = E_T$. The total energy of the atom depends on the loading technique. For an atom that is loaded from a cloud of cold atoms at average temperature T_{cloud}, the loaded atom in the trap will have a total energy that follows the Boltzmann distribution that is truncated by the maximum depth of the trap. Thus, for each energy in the distribution, the atom will experience a different average position uncertainty and thus a position averaged electric field. Doppler broadening is also present due to the finite velocity of the atom in the trap. However, since the electric field is propagating in the z direction, the main contribution of the Doppler shift will be in this direction. The maximum velocity of the atom is when its potential energy is zero and thus

$$v_{\max} = \sqrt{\frac{2E_T}{m}}, \tag{64}$$

where m is the mass of the atom and the Doppler shift to the lowest order is given by v/λ. For a maximum energy on the order of the trap depth used ($\approx k_{\mathrm{B}} \cdot 1\,\mathrm{mK}$) the Doppler shift experienced is less than

10 % of the linewidth of the probed atomic transition. Thus the momentum distribution will only broaden the measured features slightly and should not contribute much to R_{sc}. The position distribution of the atom is that of a particle in a harmonic oscillator potential where a simpler classical treatment is employed due to the high estimated temperature ($\approx 100\,\mu K$) of the atom.

2.4.3 *Position averaged R_{sc}*

Once the electric field of the probe is known at all locations around the atom and the atomic distribution is known, the average scattering ratio can be evaluated by using a classical canonical ensemble to describe the system. Thus R_{sc} which depends on the electric field at the position of the atom can be averaged using

$$\begin{aligned}\langle f(\mathbf{r}_{atom}, \mathbf{p}_{atom})\rangle &\approx \frac{1}{Z}\int e^{-\frac{H}{k_B T}} f(\mathbf{r}_{atom}, \mathbf{p}_{atom})\, d^3p\, d^3r \\ &\approx \frac{1}{Z}\int e^{-\frac{V(\mathbf{r}_{atom})}{k_B T}} f(\mathbf{r}_{atom})\, d^3r, \end{aligned} \tag{65}$$

where the momentum dependence is dropped and Z is the partition function of the system described by the classical Hamiltonian $H = \frac{p^2}{2m} + V(\mathbf{r}_{atom})$.

2.5 PULSED EXCITATION OF A SINGLE ATOM

The theory discussed so far is only applicable in the steady state solution where the probability that the atom is in the excited state never exceeds 0.5. For a pulsed probe, this is clearly not the case since for a π-pulse, an atom in the ground state can be brought to the excited state with probability close to unity. In this section, we follow the work of Wang et al. [3] on excitation of a two-level atom by a single photon in a propagating mode. In this treatment, the electric field is quantised.

2.5.1 *Quantised electric field*

Quantisation of the electric field is typically done in a cavity where the mode function is well defined by the discrete modes of the cavity. In free space however, the modes are no longer discrete but rather is a

continuum, $\mathbf{k}$. In the Coulomb gauge, the positive-frequency parts of the electric-field operator can be written as [3, 46]

$$\hat{\mathbf{E}}^{(+)}(\mathbf{r},t) = i\sum_{\lambda}\int \mathrm{d}^3\mathbf{k}\sqrt{\frac{\hbar\omega_k}{(2\pi)^3 2\varepsilon_0}}\hat{a}_{\mathbf{k},\lambda}\boldsymbol{\epsilon}_{\mathbf{k},\lambda}u_{\mathbf{k},\lambda}(\mathbf{r})e^{-i\omega_k t}, \tag{66}$$

where $\omega_k = c|\mathbf{k}|$, $\boldsymbol{\epsilon}_{\mathbf{k},\lambda}(\lambda = 1,2)$ are the unit polarisation vectors of the mode such that $\boldsymbol{\epsilon}_{\mathbf{k},\lambda}\cdot\boldsymbol{\epsilon}_{\mathbf{k},\lambda'} = \delta_{\lambda,\lambda'}$, $\boldsymbol{\epsilon}_{\mathbf{k},\lambda}\cdot\mathbf{k} = 0$ and the field operators follow the usual commutation relation

$$\left[\hat{a}_{\mathbf{k},\lambda}, \hat{a}^{\dagger}_{\mathbf{k}',\lambda'}\right] = \delta(\mathbf{k}-\mathbf{k}')\delta_{\lambda,\lambda'}. \tag{67}$$

The spatial mode functions $u_{\mathbf{k},\lambda}(\mathbf{r})$ are normalised as

$$\int \mathrm{d}^3\mathbf{r}\, u^{*}_{\mathbf{k},\lambda}(\mathbf{r})\cdot u_{\mathbf{k}',\lambda'}(\mathbf{r}) = \delta(\mathbf{k}-\mathbf{k}')\delta_{\lambda,\lambda'}, \tag{68}$$

to preserve energy conservation. In the interaction picture, and after invoking the rotating-wave and dipole approximation, the interaction Hamiltonian can be written as,

$$\hat{H}_I = -\hbar\sum_{\lambda}\int \mathrm{d}^3\mathbf{k}\left[g_{\mathbf{k},\lambda}(\mathbf{r}_a)\hat{\sigma}_{+}\hat{a}_{\mathbf{k},\lambda}e^{-i(\omega_k-\omega_a)t} - \mathrm{H.c.}\right], \tag{69}$$

where $\hbar\omega_a$ is the atomic transition energy, $\hat{\sigma}_{+} = |e\rangle\langle g|$ is the atomic operator that brings the atom from ground to excited state and the spatial mode function of the field is now contained in the coupling strength term,

$$g_{\mathbf{k},\lambda}(\mathbf{r}_a) = d\sqrt{\frac{\omega_k}{(2\pi)^3 2\hbar\varepsilon_0}}u_{\mathbf{k},\lambda}(\mathbf{r}_a)\,\mathbf{e}_d\cdot\boldsymbol{\epsilon}_{\mathbf{k},\lambda}, \tag{70}$$

where d is the atomic dipole moment amplitude and $\mathbf{e}_d$ is the dipole unit vector.

2.5.2 *Dynamics*

From this Hamiltonian, the evolution of the atomic operators, $\hat{\sigma}_{\pm}$ and $\hat{\sigma}_z = |e\rangle\langle e| - |g\rangle\langle g|$ is governed by a set of coupled Heisenberg equations. A set of modified optical Bloch equations can then be written as,

$$\dot{\hat{\sigma}}_z = -\Gamma(\hat{\sigma}_z + 1) - 2\sum_{\lambda}\int \mathrm{d}^3\mathbf{k}\left[g_{\mathbf{k},\lambda}(\mathbf{r}_a)\hat{\sigma}_{+}\hat{a}_{\mathbf{k},\lambda}(t_0)e^{-i(\omega_k-\omega_a)t} + \mathrm{H.c}\right] + \hat{\zeta}_z, \tag{71}$$

$$\dot{\hat{\sigma}}_- = -\frac{\Gamma}{2}\hat{\sigma}_- + \hat{\sigma}_z \sum_\lambda \int \mathrm{d}^3\mathbf{k} \left[g_{\mathbf{k},\lambda}(\mathbf{r}_a)\hat{a}_{\mathbf{k},\lambda}(t_0)e^{-i(\omega_k-\omega_a)t}\right] + \hat{\zeta}_-, \quad (72)$$

where $\hat{\zeta}$ are noise operators, introduced to account for the interaction of the atom with the environment, and the spontaneous decay rate in free space $\Gamma = \Gamma' + \Gamma_p$ is made up of the sum of the decay into the environment Γ' and the pulse mode Γ_p. The evolution of the $\hat{\sigma}_+$ operator is obtained by taking the Hermitian conjugate of equation 72 for the $\hat{\sigma}_-$ operator. Using the Wigner-Weisskopf theorem, the explicit formula for Γ_p is given by,

$$\Gamma_p = 2\pi \sum_\lambda \int \mathrm{d}^3\mathbf{k} \left| g_{\mathbf{k},\lambda}(\mathbf{r}_a)\right|^2 \delta(\omega_k - \omega_a), \quad (73)$$

and substituting $g_{\mathbf{k},\lambda}$ from equation 70 and evaluating in spherical coordinates, it becomes,

$$\begin{aligned}
\Gamma_p &= 2\pi \sum_\lambda \int \mathrm{d}^3\mathbf{k} \frac{d^2\omega_k}{(2\pi)^3 2\hbar\varepsilon_0} \left|u_{\mathbf{k},\lambda}(\mathbf{r}_a)\right|^2 \left|\mathbf{e}_d \cdot \boldsymbol{\epsilon}_{\mathbf{k},\lambda}\right|^2 \delta(\omega_k - \omega_a) \\
&= \frac{d^2}{2(2\pi)^2\hbar\varepsilon_0}\left(\frac{\omega_a}{c}\right)^3 \sum_\lambda \int \mathrm{d}\Omega \left|u_{\mathbf{k}_a,\lambda}(\mathbf{r}_a)\right|^2 \left|\mathbf{e}_d \cdot \boldsymbol{\epsilon}_{\mathbf{k}_a,\lambda}\right|^2 \\
&= \frac{1}{8\pi^2}\left(\frac{\omega_a}{c}\right)^3 \frac{d^2}{\hbar\varepsilon_0}\Lambda \\
&= \frac{1}{3\pi}\left(\frac{\omega_a}{c}\right)^3 \frac{d^2}{\hbar\varepsilon_0}\frac{3}{8\pi}\Lambda, \quad (74)
\end{aligned}$$

where the Dirac-delta function picks out $\mathbf{k}_a$ and the integration of $\mathrm{d}\Omega$ is done over the solid angle covered by the pulse mode. For the special case where the pulse mode matches the dipole mode completely, the integral term, Λ, reaches the maximum value of $\frac{8\pi}{3}$ and the spontaneous emission into free space is made up entirely of the spontaneous emission into the pulse mode, given by the well-known formula,

$$\Gamma = \Gamma_p = \frac{1}{3\pi}\left(\frac{\omega_a}{c}\right)^3 \frac{d^2}{\hbar\varepsilon_0}. \quad (75)$$

The parameter $\Lambda \in [0, 8\pi/3]$ weighs the solid angle covered by the pulse with respect to the atom and is related to the scattering ratio, R_{sc}, since it is only determined by the geometry of the system. However, Λ alone is not a good measure of interaction strength of the light pulse with the atom since in this short pulse regime, not only the spatial overlap is important, but also the temporal profile/bandwidth of the pulse and that is not reflected in the parameter Λ.

Thus a value that we can use to quantify the interaction strength is the excitation probability, P_e. This probability is given by the expectation value of the atomic operator $\hat{\sigma}_z$ [47, 3, 35],

$$P_e(t) = \frac{1}{2}\left(\langle\Psi_0|\,\hat{\sigma}_z(t)\,|\Psi_0\rangle + 1\right), \tag{76}$$

where $|\Psi_0\rangle = |g\rangle\left|\Phi_p\right\rangle|\text{vac}\rangle$ is the initial state of the system which is a product state of the atom in the ground state, the state of the pulse used and the environment in the vacuum state. Hence to calculate P_e at any time, it is sufficient to evaluate the expectation value of $\hat{\sigma}_z$ at the interested time with the pulse used.

2.5.3 *Fock state and coherent state*

The single-photon wave-packet in the pulse mode can be written as [37]

$$\left|1_p\right\rangle = \sum_\lambda \int \mathrm{d}^3\mathbf{k}\, g^*_{\mathbf{k},\lambda}(\mathbf{r}_a) f(\omega_k)\hat{a}^\dagger_{\mathbf{k},\lambda}|0\rangle \equiv \hat{A}^\dagger|0\rangle, \tag{77}$$

where $f(\omega_k)$ is the spectral distribution function in which the temporal shape of the pulse enters into the dynamics of equation 76, and with a normalisation that will give,

$$\sum_\lambda \int \mathrm{d}^3\mathbf{k}\left|g_{\mathbf{k},\lambda}(\mathbf{r}_a)\right|^2\left|f(\omega_k)\right|^2 = 1. \tag{78}$$

The shape of the pulse is related to $f(\omega_k)$, up to a constant factor, by a Fourier transformation,

$$\mathcal{E}(t) = \frac{\sqrt{\Gamma_p}}{2\pi}\int \mathrm{d}\omega_k\, f(\omega_k) e^{-i(\omega_k-\omega_a)t}, \tag{79}$$

which then can be used to determine the coupling strength $g_{\mathbf{k},\lambda}(t)$. Using the Wigner-Weisskopf approximation, it is assumed that the coupling is constant at the frequencies of interest around the atomic transition frequency ω_a and reduces to an effective coupling strength of

$$g(t) = \sqrt{\Gamma_p}\mathcal{E}(t), \tag{80}$$

which can then be used to calculate the excitation probability for different pulse shapes from the set of coupled differential equations 71 and 72 with initial conditions $|\Psi_0\rangle = |g\rangle\left|1_p\right\rangle|\text{vac}\rangle$. However, in the ex-

periment, a coherent source from a laser is used. The coherent state wave-packet can be defined as

$$\left|\alpha_p\right\rangle = \exp\left(\alpha\hat{A}^\dagger - \alpha^*\hat{A}\right)|0\rangle, \tag{81}$$

where the $\hat{A}^\dagger$ is the wave-packet operator defined earlier in equation 77. The mean photon number N in the state can be calculated by finding the expectation value of the number operator,

$$N = \left\langle\alpha_p\right|\hat{A}^\dagger\hat{A}\left|\alpha_p\right\rangle = |\alpha|^2. \tag{82}$$

The evolution of the atomic operator $\hat{\sigma}_z$, and hence its expectation value and the excitation probability can then be calculated with the initial condition $|\Psi_0\rangle = |g\rangle\left|\alpha_p\right\rangle|\text{vac}\rangle$ instead. This section assumes that the pulse is Fourier limited and is a pure state in the photon mode. And although the laser that will be used in the experiment is generally written as a mixed coherent state, if the off-diagonal elements are zero or very small, the expectation value of the atomic operator can still be calculated by taking a trace of the density matrix operator. This mixed state with minimal off-diagonal elements can be assumed if the initial CW source has a very small (Fourier-limited) frequency(phase) and amplitude noise. For the pulse parameters and the focusing strength that correspond to the experimental conditions, the theoretical calculations were done by Wang Yimin on Matlab.

3

EXPERIMENTS WITH LIGHT WITH A 2-LEVEL SYSTEM

In this chapter we present the series of experiments that were done to quantify the interaction strength of light with a single atom. In chronological order, the following experiments were performed,

1. Measurement of a 1° phase shift on a weak coherent beam [2].
2. Measurement of a 0.16% reflection of a weak coherent beam [1].
3. Excitation with a single atom with temporally shaped pulses.

The common features of all experiments will be described first followed by setups unique to each particular experiment.

3.1 FUNDAMENTALS

At the heart of all these experiments is the atom that we use as our 2-level system and the light source that is used to 'talk' to the atom. The atom needs to be isolated and localised in space at where the light is focused to the atom. In order to achieve this, the atom together with the confocal focusing lens pair are held inside a Ultra High Vacuum(UHV) chamber. The single-atom is localised using a far-off resonant optical dipole trap loaded from a cloud of cold atomic molasses.

Once a single-atom is identified to be present in the dipole trap, the atom is further prepared such that it resembles a 2-level system. Only then does the science experiments begin proper. In the following subsections, the technical details of the core setup will be explained.

3.1.1 *Rubidium Atom as a 2-level system*

The atom chosen as the workhorse for these experiments is the Rubidium 87 atom. ^{87}Rb is a naturally occurring isotope of Rubidium with atomic number 37. It has a natural abundance of 28% and a mass of 86.9 amu [48]. With a nuclear spin, I, of $3/2$, a natural choice for the quantum numbers for its electronic eigenstates are

$$|n, l, F, m_F\rangle,$$

where n, is the principal quantum number, l, is the orbital angular momentum quantum number, F, is the total angular momentum mag-

nitude from the coupling of the total electron angular momentum, $\mathbf{J} = \mathbf{L} + \mathbf{S}$, with the total nuclear angular momentum, $\mathbf{I}$, and finally, m_F, is the magnetic quantum number. $\mathbf{L}$ and $\mathbf{S}$ are the electronic orbital and spin angular momentum respectively. A more often used notation would be the spectroscopic notation such as,

$$5\mathrm{P}_{3/2}|F = 3, m_F = 2\rangle,$$

which refers to a state with $n = 5$, $l = 1$, $j = 3/2$ and F, m_F as stated.

A strictly 2-level system is one where the atomic population can only cycle between these two levels and sum up to unity. For a dipole allowed transition, and states $|g\pm\rangle = 5\mathrm{S}_{1/2}|F = 2, m_F = \pm 2\rangle$ and $|e\pm\rangle = 5\mathrm{P}_{3/2}|F = 3, m_F = \pm 3\rangle$ of ^{87}Rb, $|g\pm\rangle \leftrightarrow |e\pm\rangle$ is a good approximation of a closed cycling 2-level system.

RELEVANT LEVEL STRUCTURE Besides the $5\mathrm{S}_{1/2} \rightarrow 5\mathrm{P}_{3/2}$ transition, also known as the D2 line (780 nm), there's the D1 line (795 nm) where the outer electron goes from $5\mathrm{S}_{1/2} \rightarrow 5\mathrm{P}_{1/2}$. Rubidium has another naturally occurring isotope with nucleon number 85. This ^{85}Rb isotope can provide us with a close-by suitable energy reference for locking our lasers. The full level structure of the relevant Rubidium levels can be found in Appendix A.

VACUUM SYSTEM In order to localize a single-atom nicely, the background pressure needs to be kept very low such that the probability that a highly energetic background gas will hit the atom is very small. The chamber is made from an anti-reflection coated (outer-side) glass Cuvette, 3×3×7 cm outer dimensions, with a wall thickness of 2.5 mm, (Hellma OG glass) bonded to a vacuum chamber using an Indium wire and sealed with a low vapor-pressure epoxy (Torr Seal resin sealant, Variance, Inc.). The vacuum chamber is continuously pumped with an 24 l/s ion getter pump. A titanium sublimation pump is also attached to the chamber and after the initial titanium sputtering, a pressure of $\simeq 1 \times 10^{-12}$ Torr was measured on a hot-cathode ionization gauge tube with the Rubidium dispenser turned off. Rubidium gas is evaporated into the chamber from an SAES Getters' Alkali Metal Dispenser when heated above 200 °C by passing a current through it.

3.1.2 *On-resonant coherent light sources*

In order to manipulate the internal electronic states of the atom, a tunable source of coherent narrow-band, compared to the atomic transition, is desirable. This is easily attainable with increasing improvements in the engineering of solid-state diode lasers almost spanning

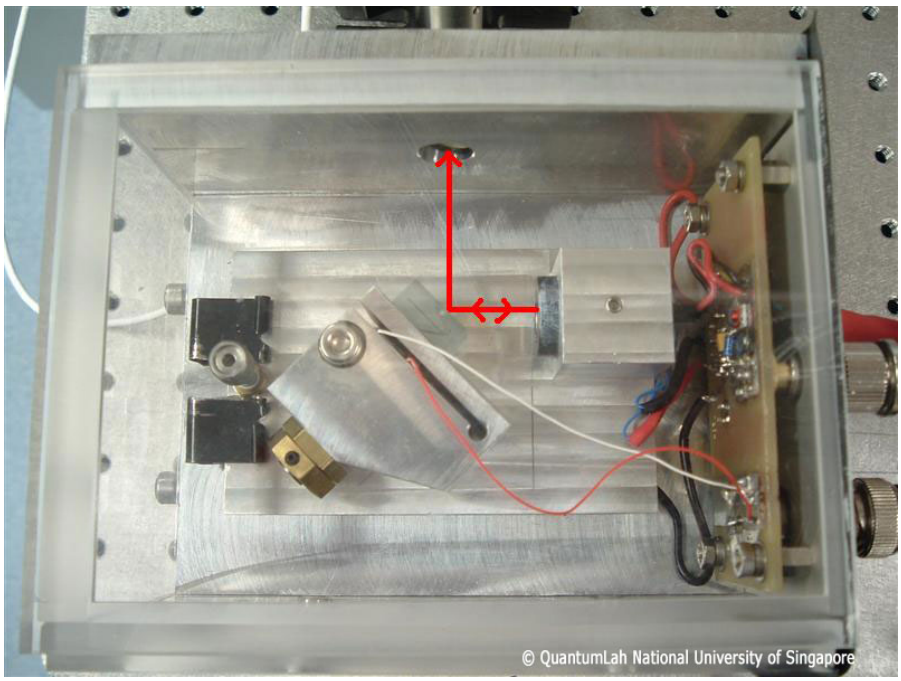

Figure 4: A photo of the top view of a typical External Cavity Diode Laser used in the experiment. The first order diffraction from the reflective diffraction grating is fed back into the diode laser.

the whole optical spectrum. The two lowest energy optical transitions in Rubidium are the D1 and D2 lines which have wavelengths very close to the lasers used in compact discs readers and thus are extensively engineered and have become very reliable and cheap for use in optics experiments [49, 50].

In our experiments, we use wavelength selected 780 nm diode lasers with a rated output power of 80 mW from Sanyo (DL7140-201SW) for beams at the D2 transitions and normal wavelength-unselected ones for beams at the D1 transition. The lasers are temperature tuned to get to the desired wavelength. A 980 nm diode with a maximum power of 300 mW was chosen as the source for the dipole trap for reasons that will be discussed in section 3.1.3.

FREQUENCY STABILITY AND EXTERNAL CAVITY DIODE LASERS The beams used in the experiments are obtained from temperature stabilised solid-state laser diodes. And depending on the tunability and linewidth required, they are further grating-stabilised in an extended-cavity Littrow configuration [51, 52] (see fig. 4). A short-term laser linewidth of $\simeq 600$ kHz with a long-term stability of 1 MHz was measured when the frequency of the grating-stabilised lasers is locked to a frequency reference. A frequency modulation technique, which will

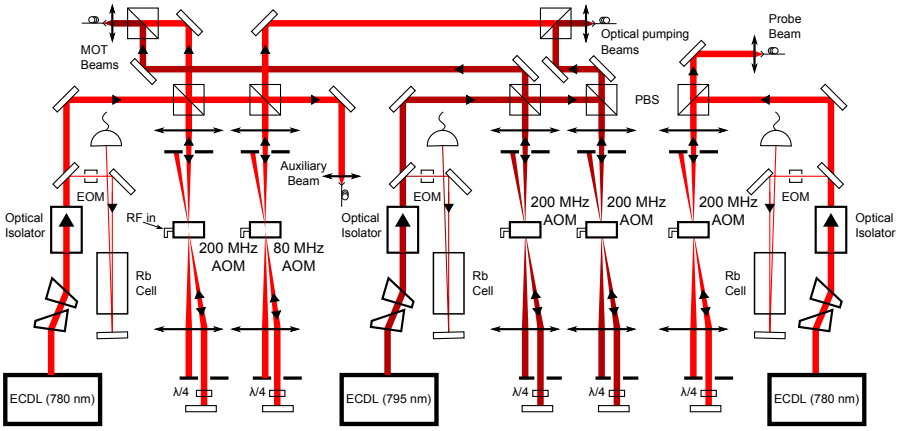

Figure 5: Schematic of the laser setup used in the experiment. Polarisation of the beams are controlled by wave-plates (not shown). The beams are all coupled to optical fibres that go to vacuum chamber. The auxiliary beam is used for alignment and frequency reference. Details are mentioned in text.

be discussed later, is used. Since the relevant transition in Rubidium that we are interested in (D2) has an atomic linewidth of 6 MHz, the linewidth of the laser is narrow enough to probe the transition coherently in continuous wave (CW) experiments. The ellipticity of the beam is compensated by anamorphic prisms and an optical isolator with 30–60 dB isolation is used to prevent optical feedback into the laser diode.

FREQUENCY LOCKING AND TUNING The frequency of the lasers are locked using Doppler-free saturated-absorption frequency-modulation (FM) spectroscopy [53, 54] to either real or cross-over transitions of Rubidium in an atomic vapour cell. Frequency modulation of the beam is done via an EOM in a tank circuit with a 20 MHz resonance. Tuning of the final laser frequency is done via Acousto-Optic Modulators (AOM) in a double-pass configuration using a polarising beam-splitter (PBS) and quarter-wave plate ($\lambda/4$). The AOM also acts as switches for turning off the beams with an extinction of about 40 dB (see fig. 5).

The cooling beams for the Magneto-Optical Trap (MOT) are derived from a laser locked to $F = 2 \rightarrow F' = 1$ on the D2 line and frequency shifted upward by 396 MHz through a double pass 200 MHz bandwidth AOM such that they are 24 MHz red-detuned from the closed cycling transition. The repumper for the MOT is derived from a laser on the D1 line, locked to $F = 1 \rightarrow F' =$ CO12, where CO12 is the

cross-over transition[1] between $F = 1$ and $F' = 2$, and also frequency shifted upward by 408 MHz through another double pass 200 MHz bandwidth AOM such that the repumper is on resonance to the $F = 1 \rightarrow F' = 2$ transition on the D1 line (see figures. 37 and 38 in appendix A).

Other than the repumper and the cooling beams for the MOT, other beams include optical pumping beam ($F = 2 \rightarrow F' = 2$ on the D2 line), probe ($F = 2 \rightarrow F' = 3$ on the D2 line) and repumper in the probe ($F = 1 \rightarrow F' = 2$ on the D1 line) with the atomic transitions frequency shifted due to the AC stark shifts of the dipole trap and bias magnetic field.

GAUSSIAN BEAMS FROM A SINGLE MODE OPTICAL FIBRE All beams are coupled into single mode optical fibres which not only serve as an easy way to guide the beams to the atom in the vacuum chamber, but also cleans up the spatial mode of the beam to that of the fundamental Gaussian mode supported by the fibre. Polarisation-maintaining fibres are also used if the polarisation of the beam needs to be kept constant.

3.1.3 *Laser Cooling and Trapping of Rubidium*

Loading and trapping of a single atom is a probabilistic process. To load a single atom into our dipole trap, we need a large enough density of pre-cooled atoms, formed by the MOT, around the trap such that the probability of loading per unit time or loading rate is reasonable. Once loaded, the lifetime of the atom in the trap is determined by the loss rate due to either the loading of another atom into the trap or collisions with highly energetic background atoms.

It should be noted that the dipole trap is a conservative potential and can only trap atoms which have a lower kinetic energy than the trap depth of the potential. Thus to trap the atom, there needs to be a process that takes away kinetic energy while the atom is in the trap, which is done by the cooling beams of the MOT.

MOT The Magneto-Optical Trap is formed at the intersection of 6 cooling beams and a magnetic quadrupole field gradient with zero field at the point of intersection. The red-detuned cooling beams are used to Doppler cool the Rubidium atoms, by preferentially scattering the faster moving atoms [55]. Without a quadrupole field, the cooling beams will set up an optical molasses of slow moving but not really trapped atoms. In order to trap, a trapping potential is

1 The cross-over transition of $F = 1$ and $F = 2$ is not a real transition but an artefact of the saturated absorption technique using counter-propagating beams [38].

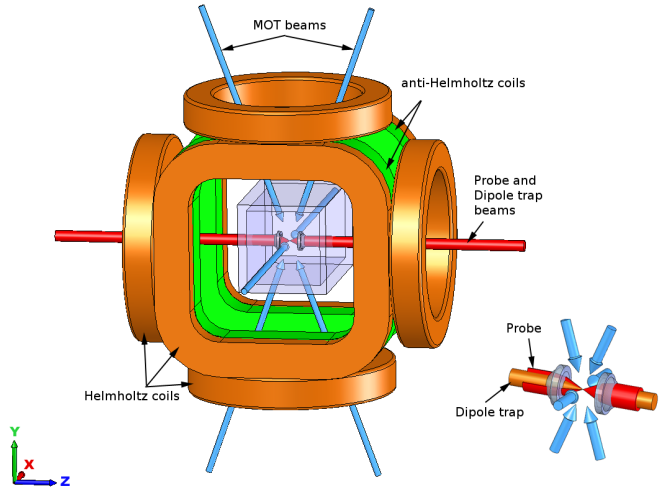

Figure 6: The core of the setup including a magneto-optical trap, a cuvette attached to a vacuum chamber, the aspheric lenses, and the relevant light beams used for trapping the atom and performing the experiment (the lens holder in the cuvette is not shown for clarity). The inset is a zoom-in near the centre of the lens system.

formed by exploiting the Zeeman shifts caused by a magnetic field minima [55, 56, 38]. The quadrupole field is set up by a pair of coils in an anti-Helmholtz configuration which generates a field gradient of $\simeq 7\,\text{Gauss}\,\text{cm}^{-1}$ along the X-axis and $\simeq 3.5\,\text{Gauss}\,\text{cm}^{-1}$ along the Y- and Z-axes at the centre of the trap.

The MOT cooling beam is split into 3 and goes through single mode fibres before being rotated to circular polarisation by a quarter wave plate. One beam goes through the cuvette along the X-axis while the other two pass through at an angle of 20° from the vertical Y-axis in the Y-Z plane (see figure 6). All beams are then retro-reflected on mirrors to create the other 3 beams. Due to reflection losses from the glass cuvette, the power from the reflected beams is slightly lower. The cooling beams from the single mode fibres thus are slightly focused such that the retro-reflected beams have a smaller waist and thus the same intensity as the forward beam at the centre of the trap. The beams have a waist of 0.7 mm to 0.6 mm at the centre of the trap. The intensity of each beam is $\simeq 20\,\text{mW}\,\text{cm}^{-2}$ which is about $5.5 \times I_{\text{sat}}$, where $I_{\text{sat}} = 3.6\,\text{mW}\,\text{cm}^{-2}$ is the saturation intensity for the D2 transition of ^{87}Rb for isotropic light [48].

The repumper, on the D1 line, is delivered to the vacuum chamber using the same single mode fibres as the cooling beams. The purpose of the repumper is to keep the $5S_{1/2}|F = 1\rangle$ ground state unpopulated, such that the atoms are continuously cooled in the cycling transition.

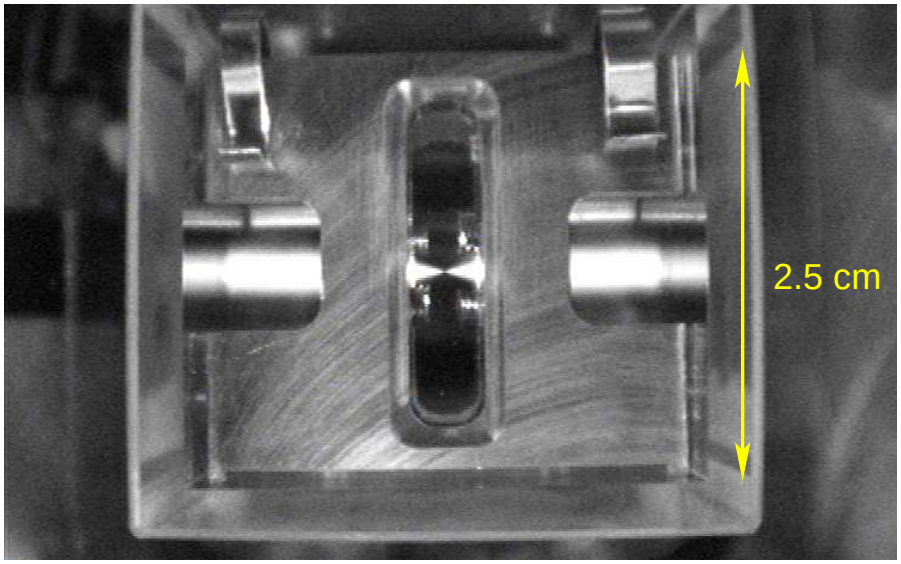

Figure 7: A photo of the probe beam fluorescence from the atoms when a high dispenser current is set. There are much less atoms in the chamber during the normal operational condition of the experiment.

The total intensity of the repumper at the MOT is $\simeq 40\,\mathrm{mW\,cm^{-2}}$. With such a setup, we obtain a ^{87}Rb-atom cloud with an approximate diameter of 0.4 mm.

CONFOCAL LENS PAIR An important component of the experiment is the confocal aspheric lens pair inside the cuvette in the vacuum chamber. An aspheric lens is designed to give a diffraction limited focus, without spherical aberration, from a collimated beam thus replacing the need for multi-element microscope objectives. The aspheric lenses used in the setup were manufactured by LightPath Technologies, Inc. (350230-B). These moulded glass aspheric lenses have a effective focal length (at 780 nm) of 4.5 mm and working distance (back focal length) of 2.91 mm both with an uncertainty of ±1% of the effective focal length. The lenses have a clear aperture of 4.95 mm, are antireflection coated for near-infrared wavelengths and are UHV compatible.

To arrange them confocally, a lens holder was machined such that the lenses are both concentric and the distance between them is 5.82 mm with a machining uncertainty of 0.02 mm. Any slight non-confocality can be compensated by sending a beam that is slightly focusing or diverging instead of a collimated beam. The lens holder is machined from aluminium and the lenses held in place with titanium screws.

OPTICAL DIPOLE TRAP An optical dipole trap is created by focusing a light beam tightly such that an a large intensity gradient is created. This intensity gradient will set up a potential due to the optical dipole force depending on the intensity and wavelength of the beam and also the atomic transitions of the atom [38]. For the experiment, we have chosen 980 nm as the trap wavelength as it is very far detuned (~200 nm) from any ground state atomic transition of ^{87}Rb and also because relatively high powered single mode diode lasers (300 mW) at this wavelength are readily available.

The depth of the potential is proportional to I/δ, where I is the intensity of the dipole beam at the trap and δ is its detuning from the D1 line of ^{87}Rb. The scattering rate of the beam by the atom on the other hand is proportional to I/δ^2. For the experiment, the dipole trap beam was obtained from a temperature stabilised diode laser without an external cavity. It passes through an AOM which is used as an amplitude modulator to stabilise the power of the beam at the trap. The polarisation of the dipole beam is chosen to be right-hand circular. A dipole trap beam power of $\simeq 20$ mW and a focal waist[2], w_D, of $\simeq 1.8\,\mu$m gives a trap potential depth, U_0, of $h \cdot 23$ MHz or $k_B \cdot 1.1$ mK. With such an intensity, we estimate the off-resonant scattering rate of the dipole trap beam to be on the order of $10\,\mathrm{s}^{-1}$.

Using paraxial approximation, the spatial distribution of the dipole potential can be described, in cylindrical coordinates by,

$$U(\rho,z) = \frac{-U_0}{(1+(z/z_R)^2)} \exp\left[-\frac{2\rho^2}{w_D^2(1+(z/z_R)^2)}\right], \tag{83}$$

where,

$$z_R = \pi w_D^2/\lambda \tag{84}$$

is the Rayleigh range of the Gaussian beam. For a sufficiently cold atom in the trap, $|E_{\mathrm{Total}}| \ll U_0$, the potential can be Taylor expanded about the minima giving rise to a harmonic potential in the form of,

$$U(\rho,z) \approx -U_0\left[1-2\left(\frac{\rho}{w_D}\right)^2-\left(\frac{z}{z_R}\right)^2\right]. \tag{85}$$

The oscillation frequencies of a trapped atom in the harmonic potential, in the radial and longitudinal directions respectively, are given by

$$\omega_\rho = \sqrt{\frac{4U_0}{mw_D^2}}, \qquad \omega_z = \sqrt{\frac{2U_0}{mz_R^2}}, \tag{86}$$

2 The focal waist was estimated using paraxial approximation.

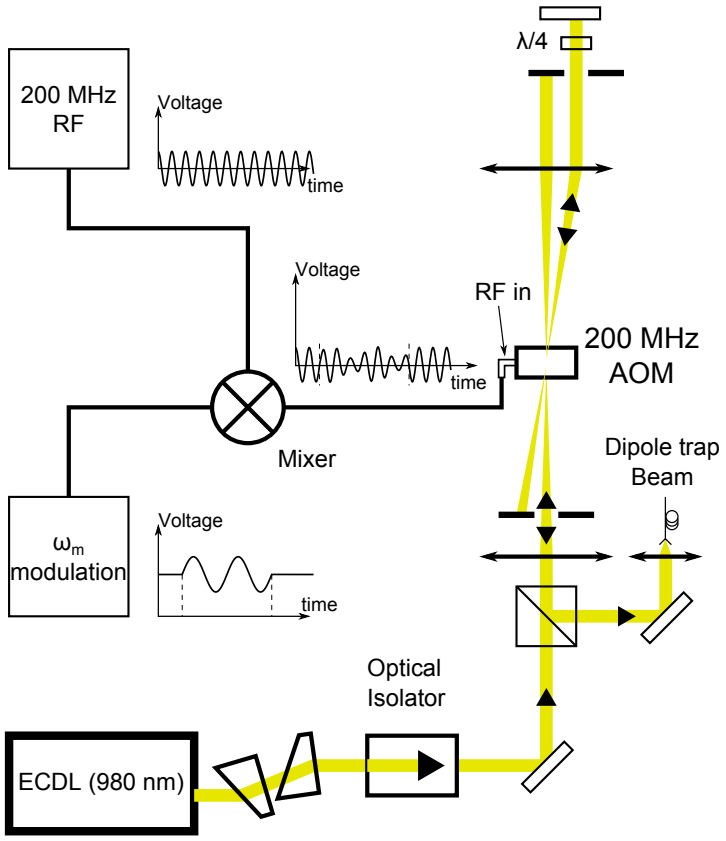

Figure 8: Setup to determine the trap frequency of the dipole trap. The power of the dipole trap beam is modulated at ω_m by modulating the amplitude of the 200 MHz RF that is sent to the AOM. The modulation is switched on for a variable duration only when the atom is in the trap and its lifetime measured.

where m is the mass of the ^{87}Rb atom. Within the paraxial approximation and from equations (84) and (86), the two trap frequencies have a fixed ratio, which depends on w_D and the trap wavelength, λ,

$$\frac{\omega_\rho}{\omega_z} = \frac{\sqrt{2}\pi w_D}{\lambda}. \tag{87}$$

The trap depth can similarly be written as parameters of the trap frequencies, trap wavelength and atomic mass as,

$$U_0 = \frac{m\lambda^2}{8\pi^2}\frac{\omega_\rho^4}{\omega_z^2}. \tag{88}$$

The trap frequencies are measured by modulating the dipole trap power. The setup for this measurement is shown in figure 8. The amplitude of the 200 MHz RF that is sent to the AOM is modulated

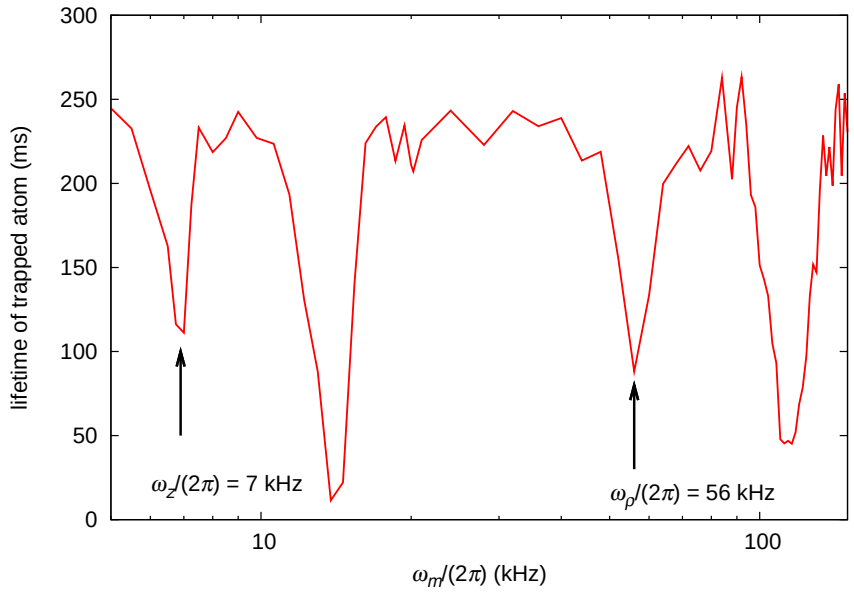

Figure 9: A semi-log plot of the lifetime of the trapped atom versus modulation frequency of the dipole trap power reveals dips at the resonances of the trap. For both trap frequencies, only the $n = 1, 2$ resonances are clearly seen.

at ω_m, with a modulation depth 20–60% and ω_m scanned. After the atom loads into the trap, the modulation is switched on for a variable amount of time and the probability that the atom remains in the trap is measured. Lifetime of the atom in the trap for each modulation frequency is extracted by fitting the probability versus time measurement to an exponential decay with the time constant as the parameter. Parametric resonance occurs when the modulation frequency is [57]

$$\omega_m = \frac{2\omega}{n}, \quad n = 1, 2, 3\ldots, \tag{89}$$

where ω can either be the longitudinal or transverse trap frequency. On resonance, the trap lifetime is dramatically reduced and this can be as can be seen from figure 9. The measured frequencies are $\omega_z \approx 2\pi \cdot 7\,\text{kHz}$ and $\omega_\rho \approx 2\pi \cdot 57\,\text{kHz}$. These numbers are compatible with the estimated trap parameters of the dipole trap.

OVERLAPPING OF THE FOCI OF THE DIPOLE TRAP AND PROBE BEAMS AND THE COLLECTION OPTICS The probe beam (780 nm) (together with the optical pumping and repumper in the probe beam) passes through the same set of aspheric lenses as the dipole trap beam (980 nm). Due to chromatic aberration of the lens, for a collimated beam, differ-

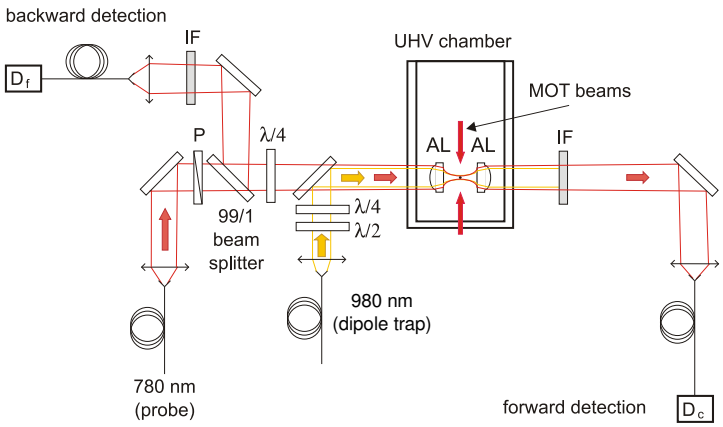

Figure 10: A basic setup to load and trap a single atom. Inside the ultra-high vacuum (UHV) chamber, the atom is loaded into the dipole trap, formed at the focus of the 2 aspheric lenses (AL), from the cloud of cold atoms at the Magneto-Optical trap (MOT). Interference filters (IF) at 780 nm filter out all dipole trap beam at 980 nm. The forward and backward detection detector, D_c and D_f are single photon silicon avalanche photodiodes which counts the fluorescence of the atom under the MOT beams. A probe beam at 780 nm is sent to the atom through the aspheric lenses as well. Its polarisation is controlled via polariser (P) and a quarter waveplate. 60% of the probe beam that passes through the cuvette is collected into the forward detection fibre.

ent wavelengths will have a different focal spot. To ensure that at least the probe and dipole trap beam have the same foci, their divergences are adjusted such that each individual beam have the same waist equidistant from the focus. This means that the beams are symmetric from the centre of the lenses and hence have foci that overlap longitudinally to an estimated uncertainty of $\approx 1.3\,\mu m$ limited by our collimating and beam waist measurement device[3]. For the transverse overlap, the axis of the two beams are aligned to an uncertainty better than $15\,\mu m$ at a plane about 10 cm away from the cuvette and better than 0.15 mm at a plane about 7 m away on the other side of the cuvette using a CCD. Doing this, we estimate that the transverse overlap of the foci to be better than 90 nm.

Collection optics are placed on both sides of the chamber to collect 780 nm light scattered through the aspheric lens pair (figure 10). All other wavelengths are filtered out using dichroic and interference filters centred at 780 nm (Semrock LL01-780-12.5). Additionally, the collection optics in the forward direction also collects about 60% of

3 The power of the beam is measured on a detector as a knife-edge on a motorised stage is moved across it. The recorded power as a function of the blade translation follows the error function (for a Gaussian beam) with the beam waist as a parameter.

the probe that passes through the chamber. The losses[4] in the probe are due to reflection losses off the cuvette and the aspheric lenses (87%), transmission losses through dichroic and interference filters (91%) and finally mode-matching and reflection losses when coupling into another uncoated single mode fibre (75%).

The single mode fibres are connected directly to Silicon avalanche photodiodes (Si-APD) operating in Geiger counting mode. Two kinds of Si-APD are used, one passively quenched and the other actively quenched. The passively quenched APD is home-made and saturates at about 300 kHz counts while the actively quenched APD is a module from Perkin Elmer (SPCM-AQR 15) with a peak count rate of 25 MHz. Dead time of the detectors are approximately the inverse of the maximum count rates. Both APDs have a quantum efficiency of about 50–60% at 780 nm.

3.1.4 *Trapping of a single atom*

In order to trap a single atom, we exploit the collisional blockade mechanism [58, 59] present in a tightly focused optical dipole trap. This blockade mechanism comes about from light-assisted inelastic collisions of two atoms in a very small dipole trap leading to a loss of both atoms [60, 61]. In other words, this ensures that we will never have more than one atom in the trap at any time.

A typical way of determining the number of atoms in a trap is to observe the amount of atomic fluorescence from the trap. If the number of atoms in the trap, N, is small, the amount of detected fluorescence shows a discrete behaviour proportional to N. Such discrete-step signals have been observed for example in a MOT [62, 60], and also in moderately focused dipole trap [63]. For a dipole trap with a tighter focus, the fluorescence signal has only two discrete levels corresponding to either one or no atom in the trap [58, 64]. Such a signal is measured and shown in figure 11.

A binary on/off signal however is not a sufficient proof that there's only a single atom in the trap. A more definitive method is to measure the normalised second-order correlation function of the light scattered from the trap [36, 37], defined classically as,

$$g^{(2)}(\tau) = \frac{\langle I_1(t) I_2(t+\tau)\rangle}{\langle I_1(t)\rangle \langle I_2(t)\rangle}, \tag{90}$$

where the angle brackets denotes a time average over t and $I_n(t)$ is the fluorescence intensity at positions 1 and 2. At long time delays, $\tau \to \infty$,

4 The numbers quoted are the transmission through those elements

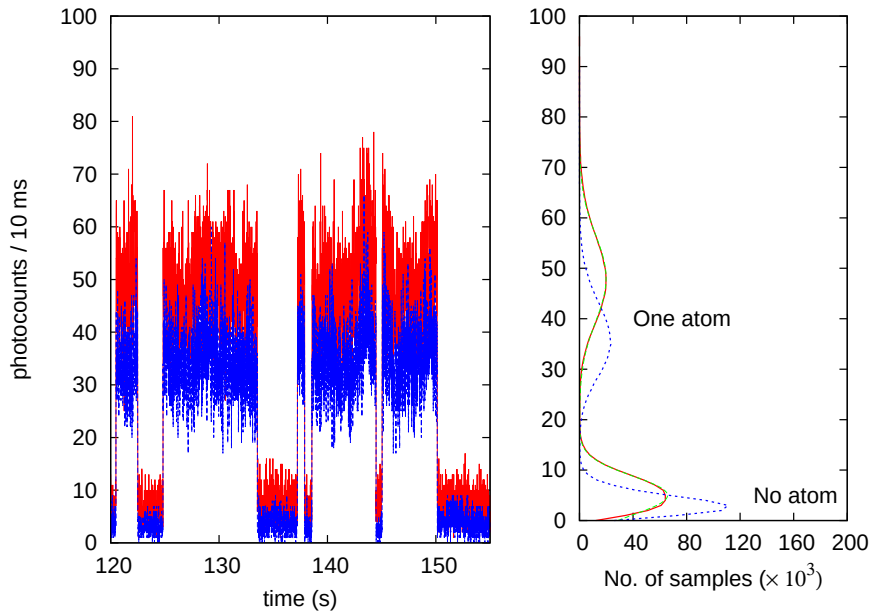

Figure 11: (Left) Typical fluorescence signals from the atom in dipole trap, measured from two different detectors. The different count rates for the 'one atom' level is due to difference in dead time of the two detectors. (Right) Histogram of the signal levels of the photocounts for 10^4 s. The green trace is a compound Poissonian fit to the histogram. It can be clearly seen that there is a gap in the photocounts between zero and one atom and also the absence of any higher photocounts due to two atom events.

all correlations should vanish and $g^{(2)} \to 1$. At shorter time scales of τ, the $g^{(2)}(\tau)$ is dependent on the source and hence properties of the fluorescence intensity. For any classical light field, $g^{(2)}(\tau)$ obeys the inequalities [65],

$$g^{(2)}(0) \geq 1, \qquad g^{(2)}(\tau) \leq g^{(2)}(0). \tag{91}$$

This definition is convenient when we are measuring current on a photodetector that is proportional to intensity of the light. In terms of photon counting, $g^{(2)}(\tau)$ describes the conditional probability of detecting a second photon at time τ after a first one was detected at $t = 0$ [65, 66]. For single-mode light in a quantised field however, it can be shown (equation 5.10.3 of [36]) that the range of values for the second-order correlation function becomes,

$$1 - \frac{1}{\langle n \rangle} \leq g^{(2)}(\tau) \leq \infty \quad \text{for } \langle n \rangle \geq 1 \text{and for all } \tau, \tag{92}$$

where $\langle n \rangle$ is the mean photon number. The fluorescence light from a single atom is not classical because its $g^{(2)}(0)$ violates equation 91. This is because after the emission of the first photon, the atom is in the ground state and cannot emit another photon at zero delay, i.e. $g^{(2)}_{N=1}(0) = 0$. For N atoms in the trap, the correlation function, $g^{(2)}_N(\tau)$ can be written as [62, 36],

$$g^{(2)}_N(\tau) = \frac{1}{N}\left[g^{(2)}_1(\tau) + (N-1)\left(1 + \left|g^{(1)}(\tau)\right|^2\right)\right], \tag{93}$$

where $g^{(1)}(\tau)$ is the field correlation function describing interference between light fields from different atoms. For a fluorescence collected from a large solid angle, the interference term disappears and we have $g^{(2)}_{N>1}(0) = \frac{N-1}{N} \geq 0.5$.

The detected fluorescence signal from the atom is recorded using a timestamp unit (maximum resolution of 450 ps and 120 ns dead time) and post processed to extract the second-order correlation function between two different detectors, D_c and D_f. A delay cable of 480 ns is inserted between D_c and the timestamp unit to compensate for the dead time of the timestamp unit. Figure 12 shows the normalised $g^{(2)}(\tau)$ of the recorded events (uncorrected for detector dark-counts). It shows a Rabi oscillation with frequency of ≈ 76 MHz and a clear anti-bunching dip (below 0.5) at zero delay, confirming that we have a single atom in the trap.

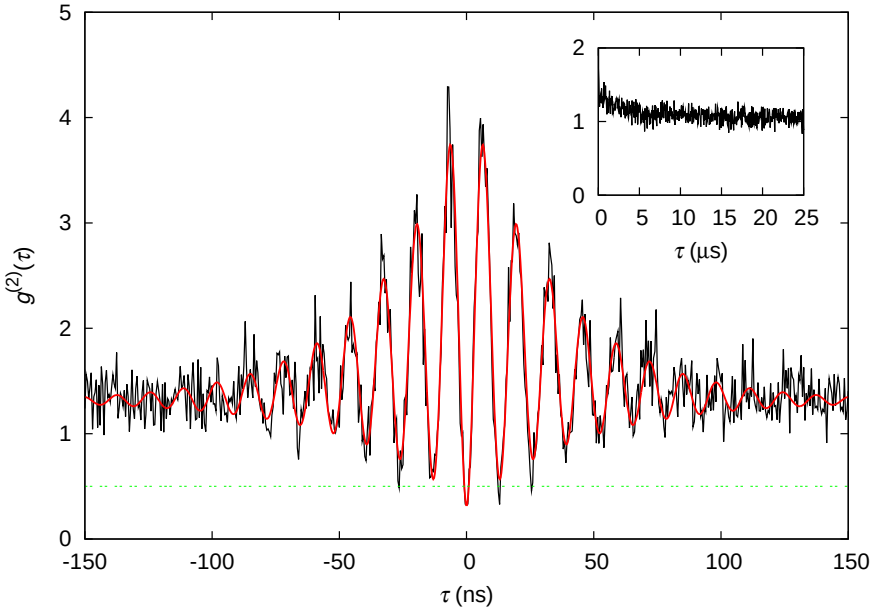

Figure 12: Normalised second-order correlation function versus time delay τ between two photodetection events at detector D_c and D_f with clear anti-bunching at $\tau = 0$. The smooth red curve is a fit using a simple sinusoidal term with a delay dependent envelope. (Inset) At long delays, $g^{(2)}(\tau)$ goes to 1.

3.2 FROM A SINGLE ATOM TO A SINGLE 2-LEVEL SYSTEM

The ^{87}Rb atom has a multi-level structure and is perturbed by any external fields. Two major sources of perturbation experienced by the trapped atom are from stray magnetic fields and the dipole trap beam. The stray magnetic fields are mostly due to the Earth's magnetic field and the permanent magnet inside the ion-getter pump. Although the magnetic field at the centre of the dipole trap can be zeroed to within an uncertainty of ±10 mGauss in the 3 directions using three pairs of Helmholtz coils (with the quadrupole coils switched off), it is very difficult to remove any magnetic field gradient. The other perturbation is caused by the light fields, mainly from the dipole trap. The dipole trap beam sets up the dipole potential which is due to the AC Stark shifts to the ground state energy levels of the atom.

3.2.1 *Quantisation axis*

Without any external fields, there is no preferred direction for the atom and its m_F levels are degenerate with the population equally distributed. The dipole trap beam breaks this symmetry by selecting a

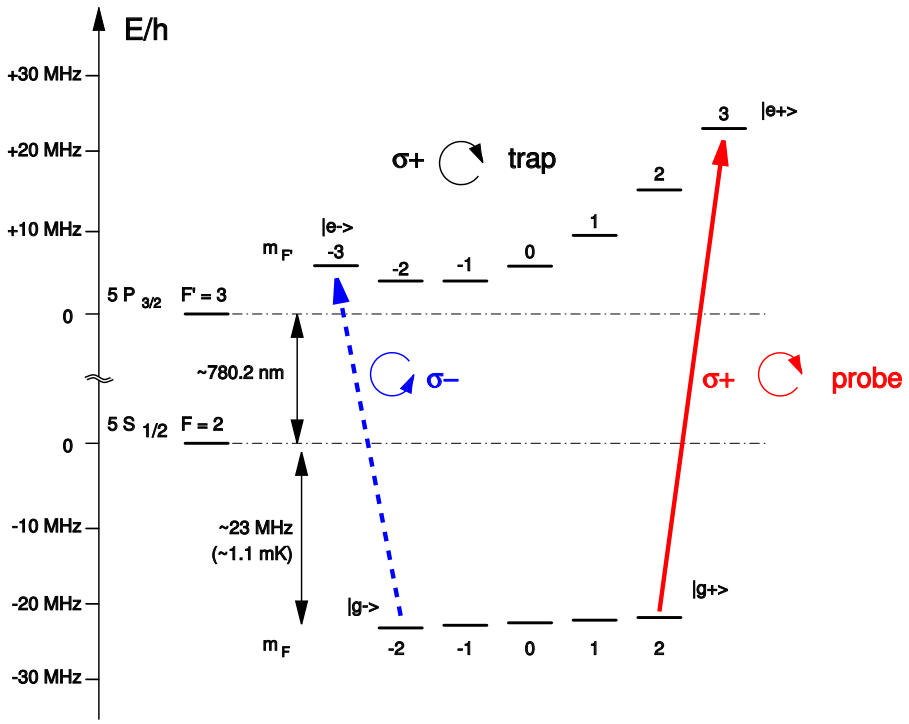

Figure 13: Calculated AC Stark shifts of a ^{87}Rb atom in a circularly polarised dipole trap for the parameters mentioned in the text.

preferred direction (z-axis) in the direction of the beam. Choosing this direction as the quantisation axis, we can calculate the AC Stark shift of the ground, $5S_{1/2}$ and excited $5P_{3/2}$ states of ^{87}Rb. The shifts were calculated using a second-order time dependent perturbation theory (see appendix of [67] using the known radiative lifetimes of transitions to the relevant states [68]. The $5S_{1/2}|F = 2\rangle$ and $5P_{3/2}|F = 3\rangle$ shifts are shown in figure 13. Under a right-hand circularly polarised dipole beam the ground states of the atom shift downwards by ≈ 23 MHz and become non-degenerate with a separation of ≈ 330 kHz between each Zeeman sub-level or m_F states. The excited states shift upwards and are strongly split. To make the ground state further non-degenerate, a bias magnetic field of ≈ 2 Gauss is introduced along the z-axis such that the levels are further split by an additional 1.4 MHz between each m_F states.

If some stray magnetic field orthogonal to the quantisation axis is present, the atom will undergo Larmor precession[5] leading to a mixing of the population into other m_F states. As a result no two-level system will exist after a characteristic time given by the inverse Larmor frequency.

5 Along the resultant magnetic field direction.

3.2.2 *Optical pumping*

In order to prepare the atom in a 2-level system, the atomic population is optically pumped to $|g\pm\rangle$. This can be done via the a circularly polarised beam that is tuned on resonance to the $F = 2 \rightarrow F' = 3$ transition on the D2 line (probe beam) and another to the $F = 1 \rightarrow F' = 2$ transition on the D1 line (repumper in the probe beam), both of which are AC Stark shifted by ≈ 30 MHz apart from their unperturbed states. Under a circularly polarised beam along the quantisation axis, the allowed transitions has to have a $\Delta m_F = m'_F - m_F = \pm 1$. Thus for an atom with F and m_F ground states initially equally populated, a left-hand circularly polarised optical pumping beam will keep on exciting the atom from $5S_{1/2}|F = 2, m_F = m_F\rangle$ to $5P_{3/2}\left|F' = 3, m'_F = m_F - 1\right\rangle$ and $5S_{1/2}|F = 1, m_F = m_F\rangle$ to $5P_{1/2}\left|F' = 2, m'_F = m_F - 1\right\rangle$. Spontaneous emission is random and can occur with $\Delta m_F = 0, \pm 1$ and with probabilities dependent on their Clebsh-Gordon coefficients. However on average, the atom will decay to $|g-\rangle$ after repeated excitation.

To achieve this efficiently, a minimum number of excitation cycles is needed. As such, we allocated 20 ms for optical pumping, by the end of which, the atom should be left cycling in the $|g-\rangle \leftrightarrow |e-\rangle$ transition with a probability of more than 99%, which is the final 2-level system that we are interested in. When a right-circularly polarised beam is used instead, the atom will end up in the $|g+\rangle \leftrightarrow |e+\rangle$ cycling transition. This bright state optical pumping technique, so called because the final cycling state is constantly scattering light, is used in the transmission, reflection and phase shift experiment of section 3.3.

3.2.2.1 *Dark state Optical pumping*

In the previous optical pumping scheme, the atom will end up in the $|g\pm\rangle \leftrightarrow |e\pm\rangle$ cycling transition at the end of the optical pumping step. Since pumping into this 2-level system is a probabilistic process, there will be instances where the atom will end up in the final cycling transition earlier and just continue to scatter more photons, thereby increasing it's average kinetic energy due to recoil. To ensure a minimal number of excitations, the atom should end up in an optically dark state where it does not have any allowed resonant transitions to excite to. This can be achieved by sending a beam that is tuned on resonance to the $F = 2 \rightarrow F' = 2$ transition on the D2 line (optical pumping beam) instead of $F = 2 \rightarrow F' = 3$ as used previously.

This works because there are no $5P_{3/2}\left|F' = 2, m'_F = \pm 3\right\rangle$ states, and when the atom reaches the state $|g\pm\rangle$ no further excitations are possible. The atom thus ends up in the optically dark state of $|g\pm\rangle$. Because the $|g\pm\rangle$ state is optically dark, there won't be any excess excita-

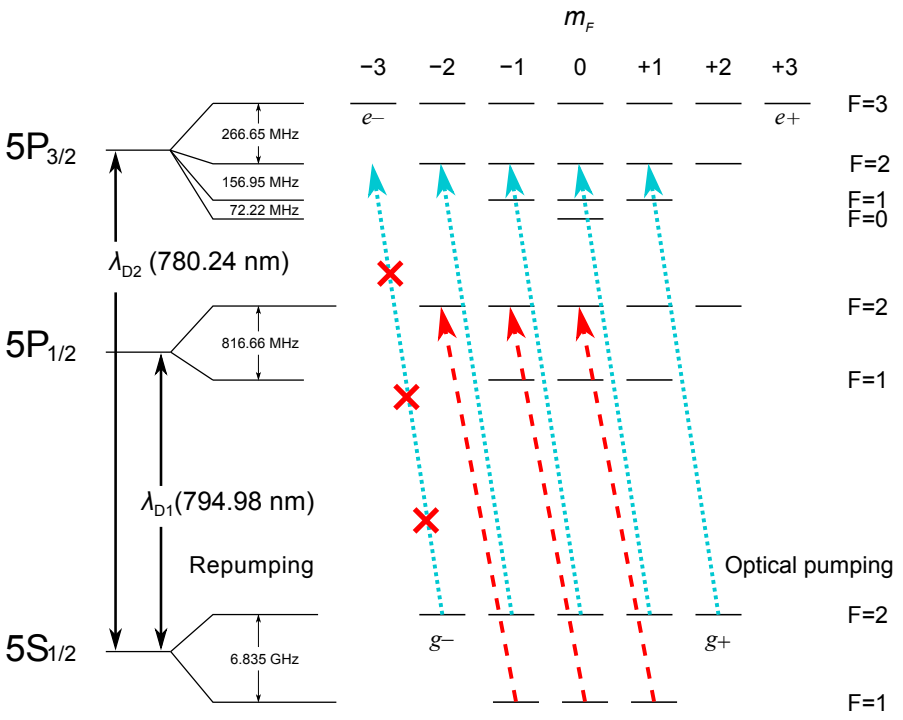

Figure 14: Dark state optical pumping scheme in ^{87}Rb pumping to $|g-\rangle$. Left-hand circularly polarised optical pumping beams along the quantisation axis drive the σ^- transitions. To pump to the $|g+\rangle$ state, the optical pumping beams polarisations are made right-hand circular.

tion which heats up the atom. Figure 14 shows the level scheme and polarisation used for optical pumping into the $|g-\rangle$ state. As such, the beam intensity can be increased and was set to be about $64\,\mathrm{mW\,m^{-2}}$, such that optical pumping is done within 10 ms. At this point, the atom is then in a good approximation of the final two level system which is between $|g\pm\rangle$ and $|e\pm\rangle$. This dark state optical pumping is used for the pulsed experiments described in section 3.4.

3.3 TRANSMISSION, REFLECTION AND PHASE SHIFT EXPERIMENTS

The first set of experiments were done with a weak coherent probe beam where the Rabi frequency is $\Omega \ll \Gamma$. In this limit, the measure of scattering ratio, R_{sc}, is still adequate to quantify the interaction strength. As discussed in section 2.3, there are several complementary experiments that can be done to determine R_{sc}. The probe beam is derived from a diode laser similar to the one used for the cooling beams in the MOT. The laser frequency is locked to the transition from $5S_{1/2}|F = 2\rangle$ to the cross-over transition $5P_{3/2}|F' = \mathrm{CO}23\rangle$. The frequency is then shifted up by about ≈ 170 MHz using a double pass 80 MHz AOM and swept across the $|g-\rangle \rightarrow |e-\rangle$ transition. The laser can also be locked to the $5S_{1/2}|F = 2\rangle$ to $5P_{3/2}|F' = 1\rangle$ transition and shifted upwards by ≈ 440 MHz by a 200 MHz AOM. See figure 38 in appendix A for the transition lines. In all of these experiments, when the probe frequency is scanned across the resonance, its intensity is adjusted such that the scattering rate for all frequencies are approximately the same at about $2500\,\mathrm{s^{-1}}$. Also, the probe beam is always kept switched on during the experiment to avoid power fluctuations due to thermal heating of the AOM. Since the probe is always on, we cannot optically pump to a dark state. Hence optical pumping is done with the probe itself for 20 ms.

3.3.1 *Transmission and reflection*

The transmission and reflection experiment can be done simultaneously. The setup for these experiments is that shown in figure 10. The probe beam has a Gaussian profile with a waist parameter of 1.25 mm just before the aspheric lens corresponding to a focusing parameter, u, of 0.278 from equation 25. Its polarisation is transformed to left-hand circular to drive the $|g-\rangle \leftrightarrow |e-\rangle$ transition. The probe beam, after passing through the atom, is recollected into another single-mode fibre and that goes to detector D_c. The collection optics for the reflected probe is aligned by first sending another beam in place of detector D_f and overlapping it with the probe and coupling

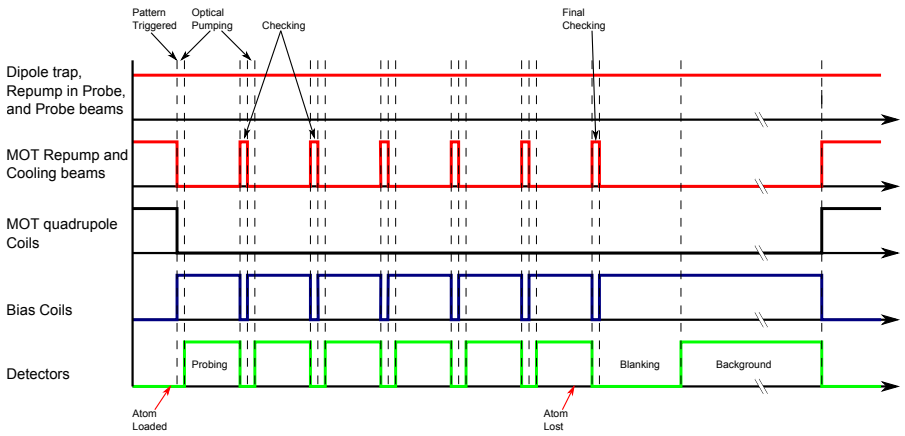

Figure 15: Schematic of the temporal sequence for the cw experiments. In this example, the probing cycle (steps 2–5) is repeated 6 times before the final background measurement. Only data from the first 5 cycles are used for calculating the transmission/reflection and phase shift. The blanking step separates atom probing and the background measurement.

them both into the same single-mode fibre (detector D_c) with similar high efficiencies of about 75%. Once that is done the two collection optics single-mode fibres have the same mode, which is the mode defined by the probe beam. Detector D_f is then replaced back.

The experiment begins by choosing a particular detuning for the probe beam. A cloud of cold Rubidium atoms is then gathered at the MOT. Once an atom is loaded into the dipole trap, its fluorescence due to the MOT beams is collected by detector D_f. This increase in count rate in the detector triggers the transmission/reflection measurement sequence. The main steps in the sequence are (see fig. 15):

1. Switching off the MOT quadrupole coils and the MOT beams.
2. Applying of a bias magnetic field of ≈ 2 Gauss along the quantisation axis which gives a Zeeman splitting of approximately 1.4 MHz.
3. 20 ms of optical pumping into the $|g-\rangle$ state which is done via the probe beam. In this time, the current supplying the bias magnetic field also should have stabilised[6].
4. After preparation, the counts rates, t_A, r_A, (normalised per 100 ms) on detectors D_c and D_f are recorded for τ_A which ranges from 130–150 ms (See Appendix C for a more detailed description).
5. Next, the MOT beams are turned on to check if the atom had remained in the trap, again by monitoring fluorescence at detector

6 See appendix B.2

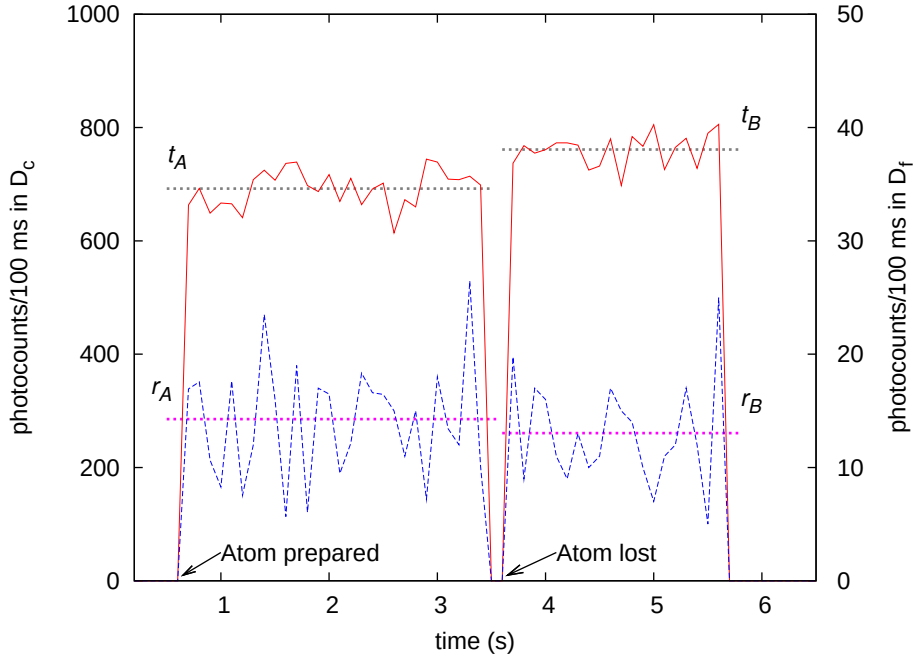

Figure 16: A typical measure of normalised count rates at detectors D_c(red, solid) and D_f(blue, dashed) during an atom loading event for the transmission/reflection experiment. The dotted horizontal lines are the averaged values for the respective detectors and steps. This trace was taken for a probe that is close to resonance and hence an obvious difference in the photocount rates.

D_f. In this step, the MOT quadrupole coils are not switched on and the bias magnetic field is switched off. This whole process takes about 20 ms. At the end of this step, the MOT beams are switched off and if the atom is still in the trap, steps number 2 through 5 repeated again.

6. Otherwise, the background count rates, t_B, r_B, (also normalised per 100 ms) on the same detectors are recorded for τ_B which lasts about 2 s as reference without the atom.

7. After measuring the background count rates, the MOT beams and MOT quadrupole coils are switched on again to load another atom into the dipole trap.

Figure 16 shows a typical trace of the photocounts recorded during a measurement sequence. The transmission, T_i, and reflection, R_i, for each loading event is calculated from the normalised count rates, $t_{A,B}$ and $r_{A,B}$ by,

$$T_i = \frac{t_A}{t_B}, \qquad R_i = \frac{r_A - r_B}{t_B} \tag{94}$$

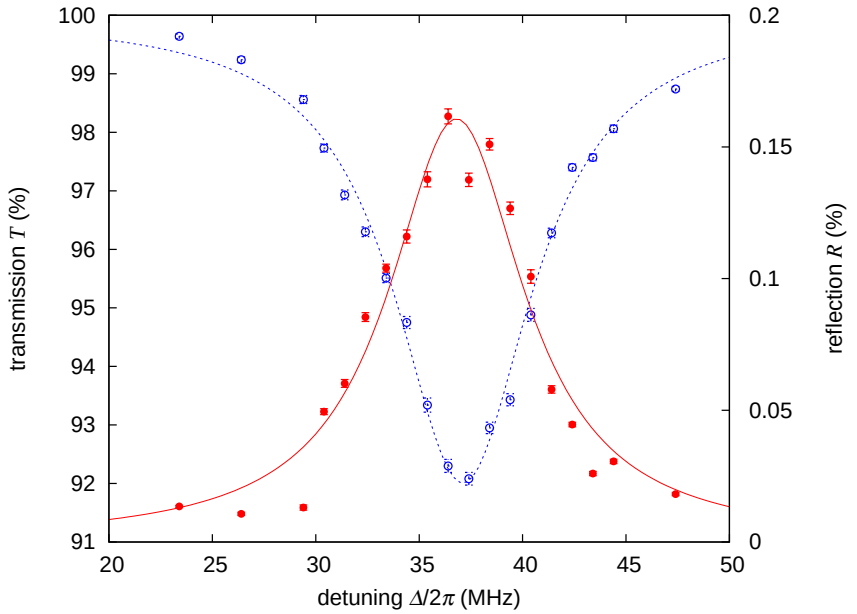

Figure 17: Results for the transmission and reflection experiment. For this focusing strength, a maximal reflection of about 0.16% of the incoming power (filled circles), coinciding with the minimal transmission of 92% (open circles) was observed. The solid lines are weighted fits to a Lorentzian profile obtained by minimising the χ^2 quantity.

and a weighing factor

$$w_i = \frac{\tau_B \sum \tau_A}{\tau_N \left(\tau_B + \sum \tau_A\right)}, \tag{95}$$

where τ_N is a normalisation time to keep the weight unit-less and the summation is carried out over the time where the atom remained in the trap. The uncertainties in the measured quantities are derived from Poissonian counting statistics. For each frequency detuning of the probe beam, we typically average over a 100 loading cycles and calculate the final transmission and reflection for that detuning as,

$$\bar{T} = \frac{\sum w_i T_i}{\sum w_i}, \qquad \bar{R} = \frac{\sum w_i R_i}{\sum w_i}. \tag{96}$$

Results

The transmission and reflection measurements, as the detuning is swept across the resonance, is shown in figure 17. Both the measurements seem to follow the expected Lorentzian line profile from equation 56 and 59. A best fit to such a profile with centre detuning Δ_0, full width

half maximum Γ, and scattering ratio R_{sc}, as free parameters was done for both dataset. For the transmission measurement, the best fit parameters were, $\Delta_0/2\pi = 37.1\pm0.1$ MHz, $\Gamma/2\pi = 8.1\pm0.3$ MHz and $R_{sc} = 0.083\pm0.002$. Similarly for the reflection data, $\Delta_0/2\pi = 36.8\pm0.2$ MHz, $\Gamma/2\pi = 8.0\pm0.6$ MHz and $R_{sc} = 0.080\pm0.002$ were obtained. Both values are in agreement within their uncertainties, however, these values for R_{sc} do not match the expected $R_{sc} = 0.201$ for the experimental focusing parameter used which theoretically gives the upper bound. From section 2.3, it was shown that the transmission and reflection can be derived from R_{sc}. Using equations 55 and 58, a value of maximal extinction value of $1 - T = 8.2 \pm 0.2$ % and a peak reflectivity of 0.161 ± 0.007 % were obtained from fitted R_{sc} values respectively.

Both measurements show complementary dependence on the detuning, within the fit uncertainty. The centre frequency of the resonance line is blue shifted mostly due to the AC Stark shift induced by the optical dipole trap and partly due the bias magnetic field. The observed widths are slightly larger than the natural linewidth of the probed D2 line. (6.06 MHz). Although not fully understood, the cause of this broadening is most probably due to position dependent differential AC Stark shift present in the trap. Since the atom has some finite temperature, it moves around in the trap experiencing not only variations in the probe field intensity, but also varying AC Stark shifts.

3.3.1.1 *Temperature of the atom*

The temperature of the atom here refers not that of an ensemble of atoms since there is only one atom, but that of the atom after many different loading events. There are a number of possible ways to determine the temperature of the atom such as the release and recapture method [69], time-of-flight measurement [70] and Raman sideband thermometry [71]. In the first two techniques, the temperature is determined by simulating the dynamics of the atom with a certain temperature, T, after it has been released from the trap and comparing it with the experiment. In the first method, the recapture probability is simulated based on the trap parameters and the initial atom energy, while in the second method the rms spread of the atom is simulated based on the initial atom energy and the imaging light. The sideband thermometry technique measures the ratio of the red to blue sideband strength in a Raman absorption spectrum. For a thermal distribution, the ratio is directly related to the average occupational number of the atom in its harmonic potential, which can then be related to the temperature of the atom in the trap. Raman sideband thermometry is a nice temperature measurement technique since it is a more direct

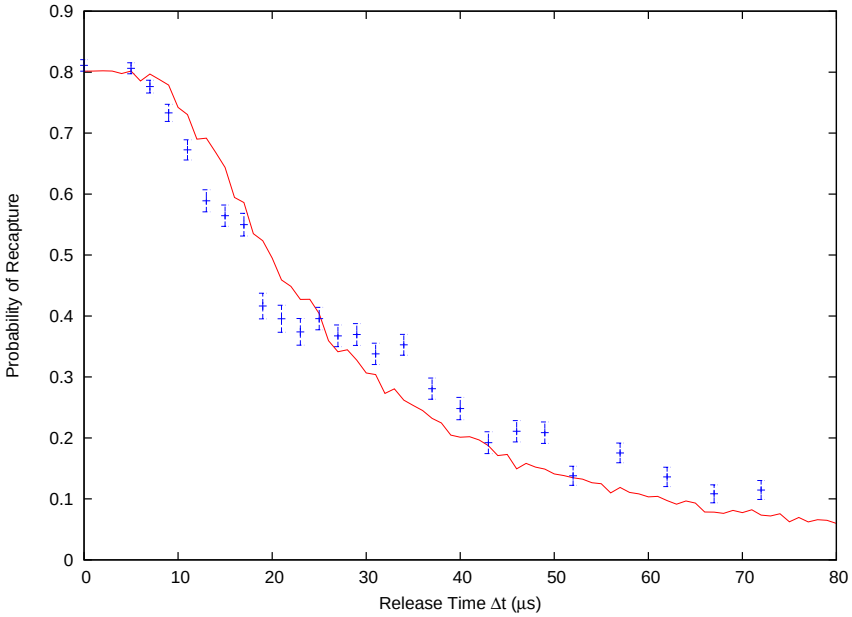

Figure 18: Probability of recapturing the atom after releasing the atom from the dipole trap. Although the trap is not switched off at $\Delta t = 0$, the probability is not unity. This is due to the loss of the atom during the finite measurement time of probing and checking for the atom. The solid line is a Monte Carlo simulation of the probability of recapture based on the energy of the atom. This simulation was done with an atom temperature of $\sim 34\,\mu K$ and using 500, 000 trajectories for each release time.

measure and also because of the ease to go a step further and cool the atom via Raman sideband cooling.

The release and recapture experiment was done to estimate the temperature of the atom [72]. The atom was released by switching off the dipole trap for a variable amount of time up to $80\,\mu s$ and then recaptured by switching it on again. The probability of recapturing is shown in figure 18 together with a Monte Carlo simulation of the experiment with an atom temperature of $34\,\mu K$. This temperature is much lower than the Doppler temperature of $T_D = 146\,\mu K$, and is caused by sub-Doppler cooling of the atom in the MOT.

The position averaged value for R_{sc} is $\simeq 0.15$ for $34\,\mu K$ and $\simeq 0.11$ for the Doppler temperature, both of which are still larger than what was measured. However since the atom is continuously being optically pumped and probed by the probe beam, the recoil from these processes will also increase the average energy of the atom. With a scattering rate of $2500\,s^{-1}$ the energy picked up in the z direction after 140 ms of probing is about $k_B \cdot 63\,\mu K$ without considering the recoil. A preliminary Raman cooling experiment is being done on the atom

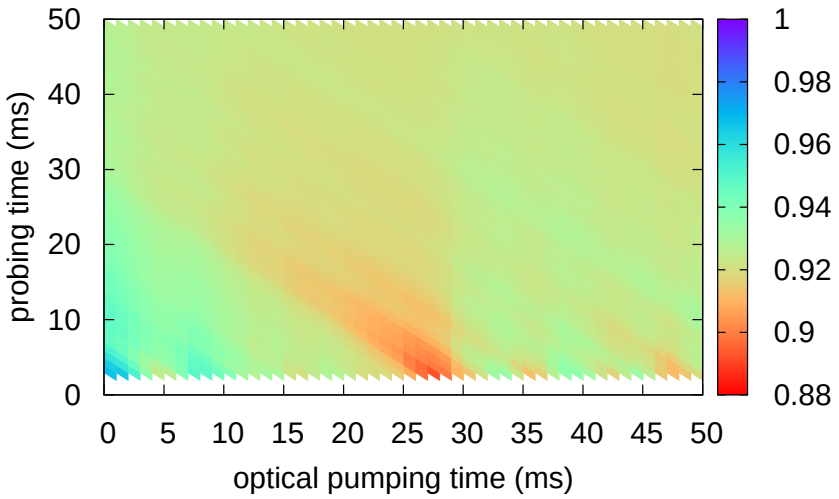

Figure 19: Transmission of the probe on-resonant as a function of optical pumping time and probing time.

(see section 4). The average occupational number of the atom in the harmonic trap can also be estimated from the measurement and was estimated to be $\simeq 6$ in the radial direction. If the motional axes in the other axes are assumed to have the same average energy, the average temperature is then $\simeq 24\,\mu$K. The discrepancy between the theoretical model and the experimentally measured results in not yet understood, however a possible source of error is that the model assumed classical motion for the atom. The effects of temperature of the atom on the experiments should be further examined.

3.3.1.2 *Varying of pumping and probing time*

A simple experiment to determine the effect of heating by the probe beam is done for the extinction experiment. For this particular experiment, instead of integrating the detector clicks into bins of 100 ms, all of the clicks and their time of arrival is recorded on a timestamp unit. The count rates for different time and durations can then be calculated by binning the clicks into the appropriate bins. Since the optical pumping and probing is done with the same $5S_{1/2}|F = 2\rangle$ to $5P_{3/2}|F' = 3\rangle$ beam that is on resonant, there is no clear transition when optical pumping is finished and when does probing begins. If detector clicks due to the probe beam immediately after the MOT is switched off are recorded, the data can be post-processed to allow for a variable amount of time set aside for optical pumping and an-

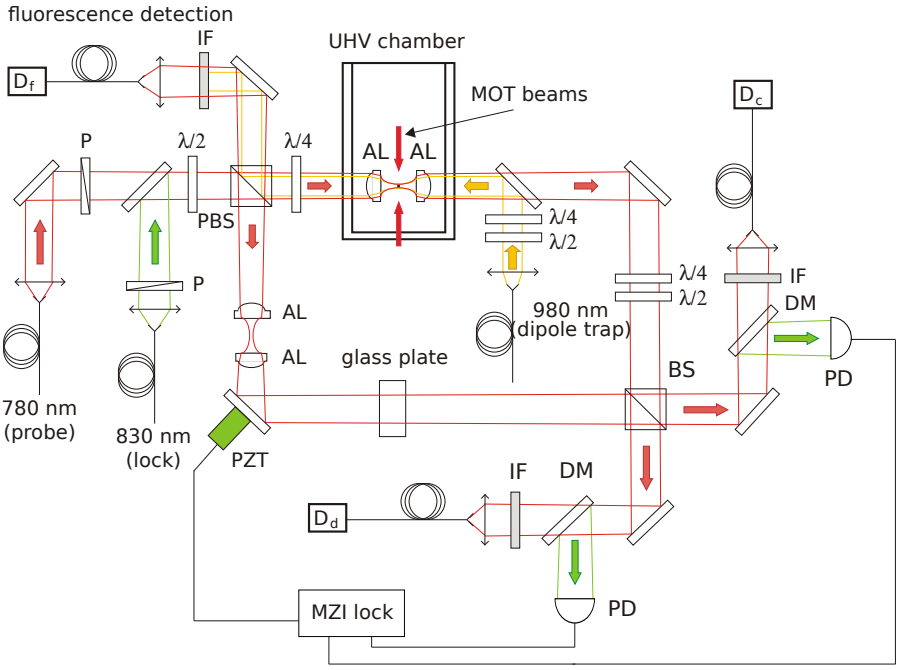

Figure 20: Setup for the phase shift experiment with a single atom trap in one arm of a Mach-Zender Interferometer.

other variable amount of time used to calculate the actual transmission. This transmission as a function of two variable for a probe beam that is on-resonant is shown in figure 19. It can be seen that there is an optimal optical pumping time for when the transmission goes to a minimum. This corresponds to the time that is needed to bring the atom into a two-level system, i.e. states $|g-\rangle$ and $|e-\rangle$.

Also visible is the drop in transmission when the optical pumping and probing times are increased. When the probing time is increased, the atom will scatter more light and gain more recoil energy. The cause of the decreased transmission is most probably due the heating up of the atom by scattering light from the beam.

3.3.2 *Phase shift*

The setup for the phase shift experiment is an extension of that for the transmission/reflection experiment as shown in figure 20. The probe beam is now sent through a stabilised Mach-Zender Interferometer (MZI), in which one arm sits the single ^{87}Rb atom trapped at the focus of the confocal aspheric lens pair and the other arm serves as a phase reference. Also, its waist parameter is slightly reduced to 1.1 mm corresponding to a focusing parameter, u, of 0.244. It is split and the ratio of optical power in both arms of the interferometer is

controlled with a half-wave plate and a polarizing beam splitter (PBS) such that the power at the input ports of the non-polarising beam splitter (BS), without an atom in the trap, is the same. The probe beam is again made circularly polarised with a quarter-wave plate before being focused on to the atom. After passing through the lenses, the probe beam polarisation is converted back to linear to match that of the reference arm. A pair of correction lenses was inserted into the reference arm to compensate for any difference in divergence of the two wavefronts at the output beamsplitter. The interference contrast (after coupling into the single mode fibres) had a visibility, V, of $98.0 \pm 0.2\,\%$. The output modes of the interferometer are then collected into single mode fibres with an efficiency of 84% without an atom in the trap, and guided to detectors $\mathrm{D_c}$ and $\mathrm{D_d}$.

The phase stability of the interferometer over the measurement time is ensured by locking it to an off-resonant laser ($\lambda = 830\,\mathrm{nm}$) co-propagating with the probe, and keeping the MZI close to zero optical path difference[7]. This auxiliary light is separated from the probe with dichroic mirrors (D) to provide a feedback signal to a piezo-electric actuator (PZT). Due to technical reasons, the dipole trap beam now comes from a direction opposite to the probe.

The measurement sequence is exactly the same as that for reflection/transmission measurement except that the count rates, t_c and t_d(t_c' and t_d') on detectors $\mathrm{D_c}$ and $\mathrm{D_d}$ are recorded instead, where the primed variables indicate the changed count rates due to the atom present in the trap.

The optical power after the beam splitter, $P_{c,d}$, — without the atom and up to a constant — is given by

$$P_{c,d} = \frac{1}{2}\Big[|E_a|^2 + |E_b|^2 \pm 2\,|E_a||E_b|\cos\phi_{ab}\Big], \tag{97}$$

where E_a and E_b are the field amplitudes in the atom and reference arms before the beam splitter respectively and ϕ_{ab} is the phase difference between the two MZI arms. Before the start of the measurement sequence, the MZI is locked to a position where it has maximal phase sensitivity which occurs for $\phi_{ab} = \pm 90°$ where $|E_a| = |E_b|$. This however does not imply that t_c and t_d are the same because of different coupling efficiencies in each channel and different detector dark count

7 Although the laser has a coherence length of several meters, the optical path length difference was kept to $< 2\,\mathrm{mm}$. This is because the wavelength of the 830 nm laser is not locked to a stable narrow frequency reference, only temperature stabilised. We estimate that for a change of frequency of 1 GHz, the interferometer path difference changes by $\sim 5\,\mathrm{nm}$ corresponding to a change in phase of the probe by $\sim 2°$. Although this seems a lot, in practise the actual frequency drifts are much smaller for the duration of the experiment, and the interferometer is frequently relocked before each measurement sequence.

rates. In general, $t_{c,d} = P_{c,d} + B_{c,d}$. It can be shown that at $\phi_{ab} = 90°$, the count rates in the detectors are,

$$t_{c,d}^{\text{lock}} = \frac{t_{c,d}^{\max} - t_{c,d}^{\min}}{2} + B_{c,d}, \tag{98}$$

where $t_{c,d}^{\min,\max}$ are the minimal/maximal observed count rates for phases $\phi_{ab} = 0°, 180°$ and $B_{c,d}$ are the detector background rates. The actual phase difference of the MZI arms, without the atom, can be inferred from the measured count rates as,

$$\phi_{ab} = \arccos\left[\frac{P_c - P_d}{P_c + P_d}\right]. \tag{99}$$

With the atom in the trap, the probe beam is scattered causing a power drop in the arm. Using the same convention as before, we have

$$P'_{c,d} = \frac{1}{2}\left[\left|E'_a\right|^2 + |E_b|^2 \pm 2\left|E'_a\right||E_b|\cos\phi'_{ab}\right], \tag{100}$$

where $|E_b|$ remains unchanged. The new phase difference is given by,

$$\phi'_{ab} = \arccos\left[\frac{P'_c - P'_d}{(P_c + P_d)\sqrt{T}}\right], \tag{101}$$

where T is the transmission of the probe beam in the atom arm,

$$T = \left|\frac{E'_a}{E_a}\right|^2 = \frac{2\left(P'_c + P'_d\right)}{P_c + P_d} - 1. \tag{102}$$

Note that for the relations in equations 101 and 102 to hold, $|E_a| = |E_b|$, which is satisfied by the high visibility of the empty interferometer. The optical powers $P_{c,d}$ and $P'_{c,d}$ can be calculated from the count rates via

$$P_{c,d} = \frac{t_{c,d} - t_{c,d}^{\min}}{t_{c,d}^{\max} - t_{c,d}^{\min}}, \qquad P'_{c,d} = \frac{t'_{c,d} - t_{c,d}^{\min}}{t_{c,d}^{\max} - t_{c,d}^{\min}}. \tag{103}$$

Finally, the phase shift induced by the atom can be calculated simply as,

$$\delta\phi = \phi'_{ab} - \phi_{ab}. \tag{104}$$

In the same experimental run (i.e. for the same detuning of the probe frequency), a complementary independent measurement of the transmission T of the probe with the reference arm blocked was performed using the same measurement sequence, which has a better signal to noise ratio.

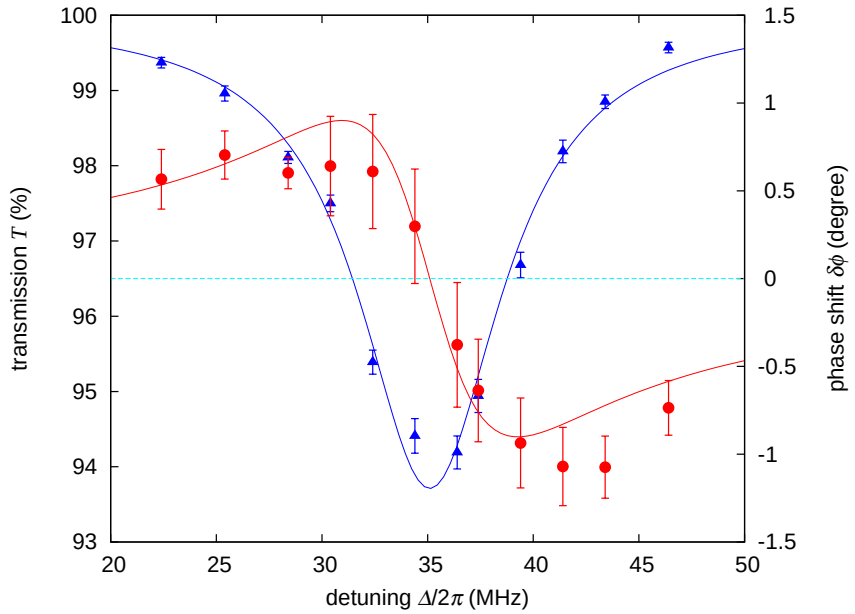

Figure 21: Phase shift $\delta\phi$ observed on a weak coherent probe beam tuned across the resonance of a single atom (red, filled circles), showing the dispersive character from phase retardation below resonance to phase advancement above resonance with respect to the freely propagating beam without the atom. The transmission, T, for the same probe (eqn. 102) is shown for reference (blue, filled triangles). The solid curves are theoretical plots with the same parameters. The parameters are extracted from the fit to the transmission data. Error bars in the data are from propagated Poissonian counting statistics.

Results

The results of the phase shift measurement is shown in figure 21. Because of the small signal to noise ratio and the large uncertainty of the the phase shift data, the transmission data was used to extract the best fit parameters using equation 56. The best fit parameters are, $\Gamma/2\pi = 8.2\pm0.5\,\text{MHz}$, $\Delta_0/2\pi = 35.1\pm0.2\,\text{MHz}$ and $R_{sc} = 0.064\pm0.004$. Using the values of the fit, equation 60 is plotted and is in reasonable agreement with the data points. Similar to the transmission/reflection experiment, the linewidth is also slightly broader than the natural linewidth of the atomic transition (6.06 MHz). The maximal phase shift occurs at $\Delta = \Gamma/2$ and according to equation 60, has a value of 0.93°.

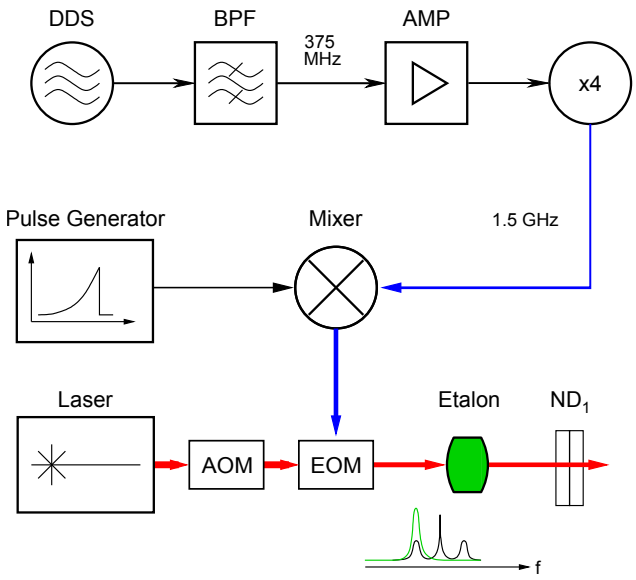

Figure 22: Setup for preparation of optical pulses with exponential or square waveforms. DDS: direct digital synthesizer, BPF: bandpass filter, AMP: RF amplifier, AOM: acousto-optic modulator, EOM: electro-optic modulator. See details in the text.

3.4 PULSED EXCITATION EXPERIMENTS

The second set of experiments were done with strong pulses of the probe beam where the Rabi frequency is now $\Omega \gg \Gamma$ and the length of the pulses is on the order of the lifetime of the excited state. In this limit, scattering ratio, R_{sc}, is no longer a good quantity as the assumptions that was made in section 2.1.2 are no longer valid. Since we do not have a source of single photon number states, the experiments are only done with coherent states from a cw laser from which the pulses are generated using an optical modulator. The atom is now optically pumped to a dark state. In this set of experiments, the probe detuning is fixed to be on resonance while the pulse bandwidth and average number of photons in a pulse are varied.

3.4.1 *Pulse generation*

The setup for generating optical pulses with a variable temporal overlap is shown in figure 22. The basic idea of optical pulse generation is to exploit the fast bandwidth of the EOM as a phase modulator. A radio-frequency (RF) signal with the desired temporal envelope is fed into a fast fibre coupled EOM (EO-Space 20 Gb/s phase modulator). The sidebands that are created at the optical carrier frequency

plus/minus the RF frequency will have an electric field that is modulated temporally by the envelope that was used.

A 1.5 GHz sine wave was chosen as the modulation frequency for ease of frequency stabilisation and filtering of the carrier later on. This RF frequency was derived from a home built circuit with components from Mini-Circuits. A digital direct synthesizer (DDS) generates a 375 MHz sine wave which passes through a band pass filter[8] before being amplified. The amplified sine wave is then multiplied by 4 through two second harmonic frequency multipliers to get the required 1.5 GHz RF frequency. The RF is used as a local oscillator input of a double-balanced mixer . The intermediate frequency input is fed with an electric signal with the desired temporal envelope. For a square pulse, the signal was generated from a NIM signal generator.

The rising exponential electrical signal was obtained from a home built circuit which uses the relation between the base voltage and collector current of a fast RF transistor. This relation is [73],

$$I_C = I_S \left[\exp\left(\frac{V_{BE}}{V_T} \right) - 1 \right], \tag{105}$$

where, I_C is the collector current, I_S is the reverse saturation current, V_{BE} is the base-emitter voltage and $V_T = k_B T / e \approx 26\,\text{mV}$ at room temperature, is the thermal voltage. Thus if V_{BE} is a linearly increasing in time, and for $I_C \gg I_S$, the collector current will, in good approximation, grow exponentially before it saturates. The linearly increasing V_{BE} is obtained by charging a capacitor with a constant current. The time constant of the exponential pulse can be controlled by choosing a suitable charging current and capacitance of the capacitor.

After the mixer, the RF input to the EOM has a trace that looks like figure 23. The residual modulation after $t = 0$ is taken care of by appropriately switching off the optical light to the EOM using the AOM. The beam is sent to the EOM with its polarisation aligned to the modulation axis defined by the key of the input fibre to the EOM. The RF pulse is mixed with the beam in the EOM to give a modulated optical pulse at the sidebands, 1.5 GHz away from the carrier frequency. At a very low modulation depth, $V_{\text{mod}} \ll V_\pi$, the response of the EOM is approximately linear and the sidebands will have the temporal profile of the RF pulse[9]. Finally, one of the sidebands is filtered with optical cavities which transmits 60% of the sideband and suppresses the other

8 The band pass filter is made from a simple narrowband stripline that only allows 375 MHz to pass and suppresses the spurious frequencies by at least 24 dBc.

9 The amplitude of the sidebands created by the EOM follows the Bessel function. For a weak enough modulation, the amplitude of the first order sidebands respond linearly with the modulation amplitude.

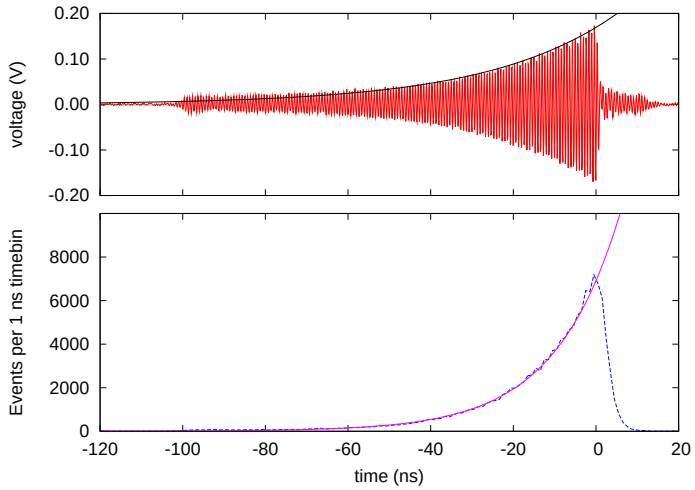

Figure 23: (Top) A 1.5 GHz RF frequency enveloped by a ≈ 30 ns rising exponential and a fast cut-off at $t = 0$ measured with a 2 GHz oscilloscope. The black solid line is exponential with a time constant 31 ns . (Bottom) A histogram of the APD clicks after sending the 18 250 000 attenuated pulses. The magenta solid line is a fit to an rising exponential and gives a time constant of 15.7 ± 0.1 ns.

unwanted frequencies by at least ≈ 60 dB[10]. The filtered pulse is attenuated to the required optical power via neutral density filters (ND_1) and then coupled into a single-mode fibre to be sent to the atom. Figure 23 shows the histogram of the number of clicks per 1 ns time bin when many identical copies of the attenuated optical pulse is sent to an APD. As can be seen, the optical histogram follows a rising exponential with a risetime half of that of the envelope of the RF. A more detailed description of the circuit is found in Appendix C .

To get the final optical frequency of the pulse to be on resonant with the Stark shifted $|g-\rangle \leftrightarrow |e-\rangle$ transition[11] the initial probe laser is locked to the ^{85}Rb transition of $5S_{1/2}|F = 3\rangle$ to $5P_{3/2}|F = 4\rangle$ with a frequency, ν, of 384.229 240 THz. The first order of the double pass AOM increases the frequency by 2×210 MHz. The red-sideband of the output of the EOM has an absolute frequency of 384.228 160 THz which is ≈ 40 MHz blue detuned from the unperturbed $|g-\rangle \leftrightarrow |e-\rangle$ transition.

3.4.2 *Experimental procedures*

For this experiment, it is essential to have timing information of each detector click. To achieve this, a 4 channel timestamp unit with a

10 Three cavities are used, each with a transmission of 85% and suppression of ≈ 20 dB

11 See page 32 for relevant transition. $\nu_{\text{red}} = \nu + 2 \times 210\,\text{MHz} - 1.5\,\text{GHz}$

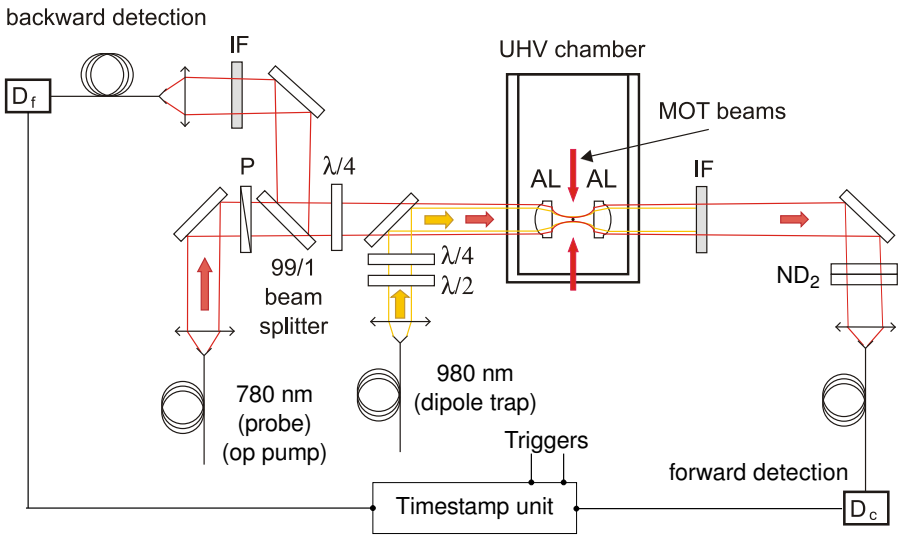

Figure 24: Setup of the pulsed experiment is almost exactly the same as that for the transmission and reflection experiment except for the additional neutral density filters (ND_2) to prevent saturation of detector D_c and the timing events of each detector clicks are recorded on the timestamp unit.

temporal resolution of ≈ 450 ps is used. Two channels are used as triggers and two other channels receive the clicks from the APDs. After each registered event, the timestamp has a deadtime of 120 ns before the next event can be registered. To compensate for this deadtime, a cable delay of 300 ns was added to one channel of the unit from one of the APDs. Before each optical pulse is generated, a trigger is sent to the timestamp, one channel for a pulse with the atom in the trap, and another for without an atom, for background measurement. The histogram is obtained by arranging the detection time into bins with temporal widths Δt_b and plotting the probability to find a click in each bin per trigger pulse.

The experimental setup itself is very similar to the one used for the transmission and reflection experiment. The main difference is the inclusion of neutral density filter filter ND_2 and a dark-state optical pumping stage is now used instead (See figure 24). The probe and the collection optics now have a smaller waist before the confocal aspheric lens pair. Also, the sequence is slightly modified to:

1. Switching off the MOT quadrupole coils.
2. The MOT beams are slightly further detuned to about 30 MHz and left on for 5 ms for molasses cooling.
3. Applying of a bias magnetic field of ≈ 2 Gauss along the quantisation axis.

4. 10 ms of optical pumping into the $|g-\rangle$ state which is done via the optical pumping beam on the $F = 2 \rightarrow F' = 2$ transition on the D2 line. In this time, the current supplying the bias magnetic field also should have stabilised.

5. After preparation, 100 identical optical pulses are sent to the atom. The repetition rate is mostly limited by the dead time of the detector and the length of each pulse and in this case is set to be 83.1 kHz. A trigger is sent to one channel of the timestamp unit 550 ns before the optical pulse is sent. The timestamp unit is gated such that only clicks from when the optical pulse is present at the atom and up to 400 ns after the end of the pulse is recorded.

6. Next, the MOT beams are turned on to check if the atom had remained in the trap, again by monitoring fluorescence at detector D_f. In this step, the MOT quadrupole coils are not switched on and the bias magnetic field is switched off. This whole process takes about 20 ms. At the end of this step, the MOT beams are switched off and if the atom is still in the trap, steps number 2 through 6 repeated again.

7. Otherwise, the background measurement is done. Background measurement is exactly the same at step 5 but with the trigger sent to another channel of the timestamp and 250,000 identical optical pulses sent instead[12].

8. After performing the background measurement, the MOT beams and MOT quadrupole coils are switched on again to load another atom into the dipole trap.

Measurement of pulse parameters

Two different pulse shapes were used in the experiment: rectangular and rising exponential. The RF envelope shape for the rectangular pulse is,

$$\mathcal{E}_{\text{rect}}(t) = \begin{cases} \sqrt{\Omega} & \text{if } 0 \leq t \leq \frac{1}{\Omega} \\ 0 & \text{elsewhere} \end{cases} \tag{106}$$

12 The reason why the background measurement is done with 250,000 pulses is because of the relatively long lifetime of the atom in the trap. The background measurement takes 3 s while the lifetime of the atom in the trap is about 9 s and during this time about 25,000 pulses are sent to the atom.

and for a rising exponential,

$$\mathcal{E}_{\exp}(t) = \begin{cases} \sqrt{\Omega}\exp\left(\frac{\Omega}{2}t\right) & \text{if } t \leq 0 \\ 0 & \text{if } t > 0 \end{cases} \tag{107}$$

where Ω is the frequency bandwidth of the pulse. The properties of the pulse can be extracted from the histogram of the photodetection events on detector D_c during the background measurement.

The average number of photons per pulse is obtained by summing all the detected events, $N_{d,i}$ in unit time bin, Δt_i of detector D_c for the duration of the pulses and normalising it by the number of triggers sent, N_T, and also the attenuation due to losses in the beam and detector efficiency, η_c, and also the stack of neutral density filter ND_2. The average photon number is then,

$$n = \frac{1}{\eta_c \eta_{ND_2} N_T} \sum_i N_{d,i}. \tag{108}$$

The losses were measured to be $\eta_c = 0.30 \pm 0.02$ which include the detector efficiency of D_c, coupling losses to a single mode fibre and reflection losses from all optical components. η_{ND_2} is measured to an uncertainty of 0.5 % and is varied from 2.5–5.1 dB. The bandwidth of the rectangular pulses are extracted directly from the histogram. The exponential histogram is fitted to the fit function:

$$N_d(t) = \eta_c \eta_{ND_2} n N_T \exp\left(\frac{t - t_0}{\tau}\right) \times \left(\exp\left(\frac{\Delta t}{\tau}\right) - 1\right), \tag{109}$$

where the first exponential term reflects the temporal envelope function and the second is due to the Poissonian distribution of photocounts. The time constant, τ, is extracted from the fit.

The parameters that were varied in the experiment were the average photon number per pulse and the bandwidth for both rectangular and exponential pulse shapes. As the bandwidth of the pulse decreases, it looks more and more like a cw probe to the atom. The maximum average photon number per pulse is limited by the peak instantaneous power available from the probe beam and also limited by the heating of the atom especially for the exponential pulse with the smallest bandwidth. The minimum average photon number is limited by the signal to background ratio of the detectors used, while maximum bandwidth is determined by the electronics used to generate the electrical pulse fed into the EOM.

Because the forward detector, D_c, is dead just after the pulse is sent to the atom, all relevant information about the dynamics of the in-

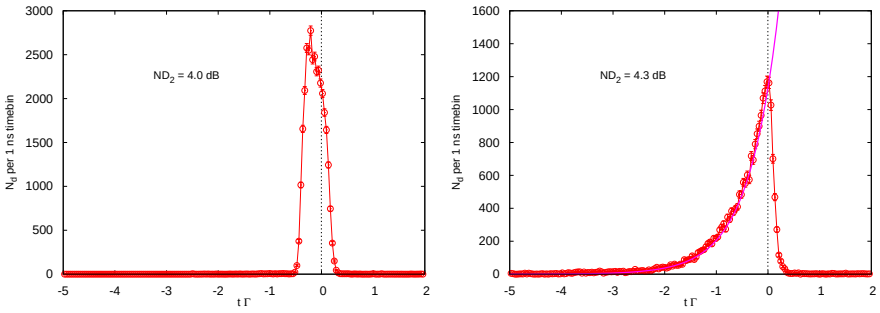

Figure 25: Rectangular and rising exponential excitation pulses. Histograms show the number of detected events, N_d in 1 ns time bin versus time expressed in the units of natural decay rate $1/\Gamma = 26.24\,\text{ns}$ of the D2 line in ^{87}Rb. (Left) Rectangular shaped pulse with a temporal bandwidth of 15 ns. (Right) Rising exponential pulse with a characteristic risetime of $\tau = 15\,\text{ns}$. The solid magenta line is a fit according to equation 109

teraction of the pulse with the atom is recorded by the backward detector, D_f, which is an actively quenched Perkin-Elmer single photon counting module. The spatial overlap of the detector collection mode and the dipolar emission pattern of the atom, Λ, can be calculated by doing a mode overlap integral of the Gaussian mode of the collection optics and the dipolar emission mode of the rotating electric dipole. It can also be determined experimentally by measuring the reflection of the atom for a cw beam. A collection efficiency of $\approx 2.7\,\%$ is measured.

3.4.3 *Results*

Figure 26 shows the histogram of detector events for an exponential pulse with average photon number, $n = 104 \pm 6$, and a characteristic risetime of 15 ns. As mentioned in section 2.5, a possible way to quantify interaction of the light pulse with the atom is through the measurement of the excitation probability of the atom. With an atom in a 2-level system, this probability is directly related to the atomic scattering/fluorescence of the atom, which is detected with detector D_f. The temporal evolution of the detected events is directly related to the expectation value of the atomic operator from which the excitation probability can be determined. The probability of detecting an event in time bin, Δt, per trigger, $P_{d,i}$, is related to the excitation probability, $P_{e,i}$, as

$$P_{d,i} = \frac{N_{d,i}}{N_T} = P_{e,i}\Gamma\Delta t\eta_f \frac{3}{8\pi}\Lambda_f, \tag{110}$$

where $P_{e,i}\Gamma$ is the rate at which the atom scatters photons, η_f=0.30 ± 0.02, is the losses through the backward arm to detector D_f inclusive

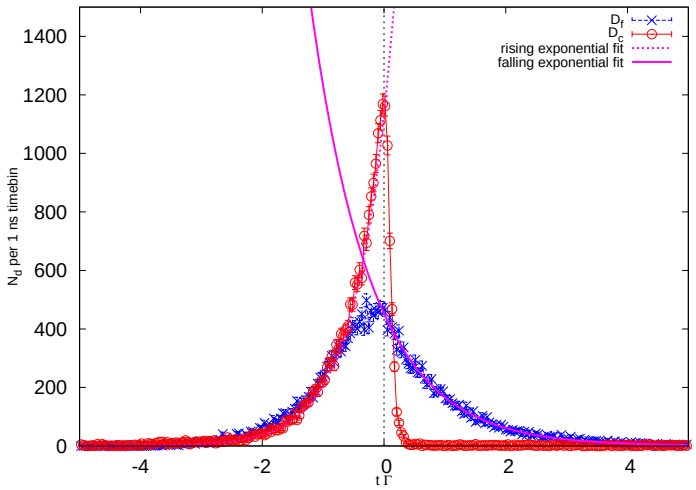

Figure 26: Histogram of detector events for an exponential excitation pulse. The red circles are recorded during the background measurement while the blue crosses are recorded when the atom is present during the pulse. In this histogram, the background measurement is recorded over 14 750 000 triggers with an, $\eta_{\mathrm{ND}_2} = 4.3\,\mathrm{dB}$, while the other measurement is recorded over 2 103 400 triggers.

of the coupling to the single mode fibre and the quantum efficiency of the APD and, $\Lambda_f = 0.027 \cdot \frac{8\pi}{3}$, is the solid angle extended by the collection optics.

In figure 26, the blue data set shows the evolution of the detected events on detector $\mathrm{D_f}$ as a function of time. There are two regions of interest, one where the pulse is still present and the other where the pulse is absent. They correspond to the coherent and incoherent part of the evolution of atomic operators. The falling exponential due to the fluorescence (incoherent) has a decay rate of $\Gamma = 26.29 \pm 0.05\,\mathrm{ns}$, where the error quoted is statistical error from the fit. To compare the interaction between rising exponential and square shaped pulses, the maximal excitation probability, $P_{e,\max}$, is plotted with respect to the average photon number in the pulse for different bandwidths as shown in figure 27.

It can be seen that as the bandwidth of the pulse decreases (larger time), the value of $P_{e,\max}$ saturates at 0.5 for the exponential pulse while for the rectangular pulse, it keeps on increasing. This is because as the bandwidth decreases the exponential pulse, with its long tail, resembles cw light to the atom and the excitation probability for cw light, after long times, is 0.5. For the rectangular pulse however, since the edge is sharp, the beginning of the pulse is always sufficient to excite the atom to a large $P_{e,\max}$ before it begins to look like a cw light

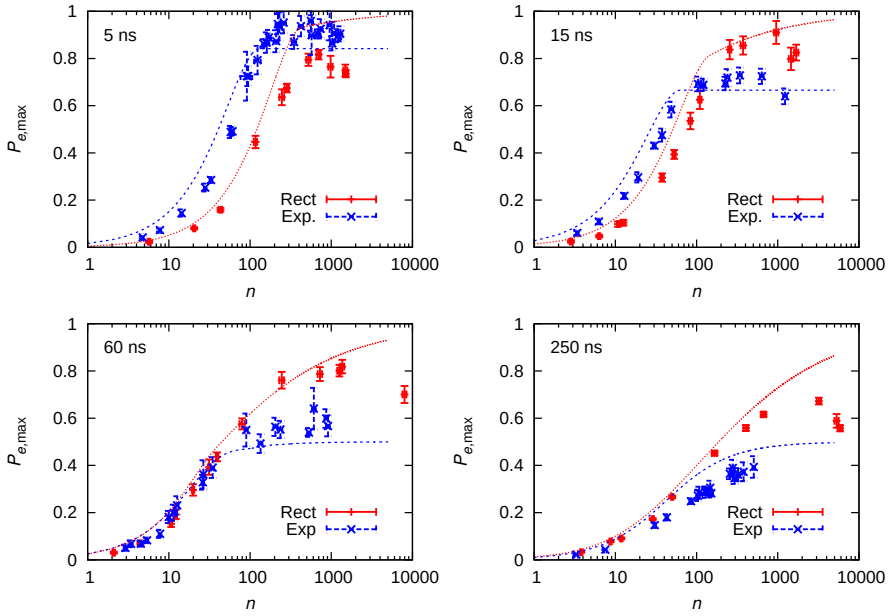

Figure 27: Maximal excitation probability versus the average photon number in the pulse with different temporal bandwidths. The theoretical curves were obtained by numerically solving differential equations for time-dependent evolution operators [3].

to the atom. As such the $P_{e,\max}$ will eventually approach unity for large enough value of n for the rectangular pulse.

For the largest bandwidth ($\Omega^{-1} = 5\,\text{ns}$), the data points for both the exponential and rectangular pulses do not follow the theoretical curves after the turning point. This is still not understood but might be due to the deviation of the experimental parameters from the theoretical definition used. For the exponential pulse, the tail is finite and extends to about 25 ns. Hence it will not saturate as quickly compared to an infinitely long pulse. The square pulse on the other hand has a finite rise- and fall-time of ≈ 3 ns which for this bandwidth, looks more like a triangular pulse.

As the bandwidth approaches the optimal value of $\frac{\Omega}{\Gamma} \approx 1$, the number of average photons needed to excite the atom to a particular $P_{e,\max} < 0.6$ reduces to a minimum or conversely, for a fixed photon number, say $n < 50$, the value of $P_{e,\max}$ is maximum close to the optimal bandwidth. However, since larger bandwidths (shorter pulse) are not easily accessible, the extrema are not so clearly distinguished.

Another clear trend is the higher value of $P_{e,\max}$ for an exponential pulse compared to a pulse with a rectangular profile for pulses with optimal and larger bandwidths and for small values of n. It should be noted however, that the optimal bandwidth is not really a well defined

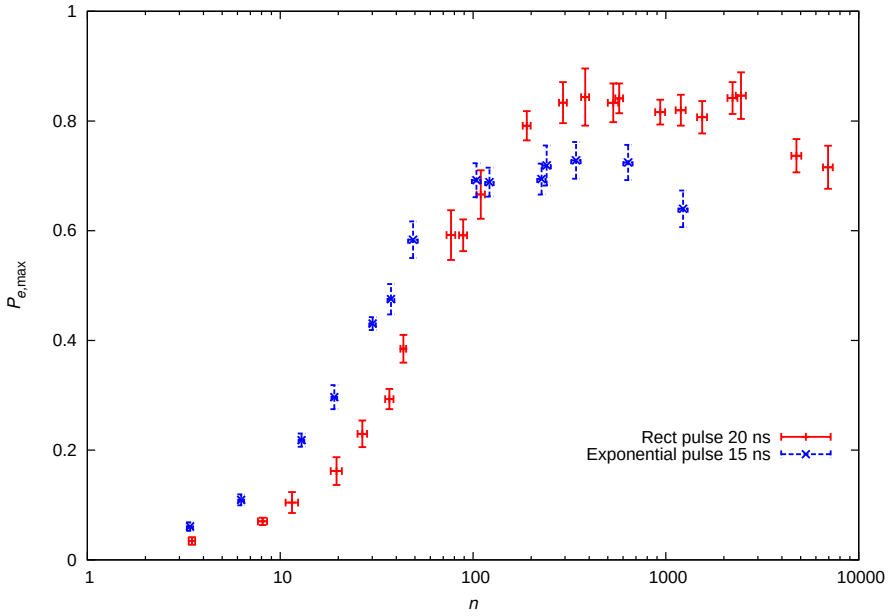

Figure 28: Maximum excitation probability versus average photon number for rectangular and exponential pulses at their respective optimal bandwidths (at $n = 1$).

parameter. This is because $P_{e,\max}$ is dependent not only on the pulse shape but also both Ω and n, even for a coherent pulse. However, it is quite obvious that a rising exponential pulse gives a larger $P_{e,\max}$ than a rectangular one for a bandwidth that is optimal or larger and for an n that is below saturation. Following [3], for an average photon number of $n = 1$ we can define an optimal bandwidth of 1.9Γ ($\Omega^{-1} = 15\,\text{ns}$) for a rising exponential pulse and 1.3Γ ($\Omega^{-1} = 20\,\text{ns}$) for a rectangular pulse. In figure 28, it can be seen that for $n < 100$, the exponential pulse always attains a larger value of $P_{e,\max}$ than the rectangular pulse for a similar n. As the atom saturates ($n > 100$) the value of $P_{e,\max}$ for the rectangular pulse overtakes that of the rising exponential.

Looking at $P_{e,\max}$, the full coherent dynamics of the atom cannot be seen, since the maximal excitation probability only occurs at the early stage of the pulse, before any incoherent radiative decay sets in. Figure 29 shows the evolution of P_e for pulses with characteristic time 15 ns and a large enough average photon number ($n \approx 1300$) such that Rabi oscillations are visible on both the exponential and rectangular pulses. As can be seen, the oscillation amplitude gradually decays due to the incoherent scattering before the pulse is switched off. Once the pulse ends, the atomic evolution is just given by it's coupling to the vacuum mode and it will decay to the ground state with a characteristic lifetime of $\Gamma = 26.24\,\text{ns}$ [74, 48]. The data points fall approximately

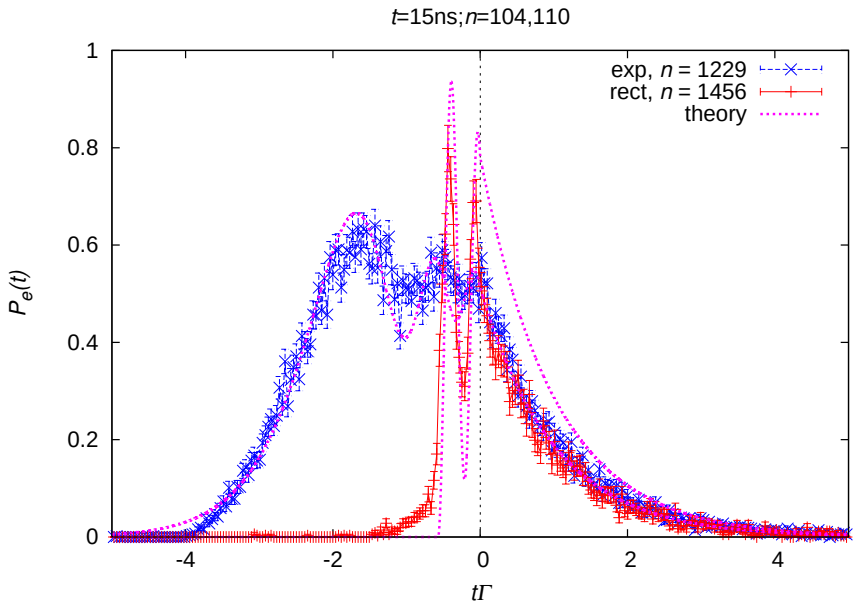

Figure 29: Excitation probability, P_e, versus time in units of the natural radiative lifetime, $\Gamma = 26.24\,\text{ns}$, for pulses with a characteristic time of 15 ns and average photon number of≈ 1300. The dashed magenta lines are numerical solution of the time-dependent operators with $\Lambda = 0.03$ and n as that measured from the data.

on the theoretical simulations for both pulse shapes except for the incoherent part of the rectangular pulse. This may be due to the finite fall time of the rectangular pulse in the actual experiment and hence stopping at a different phase of the Rabi oscillation. On hind sight, the theoretical curves could have been computed with the actual experimental pulse shapes that was used in the experiment, i.e. finite rise and fall time instead of infinitely sharp edges. However, the main physics and dynamics of the interaction would still be the same.

In order to compare the dynamics of atom for various parameters of the pulse and pulse shapes, the excitation probability at a fixed time, $P_e(t)$, say $t = 0$, can be extracted and plotted. Because the evolution of the radiative decay part is very much an exponential with

$$P_e(t) = P_e(t = 0)\exp(-\Gamma t), \tag{111}$$

the quantity $P_e(t = 0)$ can be also extracted by integrating $\Gamma P_e(t)$ from $t = 0$ to ∞ to get better statistics on the value or summing in the case of discrete bins with width Δt,

$$P_{e,\text{tot}} = \Gamma \Delta t \sum_{i=0}^{\infty} P_{e,i}. \tag{112}$$

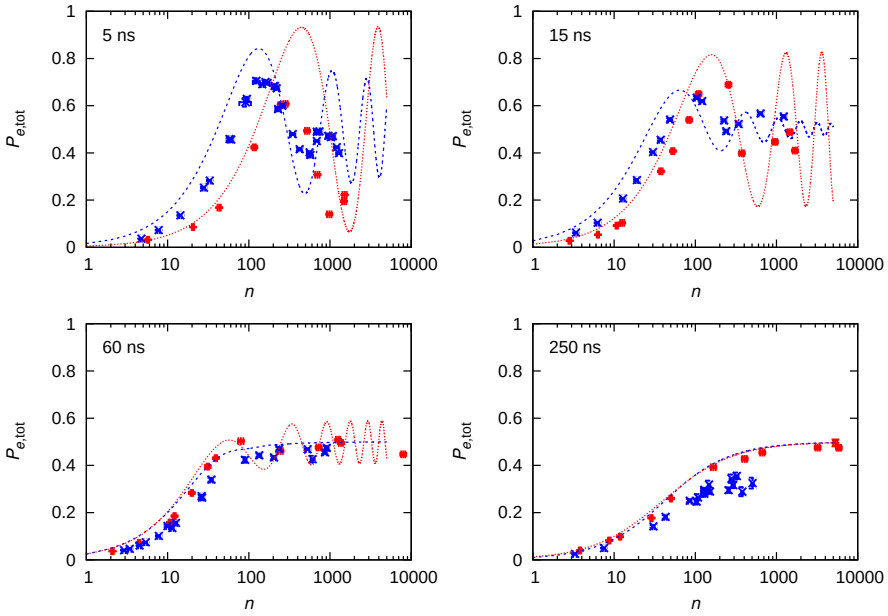

Figure 30: Excitation probability at $t = 0$, extracted from $P_{e,\mathrm{tot}}$, versus average photon number n for exponential (blue crosses) and rectangular (red pluses) pulses of various bandwidth. The theoretical curves were again solved numerically with $\Lambda = 0.03$.

The quantity $P_{e,\mathrm{tot}}$ is then plotted versus average photon number n for different bandwidths and pulse shapes in figure 30. Oscillations are clearly visible for both exponential and rectangular pulses for large bandwidths. For the smallest bandwidth ($\Omega^{-1} = 250\,\mathrm{ns}$), no oscillations are visible as the atom losses all coherence at $t = 0$. In all other cases it can be seen that $P_{e,\mathrm{tot}}$ decays to 0.5 for an exponential shape and oscillates around 0.5 for a rectangular shaped pulse.

Although the datapoints do not fit nicely to the theoretical curves, the trend of the experimental data points is clearly similar to that of theory. It can also be seen that for an atom with a relatively short lifetime, defining a π-pulse that inverts the atomic population is not an easy task as both the pulse duration and the power in the pulse need to be kept relatively constant for the atom to end up in the excited state at the end of the pulse.

3.5 CONCLUSION

In conclusion, two quantities that quantify atom-light interaction in two different regimes were experimentally measured. For the case of a weak coherent continuous probe beam, the scattering ratio, R_{sc}, was measured from two complementary measurements and related to

three measurable quantities: transmission(extinction), reflection and the phase shift induced. Simultaneous measurements of extinction and reflection of $91.8 \pm 0.2\,\%$ and $0.161 \pm 0.007\,\%$ both give similar values of R_{sc} within the statistical uncertainty. Similar measurements were done with extinction and phase shift, although the value of R_{sc} was only extracted from the extinction measurement and used to plot a theoretical phase shift curve. A maximal phase shift of 1° is measured. The experimental values of R_{sc} does not match the theoretically predicted values. A more careful study on the effects of temperature of the atom on the measured R_{sc} is important in order to fully understand the source of this discrepency.

For a strong coherent pulsed probe, the excitation probability P_e was measured directly from the observed scattering/fluorescence of light from the atom. It was seen that for this overlap of $\Lambda \approx 0.027 \cdot \frac{8\pi}{3}$, the atomic transition saturates for an average photon number of $n \approx 60$ in a pulse. Also it was seen that the shape and the temporal bandwidth of the excitation pulse is important for achieving a maximum P_e for a minimum n. For a bandwidth that is comparable or larger the atomic lifetime, and before the pulse reaches saturation, the rising exponential pulse has a larger probability to excite the atom into the excited state. This then implies that to efficiently couple a light pulse or a photon strongly to an atom without a cavity, not only is strong focusing necessary, tailoring the shape of the pulse will also benefit this endeavour.

4

CONCLUSION AND FUTURE OUTLOOK

It has been experimentally shown that a single atom can significantly scatter a strongly focused continuous wave Gaussian beam even though the excitation probability of the atom itself is quite small for such a cw probing. When a pulsed probe is sent to the atom instead, the atom saturates with an average number of about ≈ 60 photons in a pulse. It was also shown that the temporal profile of the pulse is important although the difference in excitation probability for a coherent pulse is not that obvious. It is more interesting to send temporally shaped real single photon pulses to the atom [3]. Possible sources of deterministic single photons [75] that has frequency and linewidth close to that of the atomic transition frequency are those from ensembles of Rubidium [76], a single Rubidium atom in a cavity [77, 78] or in free space [30]. A heralded single photon source can also be used with the most common example being a bright spontaneous parametric down source either generated in an interferometer [79] and subsequently filtered to the narrow atomic transition frequency line and then sent to the atom[80].

However, temporally shaping these single photons cannot be done with the current technique that was performed on the coherent pulses since it is too lossy. Other methods of single photon shaping [81] and/or generation [82, 83] need to be investigated. Currently, only 3% of the maximum overlap Λ is in use to excite the atom. And even for a maximum focusing strength of $u = 2.239$, the overlap expected is just $\Lambda = 0.364 \cdot 8\pi/3$ and thus a maximum excitation probability of 0.36 for a single-photon Fock state pulse [3] with perfect temporal overlap. In order to get a higher excitation probability, the pulse has to come in from all sides of the atom while still be in a single mode of the electromagnetic radiation in the basis of the dipole vector. This can be done by using a deep parabolic mirror as is being pursued by the group of Gerd Leuchs [84]. For that experiment, the mirror transforms a plane electromagnetic wave with a suitably chosen radial polarisation into an inward-moving dipole wave that addresses the π dipole transition.

Another possibility of addressing the atom from all sides is to split the single photon on a beamsplitter and send it to the atom from both sides using both lenses. The atom is then in a superposition of being excited from the left and right by the single photon. The phase of the left and right path needs to interfere constructively for the excitation probability to be twice compared to a single sided excitation. The

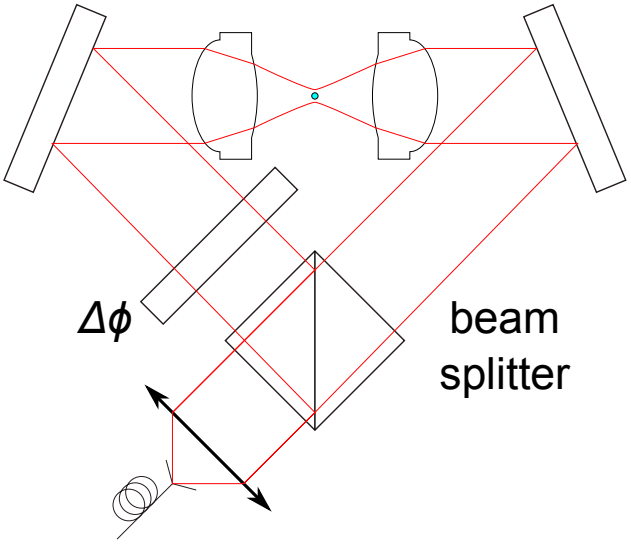

Figure 31: Excitation of a single atom from both sides by splitting a single photon on a beam splitter and sending both outputs to the atom. The phase of one arm, $\Delta\phi$, is adjusted such that the two arms of the photon arrive at the atom with the same "phase". To detect the fluorescence of the atom, the phase $\Delta\phi$ can be changed by π after sending the excitation pulse such that the photon generated always exits from the other (unused) port of the beam splitter which then can be detected by a single-photon detector (not shown).

maximal excitation probability will then be 0.72 for just a simple focusing of a single photon with a Gaussian spatial profile and rising exponential temporal profile with optimal rise time. Although it seems counter-intuitive that splitting a photon into two different modes on a beamsplitter can still result in a single mode excitation of the atom, this is just due to the choice of plane-waves as a typical basis mode of a beam splitter. If the spherical modes corresponding to the standard electric dipole radiation transition of $\pi, \sigma^{\pm}$ are taken as basis modes instead, the single photon can still be written as a single excitation of the vacuum mode.

Figure 31 shows a schematic of how such an excitation experiment may look like. An obvious problem would be to how to detect the dynamics of the atom (from the fluorescence) since all sides of the atom are now covered by the excitation mode. A simple way is to adjust the phase of one of the arm of the interferometer such that the fluorescent photon always exits at the unused port of the beam splitter. This reversibility of transforming the input (output) of the beam splitter mode into (from) a dipole wave (assuming that the lenses do perfect transformations) with a correctly chosen relative phase $\Delta\phi$, would show that exciting the atom from both sides should be possible.

Another challenge is to reduce the average temperature of the atom in the trap, such that the atom stays in the region of maximal electric field strength, assuming the dipole trap and the probe beam is perfectly overlapped. One way of "cooling" is to lower the power of the dipole beam and hence the trap depth such that only the colder atoms stay trapped before probing the atom and keeping the results only if there's an atom left after the probing cycle which was done by Tuchendler et al. [69]. To have a really deterministic way of cooling the atom, a different cooling technique needs to be employed. Raman sideband cooling is one such method, where not only is the atom cooled, but the final temperature of the atom can also be determined from the ratio of the final sidebands [55]. If a successful application of sideband cooling is possible, the atom can theoretically be cooled to the motional ground state of the trap, if it's recoil frequency (energy) is less than the trap frequencies (energies). In the case of ^{87}Rb, the recoil frequency is $2\pi \cdot 3.77\,\mathrm{kHz}$ [48], which is less than the trap frequencies used. At the ground state of the trap, the spread of the atomic wavefunction, are 32 nm and 91 nm in the lontitudinal and transverse direction respectively. The main difficulty in Raman cooling such a neutral atom in our shallow dipole trap is the relatively low trap frequencies.

Preliminary Raman Cooling

A preliminary measurement of Raman cooling was done on the atom. The setup to generate the beams to drive the Raman transitions is shown in figure 32. The maximum optical power available in the each beam is $\simeq 5\,\mathrm{mW}$.

The two Raman beams are sent to the atom in the orientation shown in figure 33, with the polarisation of one beam linear along the quantisation axis and the other polarisation linearly perpendicular to it. This orientation is chosen partly due to the available optical access and partly to keep the Lamb-Dicke parameter, η, small. Although the first order sideband Rabi rate, $\Omega_{\pm}$, scales with the carrier Rabi rate, Ω_0, as $\Omega_{\pm} \approx \eta\Omega_0$, and η shouldn't be made too small to ensure an efficient Raman cooling, the initial average motional number in the experiment is large and that may complicate Raman cooling[1]. The Lamb-Dicke parameter is given by

$$\eta = kz_0, \tag{113}$$

1 The average motional number, $\langle n \rangle$, for an atom with a thermal energy with a Doppler temperature ($146\,\mu\mathrm{K}$) in the radial direction is, $\simeq 40$, if the energy is equipartioned equally among the axes. Even if the initial temperature is 5 times smaller, $\langle n \rangle$ will still be on the order of 10.

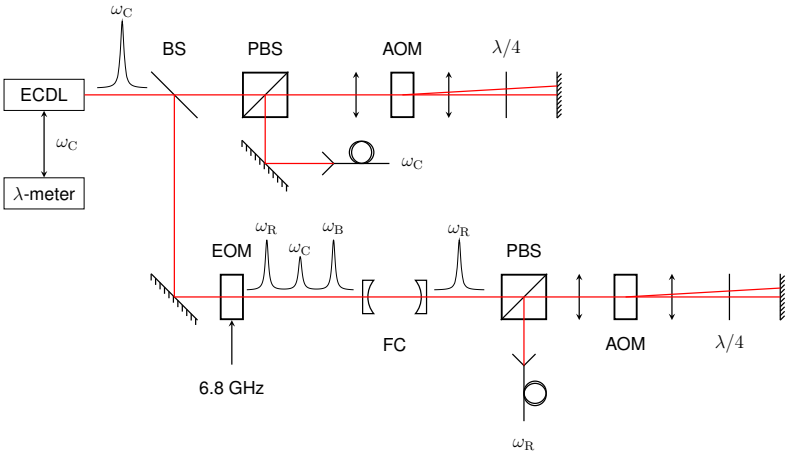

Figure 32: Setup of the laser system used to generate the Raman beams for the Raman sideband cooling measurement.. A laser beam is locked to the wavemeter such that its frequency is $\approx 15\,\mathrm{GHz}$ red detuned from the D2 transition. The beams are split into two, with one of them forming one of the pair of Raman beams and the one of them sent through an EOM, modulated at 6.8 GHz. The generated red sideband which is phase-coherent with the carrier and will form the other Raman beam, is filtered out from the carrier and other sidebands through a filter cavity. Both Raman beams are sent to AOMs which are used to tune the frequencies and also used to switch off the beams.

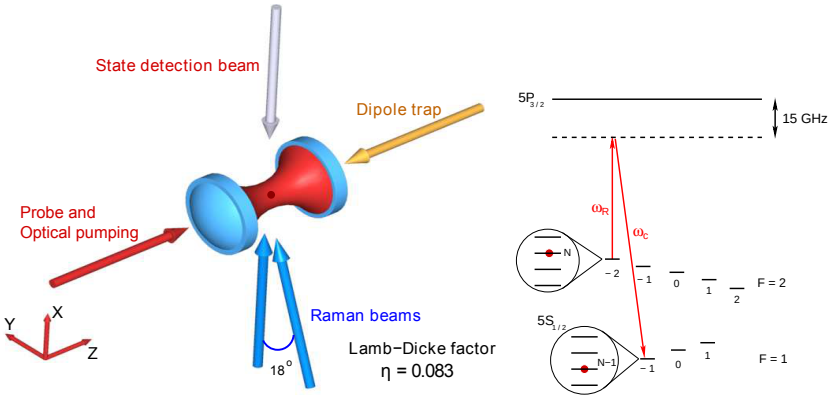

Figure 33: (Left) The orientation of the Raman beams sent to the atom. The orientation and polarisations are chosen such that the allowed Raman transition is $5S_{1/2}|F=2, m_F=-2\rangle \leftrightarrow 5S_{1/2}|F=1, m_F=-1\rangle$ as shown on the right diagram.

where k is the resultant wavevector amplitude of the two-photon Raman beam or the wavevector of repumping beam and $z_0 \equiv \sqrt{\left(\hbar/2m\omega_\rho\right)}$ is the ground state spread of the atom in the radial direction of the trap. Since the longitudinal trap frequency is very small, we shall consider only the radial direction first. They are

$$\eta_\rho^{sr} = |\Delta\mathbf{k}| z_0 = 0.083, \tag{114}$$

for the stimulated Raman transition projected along the radial direction and

$$\eta_\rho^{rp} = 0.26 \tag{115}$$

for the repumping transition from a circularly polarised beam along the quantisation axis as seen in figure 33. If anharmonicity is present in the trap and if the repumping transistion rethermalises the atom, the cooling of the other degrees of freedom can also be accomplished.. If they do not couple, additional beams need to be introduced, or the Raman beams realigned such that the cooling direction overlaps with the principal axes of the trap,to address those other degrees of freedom.

Raman sideband cooling works by first driving a two-photon Raman transition that takes away one quanta of motional energy. The Rabi rate and detuning of the Raman beams are such that the transition linewidth is smaller than the trap frequency and the sidebands can be resolved. The detuning is also made large enough such that the spontaneous Raman scattering rate is low. The atom is then recycled by optically pumping it back to the initial state. For cooling to be successful, this recycling process should not increase the average motional state of the atom. This is done by having η_ρ^{rp} small and thus the atom is cooled at the end of the process. However, for an atom in a mixed thermal distribution of motional state with average quantum number $\bar{n}$, the Rabi rate of the Raman transitions has an dependence meaning that different levels will see a different Rabi rate which will cause a decoherence in the Rabi flopping curve.

A destructive hyperfine state sensitive detection scheme which drives out the atom out of the trap if it is in the $F = 2$ ground state is employed [85]. Using this state detection beam and the Raman beams, we performed a coherent transfer of population on the carrier transition of $5S_{1/2}|F = 2, m_F = -2, n = N\rangle \leftrightarrow 5S_{1/2}|F = 1, m_F = -1, n = N\rangle$ as shown in figure 34. A two-photon Rabi oscillation of $2\pi \cdot 220\,\mathrm{kHz}$ with a decoherence time of about $40\,\mu\mathrm{s}$ was measured. If the decoherence was assumed to be entirely due to the different Rabi rates of differ-

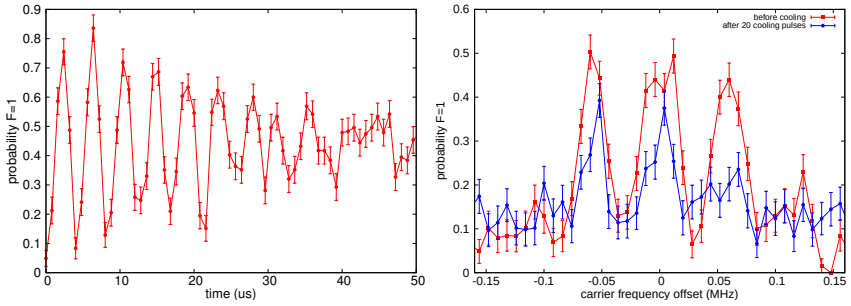

Figure 34: (Left) Rabi oscillation of the atomic population from the two hyperfine ground states when doing Raman transfer with strong Raman beams. A two-photon Rabi oscillation frequency of $(2\pi) \cdot 220\,\mathrm{kHz}$ and a damping time of about 40 µs were measured. (Right) The two-photon Rabi frequency of the beams is then reduced, and its probing time fixed at 1.5 ms, and the frequency of ω_c is scanned. Resolved motional sidebands of the atom in the trap can be seen as ω_c is scanned across resonance. After 20 cooling pulses are applied to the atom, is can be seen that the population in the blue sideband is decreased, implying that the atom is closer to the motional ground state.

ent motional states[2] n, then this corresponds to an average motional state of ≈ 6 in the radial direction. Since the decoherence time is too small, Rabi oscillations on the motional sideband transition (18 kHz) cannot be readily observed.

Next, we perform a sideband scan of the atom. The optical power of the beams were reduced and the length of the pulse kept constant at 1.5 ms such that the linewidth of the two-photon transition is about 7 kHz. The detuning between the two Raman beams, is then scanned across the two-photon resonance by varying the Raman beam frequency, ω_c (see figure 33). Figure 34 shows the red, carrier and blue sidebands of the atom in the trap. The separation of $\approx 60\,\mathrm{kHz}$ is given by the radial trap frequency. All the sidebands have a population of 0.5, due to the short decoherence time. A first attempt at cooling is done by sending 20 pulses of 100 µs each at the blue sideband frequency, with respect to ω_c, to the atom. The intensity of the Raman beams was chosen such that the carrier Rabi rate ($\Delta n = 0$) is about 50 kHz. A decrease in the amplitude of the sideband can be seen in figure 34. However, since the decoherence time is still too small, and the sideband frequency not stable, cooling is still not reliable as the sideband frequency drifts slowly. The state detection currently used is also lossy and limits the duration of the experiment. A lossless detection scheme is currently being implemented [86, 87]. Upon comple-

2 This is obviously untrue since the carrier Rabi oscillation frequency is $2\pi \cdot 220\,\mathrm{kHz}$, which is much larger than the trap frequency. Nonetheless, this gives a good estimate.

tion of the thesis, two new preprints of two new experiment of Raman sideband cooling of single neutral atoms trapped in optical tweezers were published [88, 89]. They had slightly larger trap frequencies (~ 3 times larger) and were able to reach close to the ground state energies of their trap.

Only when it is possible to cool the atom enough such that it is at the ground state of the trap and always in the region of maximal electric field strength, which is on the scale of a diffraction limited spot size, does it make sense to come in with a tighter focus of the probe. It should also be noted that the maximal interaction of the probe with the single atom will ultimately be limited by the lens used to transform the Gaussian beam into a dipolar wave. In order to break this limit, either a suitable optical element that does the ideal transformation needs to be designed or a non-Gaussian beam mode can be used in order to get that perfect spatial overlap of the probe with the single atom which will give an $R_{\mathrm{sc}} = 2$ or a $\Lambda = 8\pi/3$ [39, 47].

APPENDIX

A

RUBIDIUM TRANSITION LINES

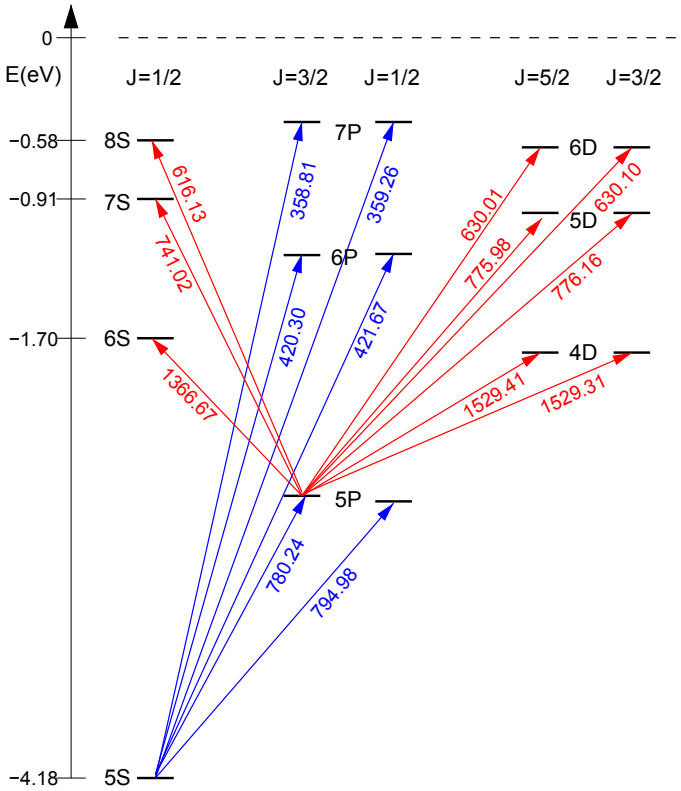

Figure 35: A Grotrian diagram of dipole allowed transitions from the $5S_{1/2}$ and $5P_{3/2}$ levels of Rubidium 87. The numbers quoted are the wavelength of the transitions in vacuum in units of nanometersKurucz and Bell [90].

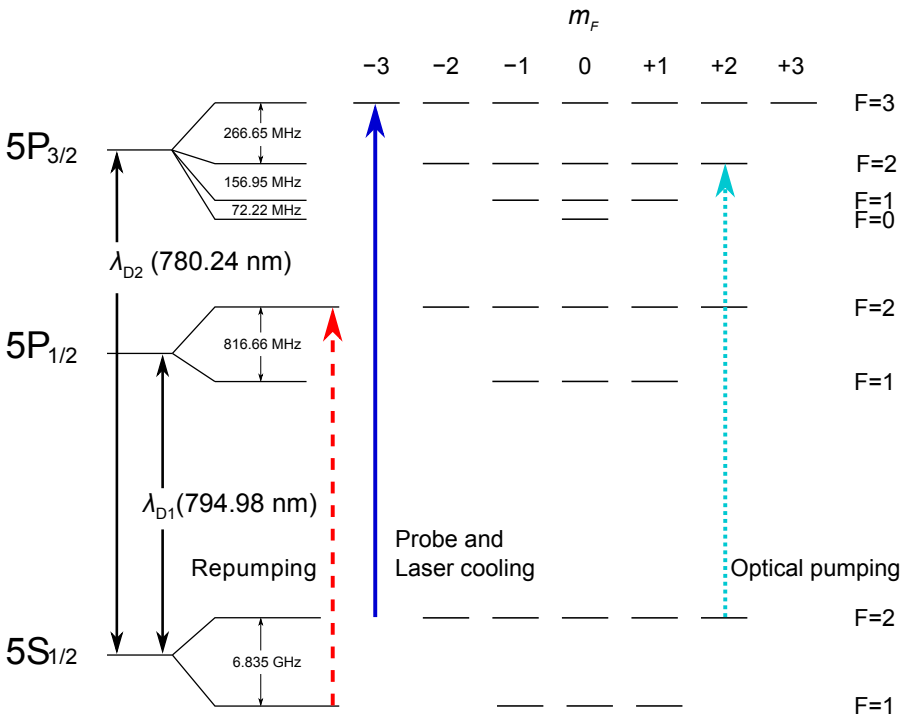

Figure 36: Hyperfine structure of the D1 and D2 transition in ^{87}Rb atom [48]. The transitions used in the experiments are shown. The frequency used for laser cooling in the MOT is slightly (24MHz) red-detuned from the resonant transition while the frequencies of the probe and optical pumping are further compensated for AC Stark and other levels shift not shown here in the figure.

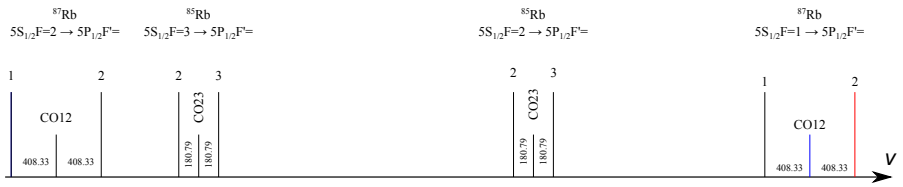

Figure 37: Spectroscopic lines of the D1 transition (795nm) where the repumper beam is locked to. The repumper is locked to the crossover transition $5S_{1/2}F = 1 \rightarrow 5P_{1/2}F' = \mathrm{CO}12$ of ^{87}Rb (blue) and shifted to the transition $5S_{1/2}F = 1 \rightarrow 5P_{1/2}F' = 2$ of ^{87}Rb (red).

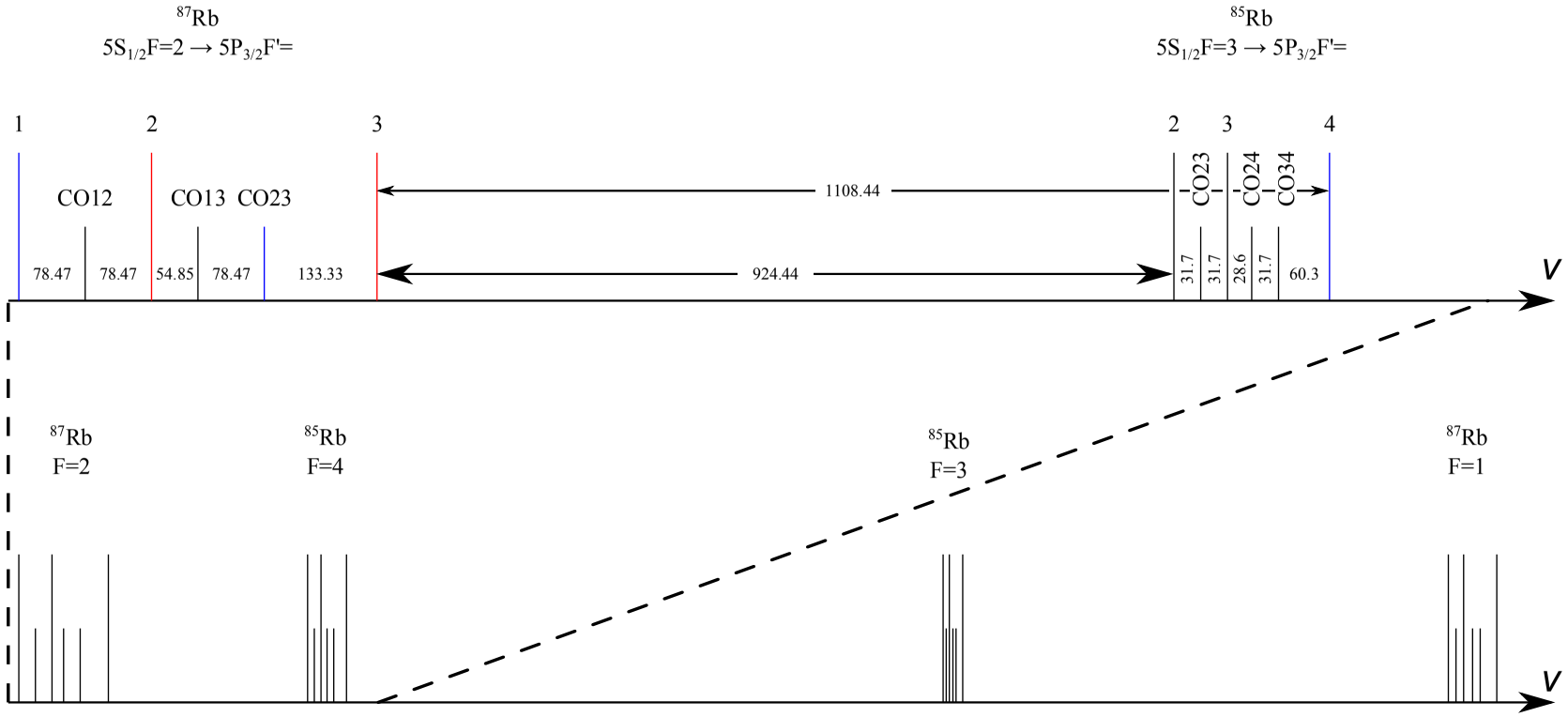

Figure 38: Spectroscopic lines of the D2 transition (780 nm) of ^{85}Rb and ^{87}Rb drawn to scale [91, 48]. Transitions marked in blue are the lock point of the lasers used while those in red are the final transition addressed by the laser after modulation via AOM and/or EOM. Further level shifts due to the dipole trap and the bias magnetic field are not shown here. (Bottom) 7 GHz scan across the D2 transition lines (780 nm). (Top) Zoom in of the lower energy transitions of the D2 line. The probe laser used in the pulsed experiment of section 3.4, is locked to the $5S_{1/2}F = 3 \rightarrow 5P_{3/2}F' = 4$ of ^{85}Rb. The frequency is then shifted upwards by ≈ 400 MHz using an AOM. The pulse is generated from the -1 order side band of an EOM which is modulated by a 1.5 GHz carrier frequency.

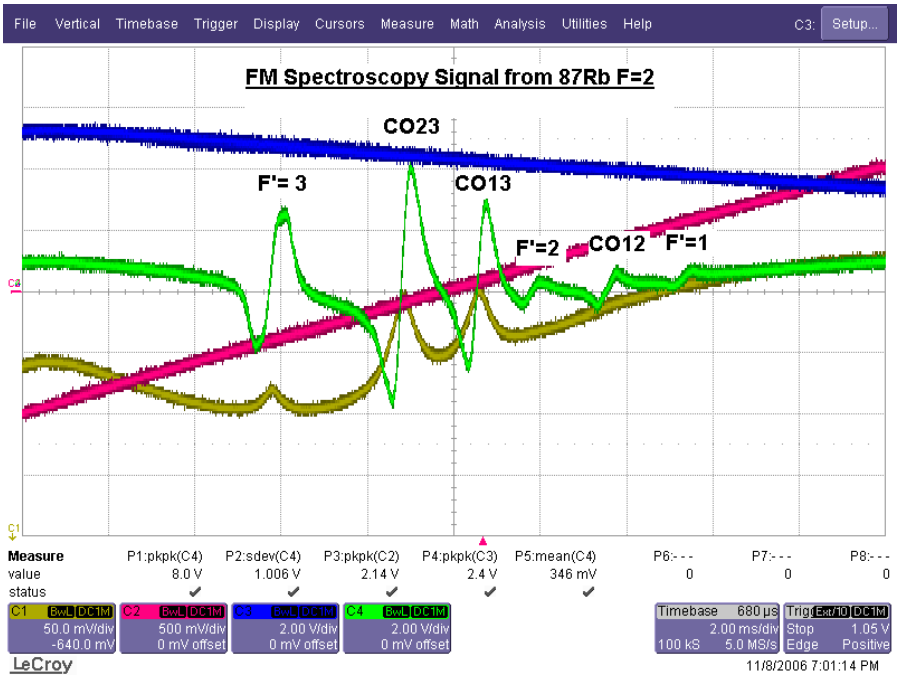

Figure 39: A typical trace of the spectrum on as seen on the oscilloscope. The yellow trace is the Doppler-free signal directly from the photodiode. The blue trace is the output voltage of the piezo. The green trace is the FM spectroscopy error signal from the $5S_{1/2}F = 2 \rightarrow 5P_{3/2}$ transitions. The red trace is the sawtooth used to ramp the voltage to the piezo.

B

METHODS

In this appendix, we describe in detail how we record the data for the weak coherent continuous wave probing experiments of section 3.3 was recorded and processed. However, the procedure for data acquisition is complicated by the lack of synchronisation of the data acquisition device and the sequencer that controls the experiment. A DT340 PCI card from Data Translation® was used as a counter to record counts from the detector and a 2 MHz square wave from a function generator, used as a timer. The *pattern generator*, which generates the sequence for the experiment, is a home made board which consist of 8 fast 512 kibibytes SRAM chips that holds a look-up table for controlling the experiment by switching on and off the AOMs, coil currents, etc. It has 4 external input lines which allows up to 16 different look-up tables and 48 digital output lines.

B.1 DATA ACQUISITION SETUP FOR CW EXPERIMENTS

Figure 40 shows the schematic of the data acquisition setup for the cw experiments. The pattern generator holds the look-up tables that controls data taking for experiment. The digital outputs are connected to AOMs that switches the beams on and off, the current controller of the quadrupole and compensation coils. It also controls the on/off state of the AND gates and other secondary triggers including ones that loop back to the pattern generator itself to go between different look-up tables. The external digital input comes from a counter that gives the count rate of detector D_f when the presence of the atom needs to be determined. There are 4 main look-up tables, which are the initial trigger for starting the sequence, measurement with the atom in the trap, checking whether the atom is still present in the trap and finally the background measurement.

The experiment begins by uploading the appropriate look-up tables into the pattern generator. Next the detuning and power for the probe beam is set, such that the scattering rate is approximately $2500\,s^{-1}$ at that particular detuning. Finally the computer begins recording counts from counter 2 every 100 ms (see fig. 40). Counter 2 has a dead time of about 10 ms which is the time for the data is written to the computer hard disk and the counter reset. By default, all the outputs of the pattern generator are switched off throughout all look-up

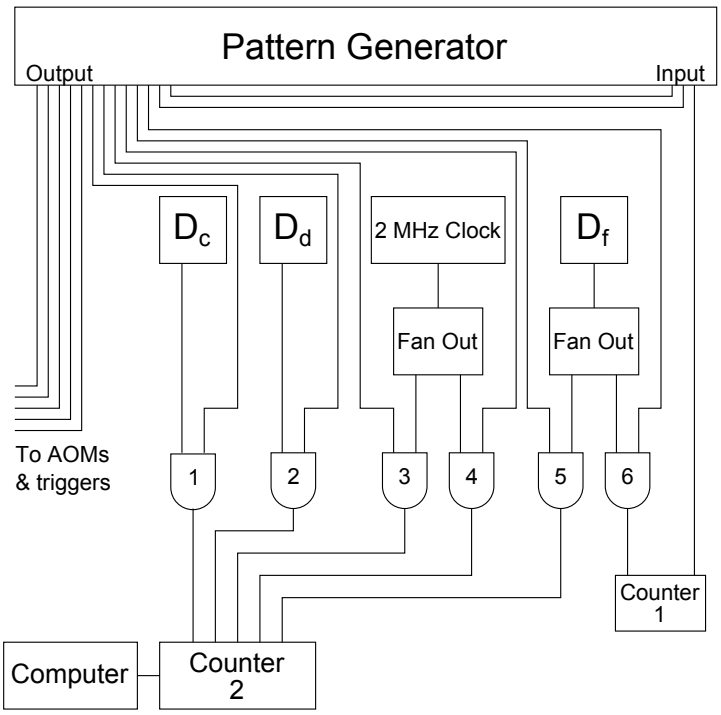

Figure 40: Schematic of the measurement setup for the cw experiments.

tables except for ones controlling the dipole trap, probe, repump in the probe beams which are always switched on, and the outputs that loop back into itself to control the look-up table used. This is to simplify the population of the look-up table such that only the required output channels needs to be switched on.

The 4 look-up tables are:

1. For the initial trigger, the MOT beams, the quadrupole coils and AND gate 6 are switched on. AND gate 6 controls the measured fluorescence from the atom from detector D_f at counter 1. Once the count rate exceeds the set threshold, counter 1 sets the input to the pattern generator high and holds it high until it is resetby an external trigger, also from the pattern generator[1].

2. The atom is optically pumped and probed in this look-up table. The bias magnetic field, used to define the quantisation axis of the atom, is switched on and atom is optically pumped into the desired 2-level system via the probe and repump in the probe beam for 20 ms. Up to this point, counter 2 has not recorded any

1 The function of counter 1 can be done via software in the look-up table as well. In this case, the output of AND gate 6 goes directly to a second input of the pattern generator, while the output of counter 1 going to the pattern generator now comes from another output of the pattern generator itself.

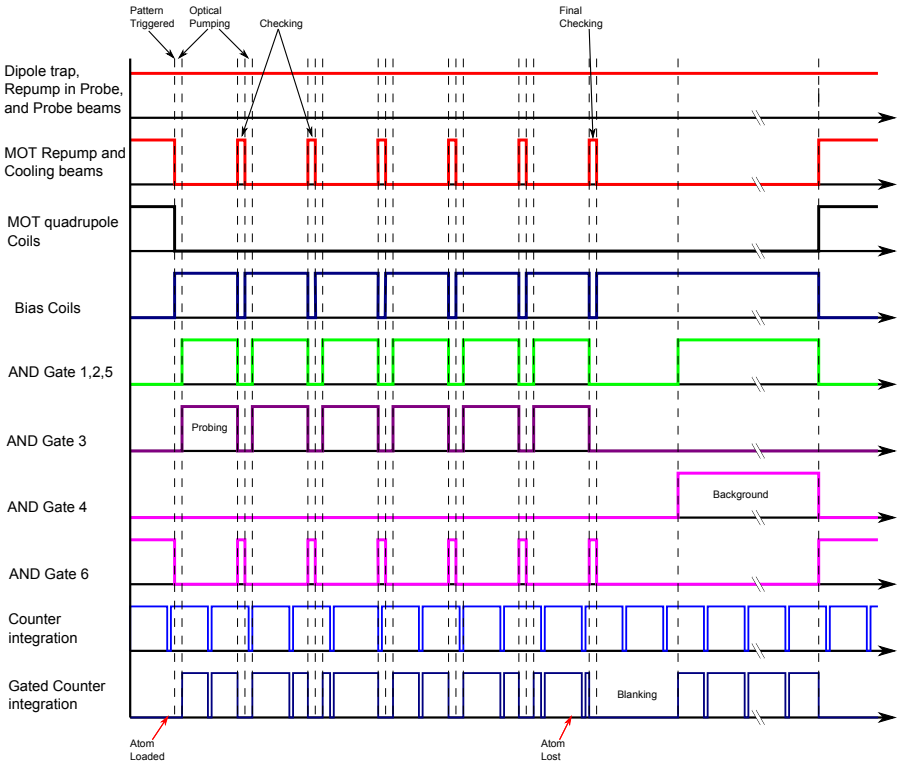

Figure 41: Timing diagram of the experimental sequence for the cw experiments. In this example, the atom is probe for 6 cycles before it is lost from the trap. Only data from 5 cycles are used since the atom leaves the trap before the end of the last cycle.

data yet. The pattern generator then keeps the second inputs to AND gates 1, 2, 3 and 5 high for 150 ms. Channels 1, 2 and 5 of counter 2 records the clicks from the detectors while channel 3 records the number of cycles of the 2 MHz clock within the 100 ms integration time. The number of cycles, divided by the 2 MHz clock then gives the time during which the detector clicks were measured.

3. Checking for the presence of the atom in the trap is done via this look-up table. The pattern generator sends a reset trigger to counter 1. The MOT beams are switched on again for about 20 ms to detect the fluorescence from the atom at detector D_f by switching on AND gate 6. If the count rate exceeds the set threshold after the detection time, the input to the pattern generator is then set high again by counter 1 and step 2 repeated. If the count rate does not reach the set threshold, the input to the pattern generator is kept low and the look-up table goes to step 4.

4. If the atom is no longer in the trap at the end of step 3, a background measurement will be performed. The bias magnetic field is switched on here as well. Nothing is done for 200 ms such that counter 2 records an empty line of zero counts in all channels. This is done to have a clear separation of data with the atom in the trap and the data due to background measurement After that, the pattern generator keeps the second inputs to AND gates 1, 2, 4 and 5 high for 2 s while counter 2 records the data used for background reference. The magnetic field bias is then switched off and step 1 repeated.

Steps 2–4 will give the detector counts and integration time of measurement both with and without atom in the trap. The normalised count rate for when the atom is in the trap, t_A and r_A (see subsection 3.3.1) can then be calculated by dividing the total detector counts by the integration time. The data from the final measurement of step 2, —just before the final check for the atom and background measurement (steps 3 and 4 consecutively)— is discarded since it is not certain if the atom had remained trapped during the measurement. The normalised background count rate without the atom can be measured in a similar way. Once enough data has been acquired, the computer stops recording data from counter 2 and the next detuning and power levels are set.

B.2 MAGNETIC COILS SWITCHING

Figure 42: Oscilloscope trace of magnetic field in the x-direction when switching off the quadrupole field. The cyan trace (C_3) is the trigger for the switch while the yellow trace (C_1) is the field probed with a fluxgate magnetometer (Stefan Mayer FLC 100). The red trace is unused. A full switch-on time of $\sim 2\,\mathrm{ms}$ and a switch-off time of $\sim 4\,\mathrm{ms}$ were measured. The magnetometer, which has a maximal bandwith of $1\,\mathrm{kHz}$ and range of ± 1 Gauss, is placed along the quadrupole x-axis and at a distance away such that it does not reach saturation. During switching of the magnetic field coils, about ~ 10–$20\,\mathrm{ms}$ is given to allow the magnetic fields in the coils to stabilise.

C

EXPONENTIAL PULSE CIRCUIT

Here we describe the details of the home-built circuit for the exponential pulse which is publised in [92]. As mentioned in section 3.4.1, the rising exponential signal is generated by exploiting the base voltage and collector current relationship of a bipolar junction transistor. Figure 43 shows the electrical circuit that implements this idea, together with other component that enable a fast switch-off of the pulse. The time constant τ_R for the exponential rise was designed to be tunable about 27 ns[1] to match the decay time of the optical transition on a D2 line in Rubidium.

A linearly rising V_{BE} is provided by charging the capacitor C1 with a constant current I_R. Transistor T1 then performs the transformation of the linear slope into an exponentially rising current I_C through equation 105. For the nominal $\tau_R = 27\,\mathrm{ns}$, a slope $\partial V_{BE}/\partial t \approx 10^6\,\mathrm{V/s}$ is necessary. Choosing $\mathrm{C1} = 3.9\,\mathrm{nF}$, this slope can be accomplished with a reasonable charging current of $I_R = 3.9\,\mathrm{mA}$.

The charging current I_R is provided by the current source combination T7 and R11, which generates a current defined by an analog input voltage V_{in}, and allows for a variation of τ_R by a factor of about 5 in both directions for exploring different interaction regimes of the optical pulse with the atom. The exponential time constant of the output pulse is then given by

$$\tau_R = \mathrm{R11}\,\mathrm{C1}\frac{V_T}{V_{\mathrm{in}} - 0.7}, \tag{116}$$

where V_T is the thermal voltage and 0.7 V refers to the base emitter forward voltage. The desired pulse does not only has to have an exponential rise, but also a steep cutoff at a given time, and the whole shape of the pulse needs to be defined with respect to some external timing reference. For this purpose, a digital signal following a standard suitable to interact with the control equipment was used.

This timing signal starts the charging of capacitor C1 when active ($V_P = -1\,\mathrm{V}$), and also routes the output current I_C via T2 into the load impedance. When it is switched to the passive state ($V_P \approx 0\,\mathrm{V}$), the output current I_C is diverted through T3 away from the output,

1 Since this electrical pulse generated will be used to envelope the electric field modulation that is sent to the EOM, the optical pulse generated, under weak linear modulation, will have a time constant that is half of that of the electrical pulse because of the square dependence of the optical intensity to the electric field.

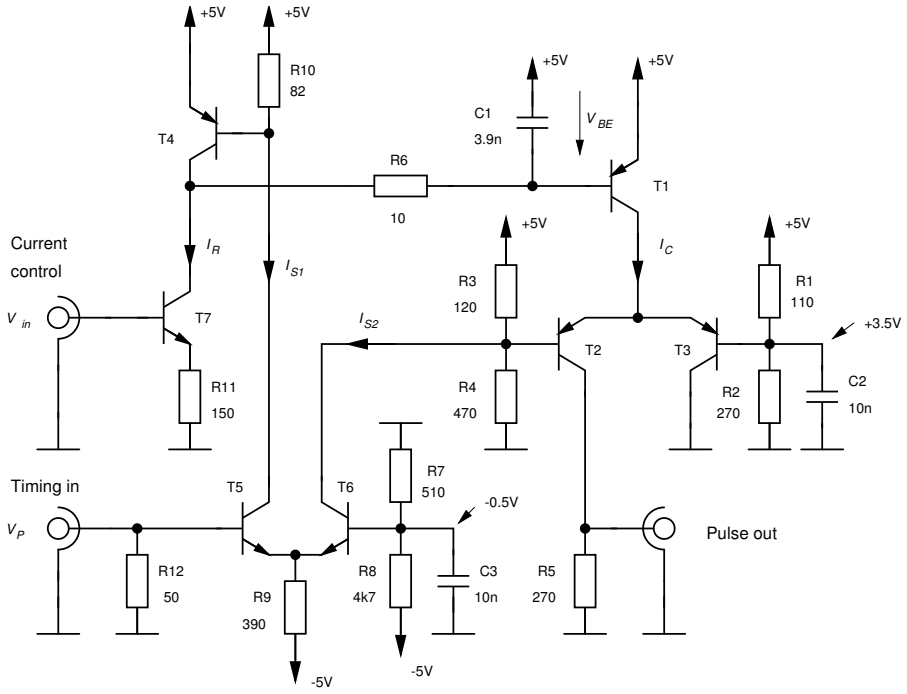

Figure 43: Electrical circuit for exponential pulse generation with risetime compatible with the atomic lifetime of the Rubidium D2 transition. T1–T4 are wide bandwidth PNP transistors (BFT93), T5–T7 wideband NPN transistors (BFR93). See text for details of operation.

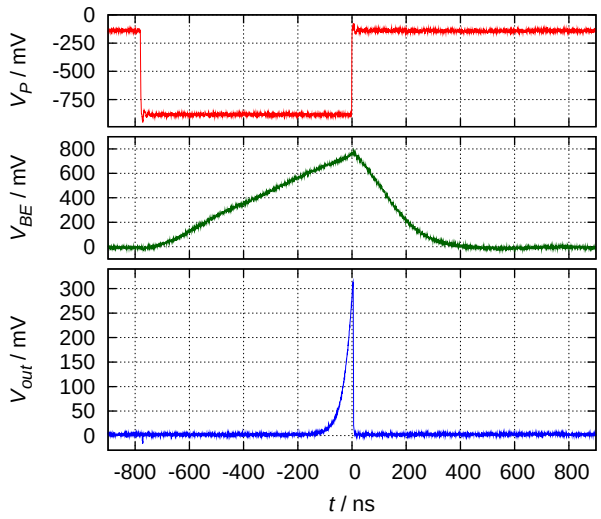

Figure 44: Operation of the exponential circuit. Triggered by V_P (top trace), the base-emitter voltage of transistor T1 rises linearly (middle trace), leading to an exponential rising voltage V_{out} (bottom trace). When the trigger signal returns to the passive state, the current is diverted away from the output, leading to a sudden drop of the envelope in V_{out}, while capacitor C1 is slowly discharged.

and C1 is discharged via T4. The basis voltage levels of T2 and T3 are chosen such that the main transistor T1 has a collector potential of 3.7 … 4.2 V to keep them unsaturated. T2 and T3 themselves stay out of saturation for an output voltage up to 2 V corresponding to an $I_C \approx 40\,\text{mA}$.

The timing of the pulse in now critically determined by the length of the control pulse sent to V_{in}, and also critically dependent on the thermal voltage, V_T. A timing diagram of the relevant voltages for a typical time constant of 30.5 ns is shown in figure 44.

D

SETUP PHOTOGRAPHS

Figure 45: Photos of the experimental setup.

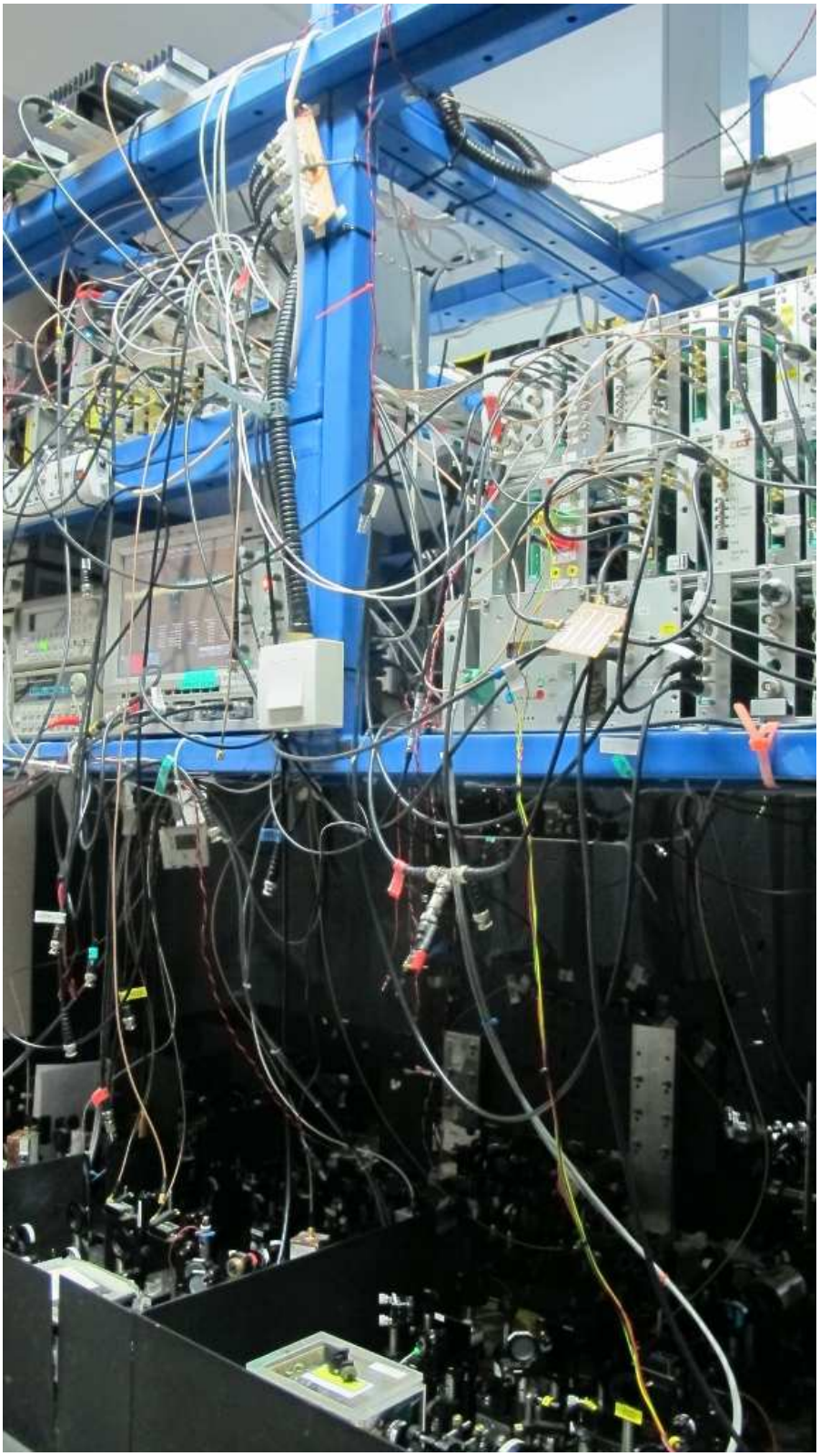

Figure 46: Laser system together with part of the data acquisition electronics.

BIBLIOGRAPHY

[1] Syed Abdullah Aljunid, Brenda Chng, Jianwei Lee, Martin Paesold, Gleb Maslennikov, and Christian Kurtsiefer. Interaction of light with a single atom in the strong focusing regime. *Journal of Modern Optics*, pages 299–305, 2010. doi: 10.1080/09500340.2010.522780.

[2] Syed Abdullah Aljunid, Meng Khoon Tey, Brenda Chng, Timothy Liew, Gleb Maslennikov, Valerio Scarani, and Christian Kurtsiefer. Phase shift of a weak coherent beam induced by a single atom. *Phys. Rev. Lett.*, 103(15):153601, Oct 2009. doi: 10.1103/PhysRevLett.103.153601.

[3] Yimin Wang, JiříMinář, Lana Sheridan, and Valerio Scarani. Efficient excitation of a two-level atom by a single photon in a propagating mode. *Phys. Rev. A*, 83:063842, Jun 2011. doi: 10.1103/PhysRevA.83.063842.

[4] Charles H. Bennett. The thermodynamics of computation—a review. *International Journal of Theoretical Physics*, 21:905–940, 1982.

[5] Richard P. Feynman. Quantum mechanical computers. *Optics News*, 11(2):11–20, Feb 1985. doi: 10.1364/ON.11.2.000011.

[6] Charles H Bennett and Gilles Brassard. *Quantum cryptography: Public key distribution and coin tossing*, volume 175, pages 175–179. Bangalore, India, 1984.

[7] Artur K. Ekert. Quantum cryptography based on bell's theorem. *Phys. Rev. Lett.*, 67:661–663, Aug 1991. doi: 10.1103/PhysRevLett.67.661.

[8] P.W. Shor. Algorithms for quantum computation: discrete logarithms and factoring. In *Foundations of Computer Science, 1994 Proceedings., 35th Annual Symposium on*, pages 124 –134, nov 1994. doi: 10.1109/SFCS.1994.365700.

[9] Lov K. Grover. A fast quantum mechanical algorithm for database search. In *Proceedings of the twenty-eighth annual ACM symposium on Theory of computing*, STOC '96, pages 212–219, New York, NY, USA, 1996. ACM. ISBN 0-89791-785-5. doi: 10.1145/237814.237866.

[10] Andrew Steane. Quantum computing. *Reports on Progress in Physics*, 61(2):117, 1998.

[11] J. I. Cirac and P. Zoller. Quantum computations with cold trapped ions. *Phys. Rev. Lett.*, 74(20):4091–4094, May 1995. doi: 10.1103/PhysRevLett.74.4091.

[12] Gavin K. Brennen, Carlton M. Caves, Poul S. Jessen, and Ivan H. Deutsch. Quantum logic gates in optical lattices. *Phys. Rev. Lett.*, 82(5):1060–1063, Feb 1999. doi: 10.1103/PhysRevLett.82.1060.

[13] J.A. Jones. Nmr quantum computation. *Progress in Nuclear Magnetic Resonance Spectroscopy*, 38(4):325–360, 2001.

[14] Q. A. Turchette, C. J. Hood, W. Lange, H. Mabuchi, and H. J. Kimble. Measurement of conditional phase shifts for quantum logic. *Phys. Rev. Lett.*, 75:4710–4713, Dec 1995. doi: 10.1103/PhysRevLett.75.4710.

[15] John Clarke and Frank K. Wilhelm. Superconducting quantum bits. *Nature*, 453(7198):1031–1042, Jun 2008. doi: 10.1038/nature07128.

[16] Daniel Loss and David P. DiVincenzo. Quantum computation with quantum dots. *Phys. Rev. A*, 57(1):120–126, Jan 1998. doi: 10.1103/PhysRevA.57.120.

[17] E. Knill, R. Laflamme, and G. J. Milburn. A scheme for efficient quantum computation with linear optics. *Nature*, 409(6816):46–52, Jan 2001. doi: 10.1038/35051009.

[18] P. Neumann, N. Mizuochi, F. Rempp, P. Hemmer, H. Watanabe, S. Yamasaki, V. Jacques, T. Gaebel, F. Jelezko, and J. Wrachtrup. Multipartite entanglement among single spins in diamond. *Science*, 320(5881):1326–1329, 2008. doi: 10.1126/science.1157233.

[19] David P. DiVincenzo. *The Physical Implementation of Quantum Computation*, pages 1–13. Wiley-VCH Verlag GmbH & Co. KGaA, 2005. ISBN 9783527603183. doi: 10.1002/3527603182.ch1.

[20] J. I. Cirac, P. Zoller, H. J. Kimble, and H. Mabuchi. Quantum state transfer and entanglement distribution among distant nodes in a quantum network. *Phys. Rev. Lett.*, 78:3221–3224, Apr 1997. doi: 10.1103/PhysRevLett.78.3221.

[21] L. M. Duan, M. D. Lukin, J. I. Cirac, and P. Zoller. Long-distance quantum communication with atomic ensembles and linear optics. *Nature*, 414(6862):413–418, Nov 2001. doi: 10.1038/35106500.

[22] P. Zoller, Th. Beth, D. Binosi, R. Blatt, H. Briegel, D. Bruss, T. Calarco, J. I. Cirac, D. Deutsch, J. Eisert, A. Ekert, C. Fabre, N. Gisin, P. Grangiere, M. Grassl, S. Haroche, A. Imamoglu, A. Karlson, J. Kempe, L. Kouwenhoven, S. Kröll, G. Leuchs, M. Lewenstein, D. Loss, N. Lütkenhaus, S. Massar, J. E. Mooij, M. B. Plenio, E. Polzik, S. Popescu, G. Rempe, A. Sergienko, D. Suter, J. Twamley, G. Wendin, R. Werner, A. Winter, J. Wrachtrup, and A. Zeilinger. Quantum information processing and communication. *The European Physical Journal D - Atomic, Molecular, Optical and Plasma Physics*, 36:203–228, 2005.

[23] H. J. Kimble. The quantum internet. *Nature*, 453(7198):1023–1030, June 2008. doi: 10.1038/nature07127.

[24] J. McKeever, A. Boca, A. D. Boozer, J. R. Buck, and H. J. Kimble. Experimental realization of a one-atom laser in the regime of strong coupling. *Nature*, 425(6955):268–271, 2003. doi: 10.1038/nature01974.

[25] A. D. Boozer, A. Boca, R. Miller, T. E. Northup, and H. J. Kimble. Reversible state transfer between light and a single trapped atom. *Phys. Rev. Lett.*, 98:193601, May 2007. doi: 10.1103/PhysRevLett.98.193601.

[26] Stefan Kuhr, Wolfgang Alt, Dominik Schrader, Martin Müller, Victor Gomer, and Dieter Meschede. Deterministic delivery of a single atom. *Science*, 293(5528):278–280, 2001. doi: 10.1126/science.1062725.

[27] P. Michler, A. Imamoglu, M. D. Mason, P. J. Carson, G. F. Strouse, and S. K. Buratto. Quantum correlation among photons from a single quantum dot at room temperature. *Nature*, 406(6799):968–970, Aug 2000. doi: 10.1038/35023100.

[28] G. Wrigge, I. Gerhardt, J. Hwang, G. Zumofen, and V. Sandoghdar. Efficient coupling of photons to a single molecule and the observation of its resonance fluorescence. *Nature Physics*, 4(1):60–66, JAN 2008. doi: 10.1038/nphys812.

[29] Ilya Fushman, Dirk Englund, Andrei Faraon, Nick Stoltz, Pierre Petroff, and Jelena Vučković. Controlled phase shifts with a

single quantum dot. *Science*, 320(5877):769–772, 2008. doi: 10.1126/science.1154643.

[30] B. Darquié, M. P. A. Jones, J. Dingjan, J. Beugnon, S. Bergamini, Y. Sortais, G. Messin, A. Browaeys, and P. Grangier. Controlled single-photon emission from a single trapped two-level atom. *Science*, 309(5733):454–456, 2005. doi: 10.1126/science.1113394.

[31] Chen X.W. Eghlidi H. Kukura P. Lettow R. Renn A. Sandoghdar V. Götzinger S. Lee, K.G. A planar dielectric antenna for directional single-photon emission and near-unity collection efficiency. *Nature Photonics*, 5(3):166–169, 2011.

[32] M. K. Tey, Z. Chen, S. A. Aljunid, B. Chng, F. Huber, G. Maslennikov, and C. Kurtsiefer. Strong interaction between light and a single trapped atom without the need for a cavity. *Nat Phys*, 4 (12):924–927, 2008. doi: 10.1038/nphys1096.

[33] Meng Khoon Tey, Gleb Maslennikov, Timothy C H Liew, Syed Abdullah Aljunid, Florian Huber, Brenda Chng, Zilong Chen, Valerio Scarani, and Christian Kurtsiefer. Interfacing light and single atoms with a lens. *New Journal of Physics*, 11(4):043011, 2009. doi: 10.1088/1367-2630/11/4/043011.

[34] Colin Teo and Valerio Scarani. Lenses as an atom-photon interface: A semiclassical model. *Optics Communications*, 284(19): 4485 – 4490, 2011. doi: 10.1016/j.optcom.2011.05.065.

[35] C. Cohen-Tannoudji, J. Dupont-Roc, and G. Grynberg. *Atom-photon interactions: basic processes and application*. Wiley, New York, 1992.

[36] R. Loudon. *The quantum theory of light*. Oxford science publications. Oxford University Press, 2000. ISBN 9780198501770.

[37] M.O. Scully and M.S. Zubairy. *Quantum optics*. Cambridge University Press, 1997. ISBN 9780521435956.

[38] Christopher J. Foot. *Atomic physics*. Oxford master series in physics. Oxford University Press, Oxford, 2005. ISBN 9780198506966.

[39] G. Zumofen, N. M. Mojarad, V. Sandoghdar, and M. Agio. Perfect reflection of light by an oscillating dipole. *Phys. Rev. Lett.*, 101: 180404, Oct 2008. doi: 10.1103/PhysRevLett.101.180404.

[40] M. Born, E. Wolf, and A.B. Bhatia. *Principles of Optics: Electromagnetic Theory of Propagation, Interference and Diffraction of Light*. Cambridge University Press, 1999. ISBN 9780521642224.

[41] S. J. van Enk and H. J. Kimble. Strongly focused light beams interacting with single atoms in free space. *Phys. Rev. A*, 63:023809, Jan 2001. doi: 10.1103/PhysRevA.63.023809.

[42] J.D. Jackson. *Classical electrodynamics*. Wiley, 1999. ISBN 9780471309321.

[43] R. C. Davis and C. C. Williams. Optical dipole model for photodetection in the near field. *J. Opt. Soc. Am. A*, 18(7):1543–1551, Jul 2001. doi: 10.1364/JOSAA.18.001543.

[44] H Paul and R Fischer. Light absorption by a dipole. *Soviet Physics Uspekhi*, 26(10):923, 1983.

[45] I. M. Bassett and R. Winston. Limits to concentration in physical optics and wave mechanics. *Optica Acta: International Journal of Optics*, 31(5):499–505, 1984. doi: 10.1080/713821548.

[46] Brian J Smith and M G Raymer. Photon wave functions, wavepacket quantization of light, and coherence theory. *New Journal of Physics*, 9(11):414, 2007.

[47] M. Stobińska, G. Alber, and G. Leuchs. Perfect excitation of a matter qubit by a single photon in free space. *EPL (Europhysics Letters)*, 86(1):14007, 2009. doi: 10.1209/0295-5075/86/14007.

[48] Daniel A. Steck. "rubidium 87 d line data", December 2010.

[49] Carl E. Wieman and Leo Hollberg. Using diode lasers for atomic physics. *Review of Scientific Instruments*, 62(1):1–20, 1991. doi: 10.1063/1.1142305.

[50] T.W. Hänsch and A.L. Schawlow. Cooling of gases by laser radiation. *Optics Communications*, 13(1):68 – 69, 1975. doi: 10.1016/0030-4018(75)90159-5.

[51] A. S. Arnold, J. S. Wilson, and M. G. Boshier. A simple extended-cavity diode laser. *Review of Scientific Instruments*, 69(3):1236–1239, 1998. doi: 10.1063/1.1148756.

[52] Karen Liu and Michael G. Littman. Novel geometry for single-mode scanning of tunable lasers. *Opt. Lett.*, 6(3):117–118, Mar 1981. doi: 10.1364/OL.6.000117.

[53] Gary C. Bjorklund. Frequency-modulation spectroscopy: a new method for measuring weak absorptions and dispersions. *Opt. Lett.*, 5(1):15–17, Jan 1980. doi: 10.1364/OL.5.000015.

[54] J. L. Hall, L. Hollberg, T. Baer, and H. G. Robinson. Optical heterodyne saturation spectroscopy. *Applied Physics Letters*, 39(9): 680–682, 1981. doi: 10.1063/1.92867.

[55] C.S. Adams and E. Riis. Laser cooling and trapping of neutral atoms. *Progress in Quantum Electronics*, 21(1):1–79, 1997. doi: 10.1016/S0079-6727(96)00006-7.

[56] H. J. Metcalf and P. van der Straten. Laser cooling and trapping of atoms. *J. Opt. Soc. Am. B*, 20(5):887–908, May 2003. doi: 10.1364/JOSAB.20.000887.

[57] L.D. Landau and E.M. Lifshitz. *Mechanics*. Course of theoretical physics. Butterworth-Heinemann, 1976. ISBN 9780750628969.

[58] Nicolas Schlosser, Georges Reymond, Igor Protsenko, and Philippe Grangier. Sub-poissonian loading of single atoms in a microscopic dipole trap. *Nature*, 411:1024–1027, Jun 2001. doi: 10.1038/35082512.

[59] N. Schlosser, G. Reymond, and P. Grangier. Collisional blockade in microscopic optical dipole traps. *Phys. Rev. Lett.*, 89(2):023005, Jun 2002. doi: 10.1103/PhysRevLett.89.023005.

[60] B Ueberholz, S Kuhr, D Frese, D Meschede, and V Gomer. Counting cold collisions. *Journal of Physics B: Atomic, Molecular and Optical Physics*, 33(4):L135, 2000.

[61] S. J. M. Kuppens, K. L. Corwin, K. W. Miller, T. E. Chupp, and C. E. Wieman. Loading an optical dipole trap. *Phys. Rev. A*, 62: 013406, Jun 2000. doi: 10.1103/PhysRevA.62.013406.

[62] V. Gomer, B. Ueberholz, S. Knappe, F. Strauch, D. Frese, and D. Meschede. Decoding the dynamics of aÂ single trapped atom from photon correlations. *Applied Physics B: Lasers and Optics*, 67: 689–697, 1998.

[63] D. Frese, B. Ueberholz, S. Kuhr, W. Alt, D. Schrader, V. Gomer, and D. Meschede. Single atoms in an optical dipole trap: Towards a deterministic source of cold atoms. *Phys. Rev. Lett.*, 85: 3777–3780, Oct 2000. doi: 10.1103/PhysRevLett.85.3777.

[64] Markus Weber, Jürgen Volz, Karen Saucke, Christian Kurtsiefer, and Harald Weinfurter. Analysis of a single-atom dipole trap.

Phys. Rev. A, 73:043406, Apr 2006. doi: 10.1103/PhysRevA.73.043406.

[65] U. M. Titulaer and R. J. Glauber. Correlation functions for coherent fields. *Phys. Rev.*, 140:B676–B682, Nov 1965. doi: 10.1103/PhysRev.140.B676.

[66] Roy J. Glauber. The quantum theory of optical coherence. *Phys. Rev.*, 130:2529–2539, Jun 1963. doi: 10.1103/PhysRev.130.2529.

[67] Meng Khoon Tey. *Interfacing light and a single quantum system with a lens*. PhD thesis, National University of Singapore, Singapore, 2009.

[68] Peter L. Smith, Claas Heise, Jim R. Esmond, and Robert L. Kurucz. Amp tools: Databases: Kurucz atomic line database.

[69] C. Tuchendler, A. M. Lance, A. Browaeys, Y. R. P. Sortais, and P. Grangier. Energy distribution and cooling of a single atom in an optical tweezer. *Phys. Rev. A*, 78:033425, Sep 2008. doi: 10.1103/PhysRevA.78.033425.

[70] A Fuhrmanek, A M Lance, C Tuchendler, P Grangier, Y R P Sortais, and A Browaeys. Imaging a single atom in a time-of-flight experiment. *New Journal of Physics*, 12(5):053028, 2010.

[71] C. Monroe, D. M. Meekhof, B. E. King, S. R. Jefferts, W. M. Itano, D. J. Wineland, and P. Gould. Resolved-sideband raman cooling of a bound atom to the 3d zero-point energy. *Phys. Rev. Lett.*, 75:4011–4014, Nov 1995. doi: 10.1103/PhysRevLett.75.4011.

[72] Jianwei Lee. Towards resolved-sideband raman cooling of a single 87 rubidium atom in a fort. Master's thesis, National University of Singapore, 2010.

[73] Paul Horowitz and W. Hill. *The art of electronics*. Number v. 816 in The Art of Electronics. Cambridge University Press, 1989. ISBN 9780521370950.

[74] U Volz and H Schmoranzer. Precision lifetime measurements on alkali atoms and on helium by beam-gas-laser spectroscopy. *Physica Scripta*, 1996(T65):48, 1996.

[75] M. D. Eisaman, J. Fan, A. Migdall, and S. V. Polyakov. Invited review article: Single-photon sources and detectors. *Review of Scientific Instruments*, 82(7):071101, 2011. doi: 10.1063/1.3610677.

[76] D. N. Matsukevich, T. Chanelière, S. D. Jenkins, S.-Y. Lan, T. A. B. Kennedy, and A. Kuzmich. Deterministic single photons via conditional quantum evolution. *Phys. Rev. Lett.*, 97:013601, Jul 2006. doi: 10.1103/PhysRevLett.97.013601.

[77] J. McKeever, A. Boca, A. D. Boozer, R. Miller, J. R. Buck, A. Kuzmich, and H. J. Kimble. Deterministic generation of single photons from one atom trapped in a cavity. *Science*, 303(5666): 1992–1994, 2004. doi: 10.1126/science.1095232.

[78] Markus Hijlkema, Bernhard Weber, Holger P. Specht, Simon C. Webster, and Rempe Gerhard Kuhn, Axel. A single-photon server with just one atom. *Nature Physics*, 3(4):253–255, 2007. doi: 10.1038/nphys569.

[79] Alessandro Fedrizzi, Thomas Herbst, Andreas Poppe, Thomas Jennewein, and Anton Zeilinger. A wavelength-tunable fiber-coupled source of narrowband entangled photons. *Opt. Express*, 15(23):15377–15386, Nov 2007. doi: 10.1364/OE.15.015377.

[80] N. Piro, F. Rohde, C. Schuck, M. Almendros, J. Huwer, J. Ghosh, A. Haase, M. Hennrich, and F. Dubin. Heralded single-photon absorption by a singleatom. *Nature Physics*, 7(1):17–20, 2011.

[81] Pavel Kolchin, Chinmay Belthangady, Shengwang Du, G. Y. Yin, and S. E. Harris. Electro-optic modulation of single photons. *Phys. Rev. Lett.*, 101:103601, Sep 2008. doi: 10.1103/PhysRevLett.101.103601.

[82] H.P. Specht, J. Bochmann, M. Mücke, B. Weber, E. Figueroa, D.L. Moehring, and G. Rempe. Phase shaping of single-photon wave packets. *Nature Photonics*, 3(8):469–472, 2009.

[83] Kahraman G. Köprülü, Yu-Ping Huang, Geraldo A. Barbosa, and Prem Kumar. Lossless single-photon shaping via heralding. *Opt. Lett.*, 36(9):1674–1676, May 2011. doi: 10.1364/OL.36.001674.

[84] M. Sondermann, R. Maiwald, H. Konermann, N. Lindlein, U. Peschel, and G. Leuchs. Design of a mode converter for efficient light-atom coupling in free space. *Applied Physics B: Lasers and Optics*, 89:489–492, 2007.

[85] M. P. A. Jones, J. Beugnon, A. Gaëtan, J. Zhang, G. Messin, A. Browaeys, and P. Grangier. Fast quantum state control of a single trapped neutral atom. *Phys. Rev. A*, 75:040301, Apr 2007. doi: 10.1103/PhysRevA.75.040301.

[86] Michael J. Gibbons, Christopher D. Hamley, Chung-Yu Shih, and Michael S. Chapman. Nondestructive fluorescent state detection of single neutral atom qubits. *Phys. Rev. Lett.*, 106:133002, Mar 2011. doi: 10.1103/PhysRevLett.106.133002.

[87] A. Fuhrmanek, R. Bourgain, Y. R. P. Sortais, and A. Browaeys. Free-space lossless state detection of a single trapped atom. *Phys. Rev. Lett.*, 106:133003, Mar 2011. doi: 10.1103/PhysRevLett.106.133003.

[88] A.M. Kaufman, B.J. Lester, and C.A. Regal. Laser cooling a neutral atom to the three-dimensional vibrational ground state of an optical tweezer. *arXiv preprint arXiv:1209.2087*, 2012.

[89] JD Thompson, TG Tiecke, AS Zibrov, V. Vuletić, and MD Lukin. Coherence and raman sideband cooling of a single atom in an optical tweezer. *arXiv preprint arXiv:1209.3028*, 2012.

[90] R. Kurucz and B. Bell. Atomic line data. *Atomic Line Data (RL Kurucz and B. Bell) Kurucz CD-ROM No. 23. Cambridge, Mass.: Smithsonian Astrophysical Observatory, 1995.*, 23, 1995.

[91] Daniel A. Steck. "rubidium 85 d line data", December 2010.

[92] Hoang Lan Dao, Syed Abdullah Aljunid, Gleb Maslennikov, and Christian Kurtsiefer. Preparation of an exponentially rising optical pulse for efficient excitation of single atoms in free space. *Review of Scientific Instruments*, 83(8):083104, 2012. doi: 10.1063/1.4739776.